SKI Report 97:44

Experimental Investigations on Vessel-hole Ablation During Severe Accidents

B R Sehgal
T N Dinh
J A Green
D Paladino

December 1997

SKi

STATENS KÄRNKRAFTINSPEKTION
Swedish Nuclear Power Inspectorate

29 - 10

SKI Report 97:44

Experimental Investigations on Vessel-hole Ablation During Severe Accidents

B. R. Sehgal
T. N. Dinh
J. A. Green
D. Paladino

Division of Nuclear Power Safety
Royal Institute of Technology
SE-100 44 Stockholm, Sweden

December 1997

Abstract

This report presents experimental results, and subsequent analyses, of scaled reactor pressure vessel (RPV) failure site ablation tests conducted at the Royal Institute of Technology Division of Nuclear Power Safety (RIT/NPS). The goal of the test program is to reduce the uncertainty level associated with the phase-change-ablation process, and, thus, improve the characterization of the melt discharge loading on the containment.

In a series of moderate temperature experiments, the corium melt is simulated by the binary oxide CaO-B_2O_3 or the binary eutectic and non-eutectic salts $NaNO_3$-KNO_3, while the RPV head steel is represented by a Pb, Sn or metal alloys plate. A complementary set of experiments was conducted at lower temperatures, using water as melt and salted ice as plate material. These experiments scale well to the postulated prototypical conditions.

The multidimensional code HAMISA, developed at RIT/NPS, is employed to analyze the experiments with good pre- and post-test predictions. The effects of melt viscosity and crust surface roughness, along with failure site entrance and exit frictional losses on the ablation characteristics are investigated. Theoretical concept was proposed to describe physical mechanisms which govern the vessel-hole ablation process during core melt discharge from RPV.

Experimental data obtained from hole ablation tests and separate-effect tests performed at RIT/NPS were used to validate component physical models of the HAMISA code. It is believed that the hole ablation phenomenology is quite well understood.

Detail description of experiments and experimental data, as well as results of analyses are provided in the appendixes.

This work was conducted through the support of the Swedish Nuclear Power Inspectorate (SKI), the Finnish Utilities (IVO, TVO), the U.S. Nuclear Regulatory Commission (USNRC), the Swiss Nuclear Safety Commission (HSK), and the European Commission.

CONTENTS

1 Introduction

In the highly unlikely event of a severe reactor accident in a light water reactor (LWR), a potential exists for the formation of a particulate debris bed in the hemispherical lower head volume. With insufficient cooling, this debris bed could re-melt due to fission product decay heat, and a melt pool could be formed. The size, composition and temperature of this melt pool is highly dependent upon the severe accident scenario by which it is formed. Regardless of its formation however, the melt pool can attack the lower melting point vessel steel wall, and in the absence of either internal or external cooling, a failure location can develop. Recall that an 80-20% binary mixture of UO_2-ZrO_2 (corium) exhibits liquidus and solidus temperatures of approximately 2900 and 2825K, respectively, while the vessel steel will have a melting temperature of $\approx$ 1700K. Failure sites could develop as the result of melt attack at a penetration (control rod or instrument tube) [1], [2] [3] or, possibly, from partial erosion of the steel shell due to jet impingement [4], [5], as the melt relocates from the original core region. In addition, vessel creep, due to extended times at high temperatures, could potentially develop into a breach of the lower pressure vessel steel wall [6]. It should be noted here that as soon as a creep-induced failure site appears, the melt flow through the failure site will primarily determine the rate of the increase of the vessel failure area, at that site, since the pressure loading will be relieved.

As the melt discharges through the failure site, the ablation rate of the RPV steel will depend upon many factors. One of the most important of these will be the stability and the persistence of the crust layer, which forms between flowing melt material and the ablating pressure vessel. The crust presents a resistance to heat transfer from the melt, thereby reducing the ablation rate. Crust formation depends strongly upon the initial melt superheat and the initial structure temperature. The mechanical stability of crust layers in this situation is highly uncertain, since the crust may be swept out along with the molten vessel wall material by the flow of the corium melt through the failure site.

Currently, there does not exist a substantial database of fluid and heat transfer process related to phase-change-hole-ablation dynamics. A review of related experiments can be found in the references by Pilch [7]. Many of these experiments were conducted at SNL in support of the DCH issue resolution [8], however, as shown in Fig.1 the limited hole enlargement in these experiments did not bring these data into the scale-range needed for the scenario of penetration failures in prototypical accident. The scaling methodology developed by Pilch was tested only against the thermite data obtained at SNL [7] . Past studies [8]-[10] employed the temperature difference between melt temperature and vessel melting point (Δ T = T_{melt}-$T_{mp,w}$) rather than that between the melt temperature and solidus temperature when a crust is formed (Δ T = T_{melt}-$T_{sol,m}$). That choice ensures conservatism, however, it is not clear how much conservation has been added. More recently, Chu et al. [11] employed Δ T = T_{melt}-$T_{sol,m}$ for assessments of vessel hole ablation, in the THIRMAL code.
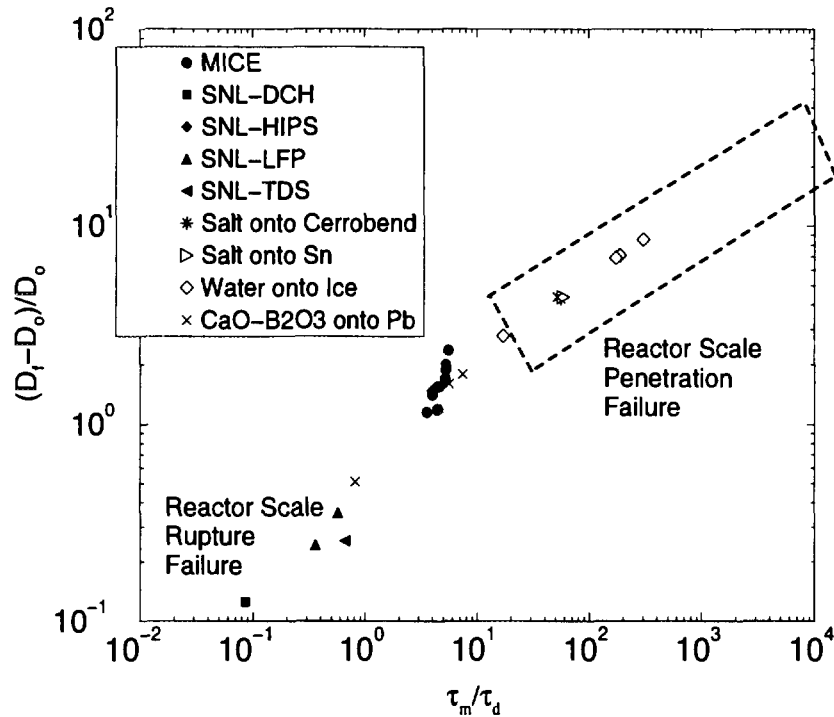
Figure 1: Hole Ablation Scaling

The experimental research program at RIT/NPS has been focused on reducing the uncertainties, associated with failure site ablation, from, both, an integral and a dynamic point of view; and to obtain data in the scale range needed for penetration failure. Employing the scaling methodology of Pilch [7], Figure 1 shows the data obtained at SNL and, the data obtained at RIT/NPS with various simulant melt and vessel wall materials. The data is plotted for Pilch's scaling parameter: ratio of hole enlargement/initial hole size on the y axis and the ratio of characteristic time for melt discharge through the original hole size/characteristic time for doubling of the hole size, due to the ablation process. Also shown by, a dotted rectangle, is the range of the x- and y-scale values needed for the reactor-scale penetration failures. It is seen that the RIT/NPS data falls in the scale range needed. As noted above, a variety of simulant materials were employed, in order to better understand the parameters of primary importance. Great care must be exercised when extrapolating the results from smaller, and thus often laminar flow, scaled experiments to the anticipated turbulent behavior for hole flow in the prototypical situation. A more detailed look at the scaling rationale and initial experiments can be found in the references of Sehgal et al. [12]-[13] as well as by Dinh et al. [14]. The earlier tests were conducted with the simulant materials PbO-B_2O_3 for melt, and Pb plates for vessel wall. Corrosion and health concerns prompted the switch to alternate melt simulants. The melt simulant CaO-B_2O_3 has been employed at both 4 and 20 liter volumes ($\approx$ 10 and 60 kg respec-

tively). Additionally, a test program, using water as melt simulant, and salted ice plates as simulant for RPV wall, was conducted to obtain data at high Reynolds numbers for the melt flow. Some limited tests using binary salt mixtures onto low- melting-point-alloys and metals were also conducted. In addition, a two-dimensional transient, mechanistic model named "Hole Ablation Modeling In Severe Accidents" (HAMISA) was developed to describe the hole ablation process and determine the rate of melt discharge from the vessel to the containment as a function of time. This report will present the results of these experiments and the comparison of the experimental observations with the predictions obtained from the HAMISA model [14].

Table 1: Thermo-Physical Properties of Simulant Materials.

Material	T_{liq} T_{sol} (K)	Δh_{fus} (kJ/kg)	k_l k_s (W/m.K)	ρ (kg/m^3)	$c_{p,l}$ $c_{p,s}$ (J/kg.K)	σ (N/m)	μ (mPa·s)
Melt							
CaO-B$_2$O$_3$	1300 1250	460	3.0 2.0	2500	2200 1530	0.15	100-300
NaNO$_3$-KNO$_3$	553 493	255	0.45 0.6	1830	1560 1340	0.11	1.5-2
Water	273 273	33.3	0.6 2.45	960-990	4180 1800	0.06	1.7-0.31
Plates							
Lead	600 600	23.3	16 32	11344	129 129	0.44	1.4
Cerrobend	343 343	39.8	18 18	9670	184 146	0.35	3.3
Steel	1793 1793	247	27 35	7700	835 750	0.3	5.4

2 Experimental Arrangement

Oxidic Melt Simulant. Since, the oxidic simulant CaO-B$_2$O$_3$ is non-magnetic, it is heated inside a steel crucible, using a 50kW/25kHz induction generator. The first set of experiments was conducted using a crucible and coil capable of 5 liter capacity, while subsequent experiments have employed a larger, 25 liter, arrangement. Oxidation at high temperatures is minimized with argon gas flow. Once the melt has been generated and the desired superheat obtained, the crucible is remotely tipped and melt poured into the test section, which is schematically depicted in Fig.2. Pour times from the furnace to test section are 10 seconds or less. This pour time must be kept small in order to minimize melting of the upper surface of the test plate. The test section walls are heated to minimize heat loss, while a distributor plate precludes any direct impingement of the melt onto the lower instrumented plate, representing the vessel wall.

A mechanical plug mechanism is inserted into the initial failure site (D_o) and is removed, once all of the melt has been delivered from the furnace. Initial hole diameters
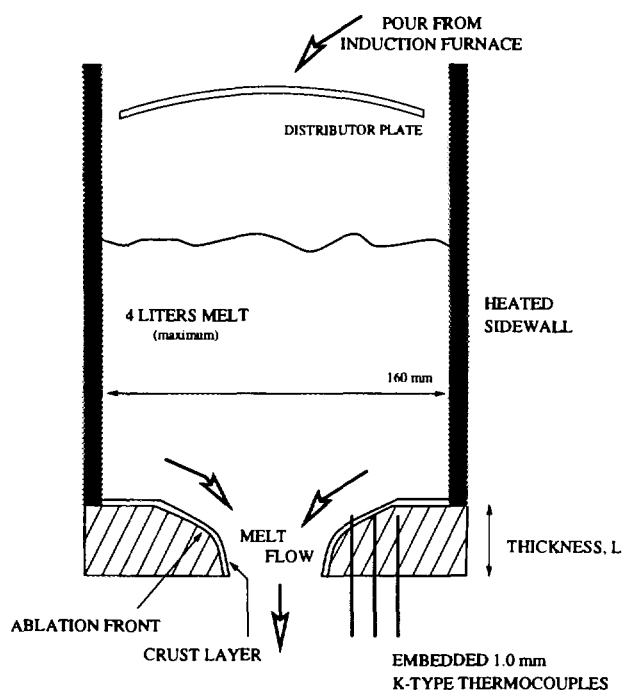
Figure 2: Experimental Arrangement

of both 10 and 20 mm were used. For the 16cm ID test section, a 5 liter melt provides roughly 25cm of melt pool height. Both lead and aluminum plates have been employed as plate materials. Standard 1mm OD K-type thermocouples were embedded within the plates at known radial and axial locations, in order to observe the progression of the melt front and to deduce ablation velocities. The plate size was 0.25x0.25m square, and tests with plate thicknesses of 30 and 40mm were performed for Pb, while thicknesses of 10 and 20 mm were employed when using Al.

The melt was formed from powdered CaO and H_3BO_3, with the water content of the acid evaporated during heating. Chemical analysis of post-test samples revealed reasonably good ($\pm2\%$) control of the mixture composition and thus the liquidus, solidus temperatures and the in-between mushy-zone. Some iron (Fe_2O_3) impurity from the induction crucible has been observed, however its mass percentage has been found to be less than 5%. The presence of the iron compounds serves to slightly lessen the solidus and liquidus temperatures from their reference values. The corrosion characteristics of the melt-crucible are good, allowing for repeated use of the same crucible over several tests. The melt temperature is nominally 1423-1473K which corresponds to a melt superheat in the range of 125-175K. Thermophysical properties, for the melt and the vessel simulant materials employed in the current test program, are provided in Table 1.

Results from the experiments using CaO-B_2O_3 indicated a strong multi-dimensional behavior of the ablation front. Representative tests performed with a 40mm thick Pb

plate provided some insight into the failure site enlargement characteristics. Temperature traces from several of the thermocouples at equivalent radial locations are given in Figure 3 at specific depths from the upper surface. The final shapes of the ablated Pb plates were pressed into epoxy for measurement and assessment. In one test, the 10mm diameter initial hole size was enlarged to a roughly circular 50mm hole at the bottom surface. Midway through the same 40mm thick plate, the final hole was ~60mm in diameter while the uppermost surface was pitted and nonuniform due to the time period of melt-substrate contact prior to flow in the hole. That is to say, in this test, the upper surface was not entirely representative of ablation dynamics, since it suffered some melting prior to removal of the mechanical plug. A second similar test resulted in nonuniform melt discharge and a final elliptical shape hole of dimensions ~50x60mm diameter. In this experiment, only a slight melt flow was observed for the first 30 seconds, however this was followed by an abrupt and rapid discharge period.

Several important aspects are evident from the temperature traces. First, the ablation front speed can indeed be obtained from the data and secondly, there is clear evidence of the crust existence during the course of the tests. Ablation front velocities are in the range of 5mm/s at the upper surfaces and decrease to roughly 1mm/s near the bottom of the plate. Crust behavior is seen in the temperature traces as a momentary "leveling off" in the temperature rise followed by a second rapid rise up to the melt temperature. That is to say, as melt discharge continues, the thermocouples indicate the passing of a crust layer past their location.

Several tests were conducted using the oxidic melt discharge through aluminum plates. However, due to the high thermal conductivity of Al, these tests did not result in ablation but rather a simple discharge of the melt through the hole, coupled with creep of the plate due to the high temperatures and melt mass loading. Pre-heating and insulation of the Al plates did not serve to alter this behavior.

Water as Melt Simulant. A second series of experiments were conducted using water as the melt simulant and salted ice as the simulant vessel wall material. The salt, used in a 10 w/o concentration, allows for a lower temperature melting point (-9°C) and also provides the added benefit of stabilizing the ice block during freezing.

The salt-ice plates were formed in a low temperature (as low as -60°C) freezer and for many of the tests K-type thermocouples were embedded at known distances from the pre-formed cylindrical hole. A test section of 80 liter capacity was used, which employed a slide gate below the melt volume. In this fashion, the water in the test section could be separated from the instrumented ice plate prior to the start of the test. Additionally, the melt simulant volume could be heated or cooled using a separate tank system. Upon opening of the slide gate, the melt (water) comes into contact with the lower plate and begins to ablate the hole as flow is discharged through it. The tank water level was measured, versus time, to provide an indication of the melt discharge rate. A representative
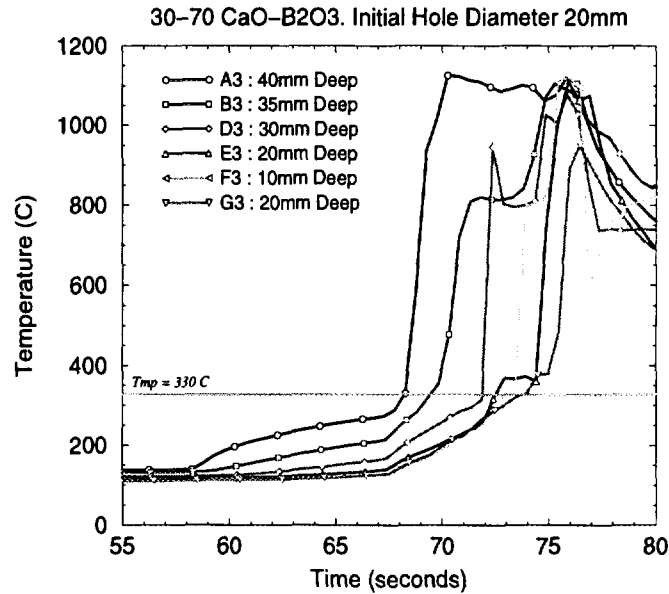
Figure 3: Temperatures - Test 0409

trace of temperatures from the embedded thermocouples in the ice plate is shown in Figure 4. These thermocouples were separated by a distance of 5mm at a depth of 25mm from the top surface. The ablation front speeds measured in this case range between 3.5-$4.0 \cdot 10^{-3}$ m/s. For illustration, accounting for the sensible and fusion heat of the ice plate reveals that an ablation speed of this magnitude corresponds to a heat flux of roughly 0.25 MW/m². In addition, the melt discharged from the ablated hole was collected and its mass measured versus time.

Table 2 provides a listing of all tests conducted using water and ice as simulant materials. The last column in Table 2 shows the measured final hole size immediately after the melt volume has exited. The designation "B" refers to the bottom of the salt-ice plate while "T" refers to the top. Note that the dimensions provided for the final hole size are averaged values since the final hole geometry is not perfectly symmetrical. As can be seen, the tests encompassed variations upon the initial hole size, the melt temperature and the plate thickness. The variability in the initial salt-ice plate temperature is due to the time required to install the plate into the test section, upon removal from the low temperature freezer.

The general observation from these tests was that the final hole geometry was mainly cylindrical, that is to say, there was no significant difference between the diameter at the top or bottom of the salt-ice plates. This differs from that for the earlier oxidic melt experiments where the final plate shapes were multidimensional, exhibiting a much wider entrance diameter (see for example the plate geometry when using PbO-B_2O_3 as melt in

9

Sehgal et al. [13]). This aspect points to the melt viscosity as playing a significant role in the ablation dynamics.

Table 2: Water-Salt-ice Hole Ablation Tests

Test	w/o Salt	D_o (mm)	δ_{plate} (mm)	T_{melt} (°C)	$T_{o,plate}$ (°C)	V_{melt} (liters)	Discharge Time (s)	D_{final} (mm)
0917A	10	20	50	23	-30	78	16	72 B / 72 T
0917B	10	20	50	41	-28	78	12	65 B / 72 T
0918	10	10	60	48	-20	78	14	87 B / 94 T
0919	10	10	60	46	-33	78	15	86 B / 90 T
0923	10	10	60	80	-40	76	12	96 B / 90 T
0925	10	20	60	3	-30	76	77	25 B / 28 T
1002	10	10	38	11	-41	78	27	60 B / 64 T
1015	0	10	80	44	-24	78	14	94 B / 100 T
1016	10	20	79	91	-31	78	10	105 B / 103 T

Some of the water-salt-ice tests employed very low melt temperatures, which resulted in a clean ice crust to form on the upper plate surface and within the ablation hole. This crust layer was measured (post-experiment) to range from 2-5mm in thickness. Obviously, the ablation rates were significantly less for these cases due to the crust formation.
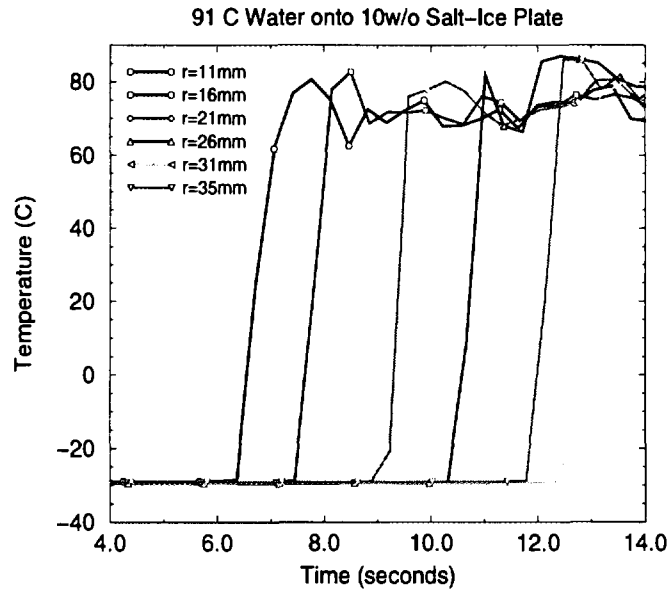

Figure 4: Temperatures - Test 1016

Other Simulants. To examine the influence of melt viscosity, a pair of similar exper-

iments were conducted using paraffin oil as the melt simulant, in conjunction with the 10 w/o salt-ice plate, whose particulars are shown in Table 3. Even with heating of the paraffin oil melt, and, thus, decreasing the melt viscosity and increasing the Reynolds number, the ablation of the initial 20mm hole was not much increased. The final shape of the hole was much different from that observed with the water-salt-ice tests in that the upper region of the hole exhibited a curved or sloped geometry while the bottom of the hole was cylindrical. This points to the fact that because of the very long discharge time, and thus contact time between melt and plate, that multidimensional ablation on the upper surface becomes significant. That is to say, conduction from the melt to the upper plate surface plays a greater role. Also, the higher melt viscosity and Pr number create a thicker dynamic boundary layer and, thus, diminish the role of surface roughness in augmenting heat transfer. This in turn implies a higher entrance-region heat transfer and can also account for the higher ablation rates seen at the upper region of the hole.

Table 3: Paraffin Oil-Salt-ice Hole Ablation Tests

Test	w/o Salt	D_o (mm)	δ_{plate} (mm)	T_{melt} (°C)	$T_{o,plate}$ (°C)	V_{melt} (m^3)	t_d (s)	D_{final} (mm)
1023	10	20	60	29	-37	73.8	128.8	22 B / 30 T
1024	10	20	63	45	-38	69.3	79.7	28 B / 42 T

Another test series employed the binary salt mixture of $NaNO_3$-KNO_3. Both eutectic as well as mushy zone regions of the binary salt mixture phase diagram were employed by varying the composition. In these tests the melt is formed inductively in a 25 liter steel crucible. Similarly to the oxide tests, the melt is poured into the heated test section and the plug mechanism removed from the plate. The most recent results from these tests can be found in Table 4. Comparison of test 1205 with that of 1211 indicates little, if any effect, which can be attributed to the fact that the former test employed a $\approx 60°$C "mushy-region".

More details about binary salt-metal hole ablation tests are provided in Appendix A of the present report.

3 HAMISA Predictions of Hole Ablation Tests

The HAMISA model [14] is a tool for integrated analysis and prediction of pressure vessel hole ablation at both experimental and prototypical scales. The set of phenomena accompanying the vessel hole ablation and melt discharge, are modeled in the code. Heat conduction, and phase change, in the vessel space are calculated in a 2-dimensional

Table 4: NaNO$_3$-KNO$_3$ Salt-Metallic Hole Ablation Experiments

Test	Melt Compos.	Plate Material	D_o (mm)	δ_{plate} (mm)	T_{melt} (°C)	$T_{o,plate}$ (°C)	V_{melt} (m^3)	t_d (s)	D_{final} (mm)
1129	20%-80%	Cerrobend	10	50	450	25	25	12	65 B / 63 T
1205	20-80	Tin	10	50	420	25	25	11	56 B / 54 T
1211	50-50	Tin	10	50	440	50	23	11	60 B / 68 T

formulation and a moving phase change boundary is provided for. Recently, further improvements to the model have been made which address the discharge coefficients, and skin friction as melt exits the failure location.

Improved knowledge, regarding the melt discharge coefficients, has been obtained as a result of a series of tests done at the RIT/NPS laboratory, dealing with water exiting known L/D holes. For relatively long holes, that is L/D ratios greater than $\approx$ 1, values of the discharge coefficients, C_d, of 0.9 - 1.2 were obtained for a range of water temperatures. For shorter holes, the C_d values were predominantly in the range of 0.7 to 0.8. Modifications in the code which arose from these experiments include accounting for both entrance and exit form losses as melt passes through the ablation site. These values are quite different from the typical discharge coefficient of 0.6, which has been used in past studies and taken from flow past orifii. In addition, a model of skin friction factor for the in-hole melt flow has been included in the code. This skin friction factor is an important improvement to the code, since it allows inclusion of surface roughness effects for the in-hole melt flow.

Table 5: HAMISA Validation on Water-Salt-ice Tests

Test	Experiment D_f (mm)	HAMISA D_f (mm)	Experiment t_d (s)	HAMISA t_d (s)	$\Delta D/D_o$ (-)	τ_m/τ_D (-)
0917A	72	70	16	18	2.5	12.6
0917B	69	76	12	15	2.8	22.9
0918	91	87	14	13	7.7	233
0919	88	85	15	13	7.5	219
0923	94	96	12	11	8.6	309
0925	27	24	77	78	0.2	0.5
1002	62	59	27	32	4.9	44.9
1015	96	88	14	12	7.8	228
1016	104	107	10	8	4.4	56

Example simulations using the HAMISA code for several of the water-salt-ice tests in

12

Table 2 are shown in Table 5. Comparisons of final hole size and actual discharge times are found to be in good agreement. This is especially true of the test 0925 which places added demands on the code due to the fact that the low water temperature requires an accurate prediction of the crust behavior during the process. For the above simulations, constant temperature properties were employed along with 2 dimensional representations of the plate material. An in-hole skin friction factor of 0.0055 was employed throughout. The resulting scaling parameters predicted by the HAMISA calculations were shown on Figure 1 previously. It is seen that the use of water-salt-ice provides data in the scaling range needed, especially with respect to penetration type failures.

The comparisons shown in Table 5 were conducted using constant thermal properties. Some uncertainty remains as to precise thermal properties for use in the simulations, yet their impact upon the integral results is not considered to be large.

HAMISA predictions of the hole ablation tests using oxide and binary salt as working fluids are presented and discussed in Appendixes of the present report. In general, very good agreement between the experimental data and calculated results was obtained.

4   Summary and conclusions

An experimental program at RIT/NPS has been conducted, which aims to reduce the uncertainty level associated with ablation dynamics of a failure site in the RPV lower head. There is very little scaleable experimental information available regarding failure site growth dynamics resulting from the flow of a fluid at temperatures greater than the melting point of structure. An important aspect is the impact of a mushy-region crust layer, which can form, and reduce the ablation rate and the final area of the failure site. Clearly, this issue is important since the melt discharge rate from the failure site location will determine the major containment loading during a severe accident.

Various melt and vessel wall simulants were employed in the test program, in order to, better, examine the influence of material properties upon the ablation phenomena. It was realized that the melt viscosity plays an important role in hole ablation. That is because the crust layer of melt which can form upon the ablating hole will undoubtedly exhibit a significant surface roughness. In lower viscosity melts the thickness of the boundary layer is small enough that the surface roughness governs the heat transfer, thereby minimizing any entrance effects, and producing a much more uniform (one-dimensional) ablation. In the experimental program, it was found that for the higher viscosity melts (binary oxide and paraffin oil) the final hole shape was very much two-dimensional, with a significantly wider "mouth", or upper surface, than the exit. Conversely, with the water and salt melt simulants the ablation profile may be characterized as one-dimensional. In all of the experiments, it was clear that the crust boundary condition prevails all the time, i.e., the

temperature difference driving the ablation is the melt temperature and the melt liquidus temperature (i.e. $\Delta T = T_{melt} - T_{liq}$). Thus, even though the crust may be swept out by the melt flow, it re-establishes itself i.e., and the time required for crust formation appears to be much less than the rate of crust sweep-out.

The experimental program on hole ablation demonstrated:

i) the discharge coefficients of vessel hole ablation is closer to 1.0 than to 0.6;

ii) the crust boundary condition persists through the whole scenario, reducing the heat transfer to the vessel wall and its ablation. It is believed that melt superheat i.e. $\Delta T = T_{melt} - T_{liq}$ should be used for determining the heat transfer;

iii) the ablation process appears to create a rough surface, which promotes a high heat transfer coefficient from melt to interface;

iv) for low Prandtl number fluids (corium), the thermal boundary layer thickness may be less than the roughness height. Thus, the heat transfer may be represented as a function of the viscosity-independent Peclet number $(Pe = Re.Pr)$.

It is believed that the HAMISA model could be employed, with confidence, to predict the hole ablation dynamics process during the prototypic accident scenarios.

It is believed that the hole ablation phenomenology is quite well understood.

NOMENCLATURE

Δh_{fus}	Heat of fusion, J/kg
T	Temperature, K
V_{melt}	Melt volume, dm^3
t_D	Melt discharge time, s
τ_m	Discharge time without ablation, s
τ_d	Characteristic hole growth time, s
$\Delta D_o/D_o$	Characteristic Size Ratio
D_o	Initial hole size, m
κ	Heat conductivity, W/m·K
μ	Dynamic viscosity, Pa.s
δ_{plate}	Plate thickness (mm)

Subscripts

mp, w	Melting point of wall material

o	initial
l, liq	liquid, liquidus
s, sol	solid

References

[1] Rempe, J. L., G. L. Thinnes, S. A. Chavez, "A Simpler Approach for Predicting LWR Vessel Failure During Severe Accident Conditions," Nuclear Engineering and Design, Vol.148, pp 365-383, (1994).

[2] Rempe, J. L. and T. J. Walker, "Overview of NRC Sponsored LWR Lower Head Failure Research Program," Nuclear Engineering and Design, Vol.148, pp. 327-341, (1994).

[3] Chavez, S.A. and J.L. Rempe, "Finite Element Analyses of a BWR Vessel and Penetration under Severe Accident Conditions," Nuclear Engineering & Design, Vol. 148, (1994), pp. 413-435.

[4] Green, J. A., T. N. Dinh, W. Dong, and B. R. Sehgal, "Experiments on Melt Jet Impingement and Vessel Hole Ablation Phenomena", PSA'96 - International Topical Meeting on Probabilistic Safety Assessment, Park City, Utah, (1996).

[5] Theofanous, T. G., C. Liu, S. Addition, S. Angelini, O. Kymäläinen, and T. Salmassi, "In-Vessel Coolability and Retention of a Core Melt," DOE/ID-10460, Vol. 2, (July, 1995).

[6] Witt, R.J., "Local Creep Rupture Failure Modes on a Corium-Loaded Lower Head," Nuclear Engineering & Design, Vol. 148, (1994), pp.385-411.

[7] M.M. Pilch, "Continued Enlargement of the Initial Failure Site in the Reactor Pressure Vessel", Nuclear Engineering & Design, Vol. 164, (1996), pp. 137-146.

[8] Pilch, M. M., Y. Yan and T. G. Theofanous, "The Probability of Containment Failure by Direct Containment Heating in Zion", NUREG/CR-6075 and SAND93-1535, (June, 1993).

[9] Sienicki, J.J. and B.W Spencer, "Superheat Effects on Localized Vessel Breach Enlargement During Corium Ejection", Trans. ANS, Vol. 52 (1986), pp.522-524.

[10] Zion Probabilistic Safety Study, Commonwealth Edison Co., Chicago, IL. 1981.

[11] Sienicki J.J. , C.C. Chu, B.W. Spencer, W. Frid, and G. Löwenhielm, "Ex-Vessel Melt-Coolant Interactions in Deep Water Pool: Studies and Accident Management for Swedish BWRs", Proceedings of the CSNI Specialist Meeting on Fuel-Coolant Interactions, Santa Barbara, January 5-8, 1993, NUREG/CP-0127, NEA/CSNI/R(93)8.

[12] Sehgal B.R., J. Andersson, T.N. Dinh and T. Okkonen, "Scoping Experiments on Vessel Hole Ablation During Severe Accidents", Proceedings of the Workshop on Severe Accident Research in Japan, SARJ-4, Japan, Oct.-Nov., 1994, pp.230-236.

[13] Sehgal, B. R., V.A. Bui, T.N. Dinh, J. Andersson and T. Okkonen, "Experiments on Vessel Hole Ablation During Severe Accidents", Proceedings of the International Seminar on Heat and Mass Transfer in Severe Reactor Accidents, Izmir, Turkey, 1995.

[14] Dinh, T. N., V.A. Bui, R.R. Nourgaliev, T. Okkonen and B.R. Sehgal, "Modeling of Heat and Mass Transfer Processes During Core Melt Discharge from a Reactor Pressure Vessel," Nuclear Engineering and Design, Vol. 163, pp. 191-206, (1996).

Appendix A: Review of Salt-Metal Hole Ablation Experiments

Abstract

This section provides a summary of the four (4) hole ablation tests conducted at RIT/NPS using salt as melt simulant and low melting point metals as vessel steel simulant. These tests were conducted using the larger induction furnace coil and therefore provide for melt volumes of just under 25 liters. As a result, they provide good scaling to prototypical penetration failures. Modeling of these experiments with the HAMISA code is also described.

A-1   Introduction

A severe accident in a nuclear power plant could result in the generation of substantial volumes of high temperature oxidic corium and/or metals. Once generated, this melt can be involved in a variety of phenomena of importance to reactor safety which are highly scenario and design dependent. One such phenomena is the formation of a melt pool in the lower plenum of the reactor pressure vessel (RPV) due to melt relocation, which subsequently results in failure of a lower head vessel penetration (CRDM or drain line in a BWR or instrumentation nozzles in a PWR). Flow of the melt pool fluid through this failure site will in turn result in enlargement of the hole, and thereby increase the rate of melt discharge into the containment.

The ablation of the vessel steel by the discharging melt involves several complex phenomena such as; moving phase change boundaries, multidimensional conduction in the vessel steel and crust formation for an oxidic material which melts over a particular temperature range $(T_{liq}\text{-}T_{sol})$.

A substantial research program has been directed into the understanding of the hole ablation process at RIT/NPS. This report describes a series of tests which were conducted using molten $NaNO_3$-KNO_3 salt mixtures as corium simulant and the low melting point Cerrobend alloy as well as tin (Sn) as RPV plate materials.

Four experiments were conducted in this test series. All four tests were reasonably successful and thereby provide a valid database for the benchmarking of the mechanistic HAMISA code developed by RIT/NPS. This test series also provided valuable experience for future tests which involved higher temperature oxidic melt simulants.

17

A-2 Description of Tests

A set of four salt-metal hole ablation tests were conducted in the MIRA (Melt Interactions in Reactor Accidents) facility. Table A-1 provides a description of the relevant test conditions.

Table A-1: RIT/NPS Salt Metal Test Parameters

Test Date	Melt	Plate	D_o (mm)	T_{melt} (°C)	Volume (liters)
1024	20-80 w/o (Na,K)NO$_3$	Cerrobend	20	350	22
1129	20-80 w/o (Na,K)NO$_3$	Cerrobend	10	450	23
1205	20-80 w/o (Na,K)NO$_3$	Tin	10	450	23
1211	50-50 w/o (Na,K)NO$_3$	Tin	10	440	24

Individual reports regarding the specifics of each test can be found in the applicable directories in the RIT/NPS user4 storage disk. Physical properties for the melt and cerrobend alloy can be found in the report by Green [1]. Tin properties can be found in Incropera [2].
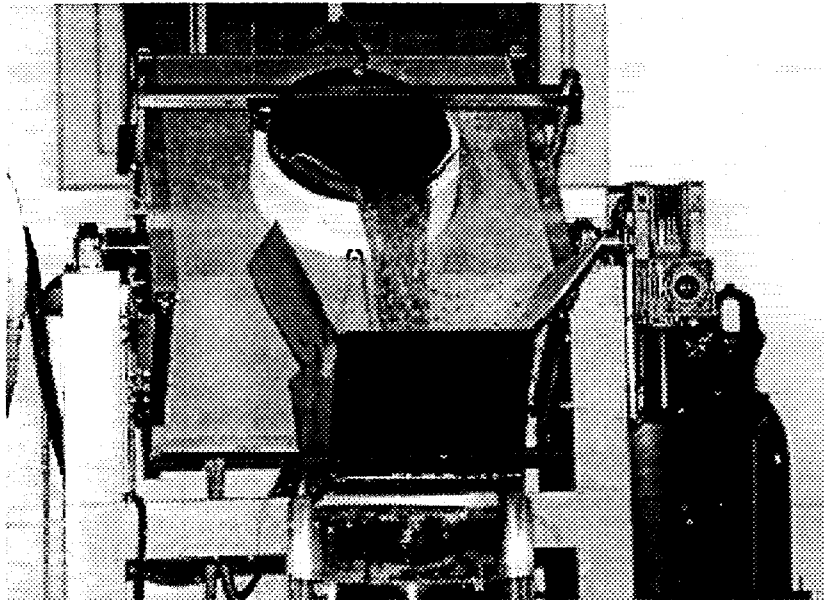
Figure A-1: Pouring of Salt Mixture into Test Section.

In each of the above tests the induction furnace arrangement, the test section into which the melt was poured, and the plate geometry were identical (Figure A-1). Additionally the embedded thermocouple locations in the metal plates were the same (Figure A-2).

18

The melt crucible has a 270mm ID with a 17mm thick wall. It is made of common C-steel. The height of the crucible is 480mm which provides for a maximum melt volume of 27.5 liters. The actual melt height is always somewhat lower than this to avoid any spillage. The salt mixture is weighed out in the proper proportions and mixed thoroughly. The melt is generated by induction heating of the steel crucible. As the powder melts, additional salt is added. The generation time for just under 25 liters of melt is approximately 2 hours at power levels of 20-30 kW. Note that there is an initial period during which the crucible is heated to its curing point of $\sim700^\circ$C. In this period a maximum of only 10-15 kW can be supplied by the generator.

Once the melt has been formed it is remotely tipped into the pre-arranged test section. This test section is 257.5mm ID and 500mm in height. The section is heated using 4 band heaters. The melt is poured into the section via a pour spout and umbrella in order to preclude any direct melt impingement on the plate. Once the melt has been delivered into the test section the pre-installed plug is removed to allow the melt flow to discharge through the instrumented plate. In most tests the scale apparatus was installed to collect the mass discharged from the ablating hole. This was then recorded by the PC data acquisition (DAS) system and manipulated to provide a mass discharge rate in time.
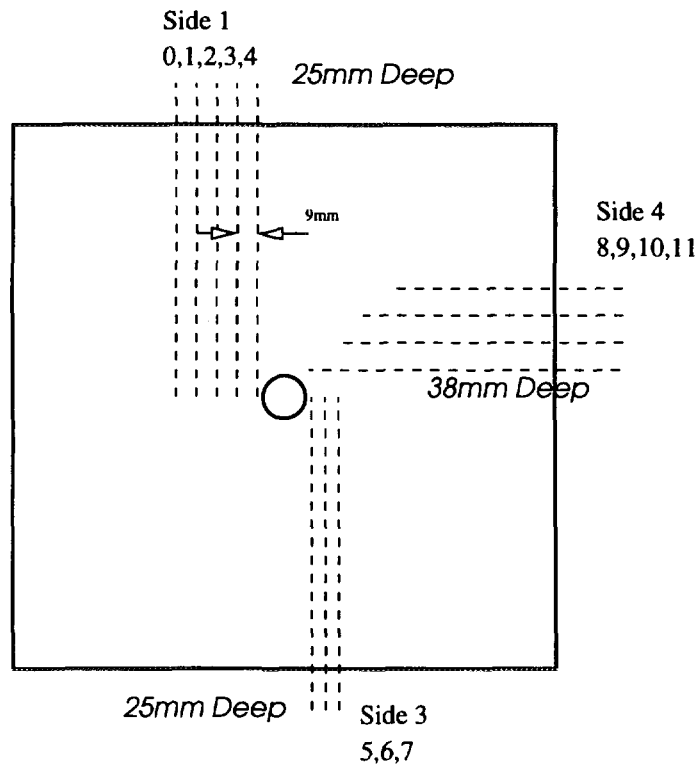

Figure A-2: Arrangement of Embedded Thermocouples.

In all cases the plate was 50mm thick. In all tests except that of 1024 the initial hole size was 10mm and a plug mechanism was installed to prevent any melt flow prior to all

of the melt being delivered into the test section. For the 1024 test, a 20mm initial hole was used without any plug mechanism (thus melt was being ejected as soon as it was remotely tipped into the test section).

Twelve 1mm OD K-type thermocouples were embedded in the test plates and connected to the HP DAS for scanning. These thermocouples are arranged as shown schematically in Figure A-2 and which can be seen in the photograph of Figures A-3-A-4.
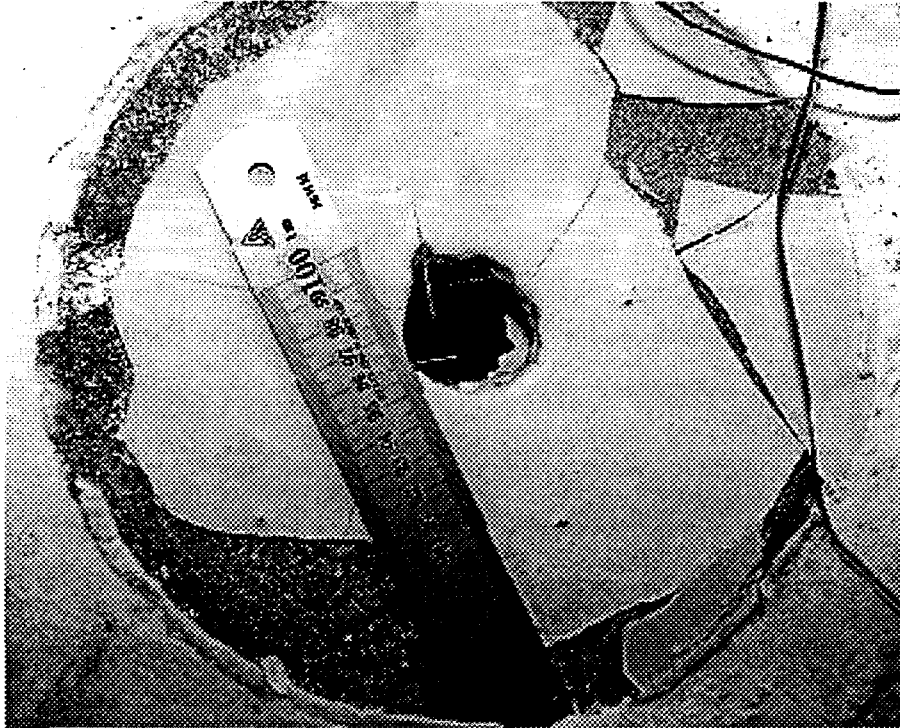

Figure A-3: Test 1024.

A-3   Experimental Results

The information from these tests falls into 2 main categories; (i) integral results such as the final hole size (D_f) and the discharge time (t_d) and (ii) dynamic results such as the ablation front progression (V_{abl}) and rate of melt discharge. All of the tests provided results from the first category. The latter category depends upon the installed instrumentation whose success is not always guaranteed.

The applicable 'integral' type results are presented in Table A-2. Recall that test 1024 is unique in that the plug mechanism was not used there.

Interestingly, the lower surface diameters are in some cases larger than those at the
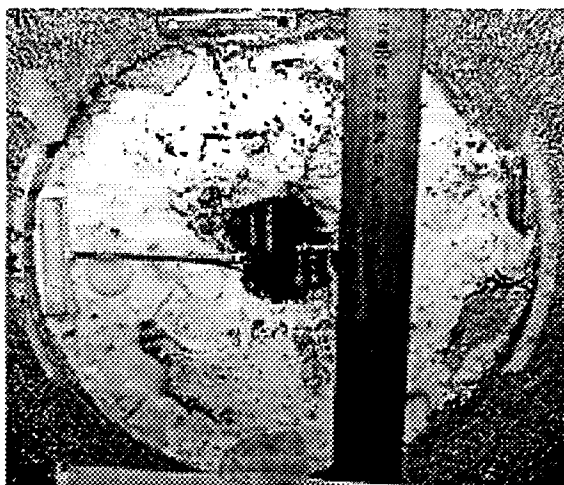
20

Figure A-4: Test 1129.

Table A-2: RIT/NPS Salt-Metal Integral Results

Test Date	D_o (mm)	$D_f{}^T$ (mm)	$D_f{}^B$ (mm)	t_d (s)	t_{pour} (s)
1024	20	49	48	31	10
1129	10	63	70	12	9
1205	10	54	56	12	10
1211	10	68	60	12	9

top surface. This is indeed the case although it must be realized that the hole size measurements are slightly subjective (i.e. where to place the ruler) and also that the numbers in Table A-2 represent an average of measurements taken every 45° around the final hole. The geometry of the ablated holes is not always exactly cylindrical and as a rule the difference in diameter at differing angles never exceeded 6mm.

Another common aspect to these tests is the fact that the diameter of the plate at the center depth is typically the greatest. Indeed, the final hole shapes were often "hourglass" shaped. Also of importance is the fact that for the 2 cerrobend plate tests, the plate itself had some "gaps" which formed during the cooling-off as the plate was formed. It is impossible to ascertain the effect of these gaps on the ablation process. It would not seem to have a major impact however, in one test (1205) it was seen from the video that a path for melt flow developed *away* from the preformed initial hole (Figure A-5). Thus, there exists some inherent voiding of the plate materials which is difficult to avoid. The impact of this plate voiding on the overall results is difficult, if not impossible, to quantify. Finally, all measurements are to some extent intrusive on the process to be measured. The embedded plate thermocouples are no exception. They are relatively large at 1mm and
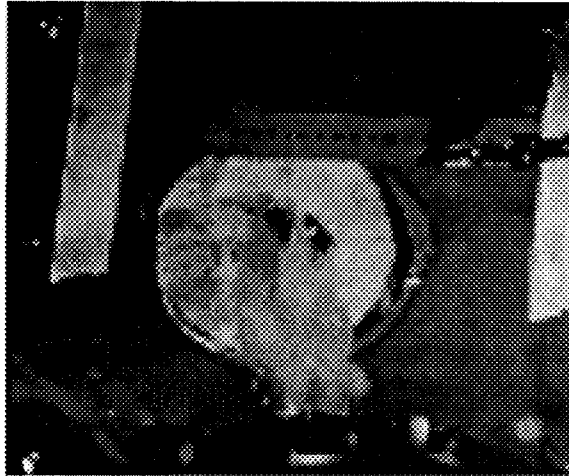
Figure A-5: Discharge of Melt from Bottom of Plate (Test 1205).

certainly have some effect on the flow field in the hole flow. Given other experimental uncertainties however, this is not considered to be a major contributor.

A selection of pictures taken of the ablated plates is presented in Figures A-3 through A-6.

Notice from Table A-2 that the applicable integral scaling parameter of the hole growth to that of the initial hole size ranges from 4.5 to 5.7 for the tests with 10mm initial diameter. This clearly places them into the desired prototypically scaled penetration failure range (see Pilch [3]).

As for *dynamic* measurements, test 1205 was unsuccessful in providing ablation front progression measurements due to the fact that trouble with the tilting mechanism resulted in the DAS "timing out". Also, test 1024 did not reveal sufficient ablation so as to cover several thermocouples (due first to the larger hole size and secondly to the lack of plug).

For each of the 4 tests the collected mass was recorded. This measurement and its time derivative is provided in Figures A-8 to A-11. It can be seen that the discharge times are approximately the same as shown in Table A-2. The differentiation of the mass collected provides a slightly longer discharge period ($\sim$1s) as a result of the fact that some melt continues to drip out after gas blowthrough has taken place.

Results from the embedded thermocouples is provided in Figures A-12 to A-17. From these figures it becomes evident that the actual cerrobend alloy melting point is not 70°C. It would appear that the melting point is much closer to 80°C as was measured in [1]. Tests 1129 and 1211 provide some indication of the ablation front velocity. These results are summarized in Table A-3.
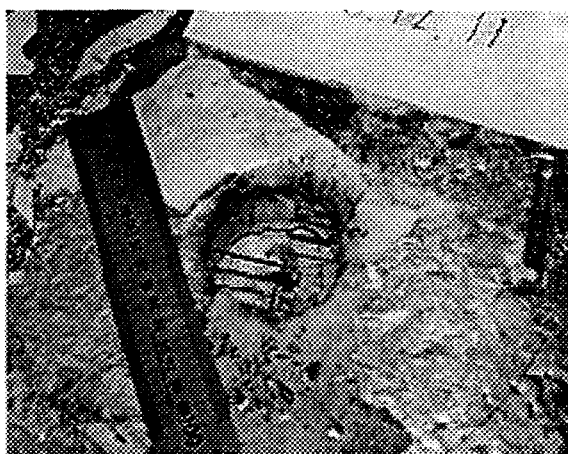
Figure A-6: Test 1211.

Table A-3: Ablation Velocities

Between TC's	V_{abl} 1129 (mm/s)	V_{abl} 1211 (mm/s)
0 - 1	2.4	2.7
1 - 2	2.8	1.8
5 - 6	n/a	3.5
6 - 7	1.6	3.8
8 - 9	2.8	1.8
9 - 10	2.5	2.8

It must be noted however that even a small deviation in the position of the thermocouples (which is likely given the manner in which the plate was formed) will produce significant changes in the calculated ablation speed. A separation between thermocouples of 9mm is the best estimate however. In addition, there appeared some very hard solid "lumps" which were caught on the thermocouples in test 1211.

Finally, it was seen for the salt-cerrobend tests that the upper surface of the cerrobend plate was melted over the entire test section geometry. The depth of this melting was as much as 10mm. A non-uniform mix of the alloy and salt was realized on the top surface of the plate. This was not true of the subsequent tests using the higher melting point Sn.

A-4 Modeling with HAMISA Code

These tests were employed for validation of the HAMISA code. Although an initial attempt at modeling of the 1024 test was made, it proved to be unsuccessful due to the

23

fact that mass was discharged as soon as it was delivered. The subroutines were modified to allow for this (and also to prevent the code from stopping due to gas blowthrough) however the rate at which the mass is added to the test section is very difficult to include since it changes in time at an unknown rate. The remaining 3 tests were modeled using HAMISA using the property database provided in [1]. The greatest uncertainty in properties appears to be that of the melting temperature and mushy behavior of Cerrobend. In these simulations a melting temperature of 75°C was used with a 5°C freezing zone. It appears likely that as the Cerrobend is repeatedly used, it oxidizes to some extent and therefore the melting point increases and also a larger mushy zone results.

Table A-4: HAMISA Validation on Salt-Metal Tests

Test	HAMISA Options	Experiment D_f (mm)	HAMISA D_f (mm)	Experiment t_d (s)	HAMISA t_d (s)
1129	f=0.0055, MODS=0	63/70	64/74	11	9
1129	f=0.0055, MODS=1	63/70	64/68	11	9
1205	f=0.0055, MODS=0	54/56	50/53	12	12
1205	f=0.0055, MODS=1	54/56	50/51	12	12
1211	f=0.0055, MODS=0	68/60	55/58	12	12
1211	f=0.0055, MODS=1	68/60	55/56	12	12

The results are quite good as can be seen. This has been achieved with a minimum of "tuning" of the input parameters for these tests. It is likely that the remaining discrepancies between experimental and predicted parameters are due to remaining uncertainties in the thermophysical parameters. In addition, it is very difficult to know the exact volume of melt which is available for ablation. That is due to the fact that some material remains on the induction crucible, some on the pouring spout and umbrella and some on the test section walls. Differences in melt volume input to the code can have significant effects upon the predicted results. Note also that although Table A-4 provides sizes of 68/60 mm for the bottom and top dimensions in test 1211, these are in reality averages of different measurements. At 45° angles the actual upper surface yielded dimensions of 62, 71, 70 and 68 mm and the bottom of 63, 62, 57, and 58mm. (i.e. the holes were not entirely cylindrical). The HAMISA predictions are well within this uncertainty.

Extensive sensitivity calculations were performed. It is found that the driving temperature difference governing the hole ablation process is that between the melt and its liquidus point (T_{melt}-T_{liq}) rather than the solidus point. This is tested in the HAMISA model by artificially changing the salt mixture liquidus point to values closer to the solidus point with the results being that large differences in predicted hole sizes and discharge times were realized. Changes in solidus temperature, while maintaining the proper liquidus temperature yielded no changes in results.

A-5 Summary

This report has presented an overview of 4 hole ablation experiments conducted in the RIT/NPS laboratory using $NaNO_3$-KNO_3 salt as melt and either cerrobend alloy or tin as plate material. The experiments performed have provided well-scaled data points for reactor penetration-type failures. Additionally, the HAMISA code was validated using these tests with reasonable results.

Some conclusions can be made from these experiments;

- The experiments provide the only known database of hole ablation tests for proto-typically scaled penetration-type failures.

- The final hole sizes and discharge times are well predicted by the HAMISA code.

- The final hole geometry was primarily cylindrical, thus indicating minor multidimensional effects. This can be attributed to the phase-change surface roughness which minimizes any entrance region effects.

- There appears to be little impact due to the composition of the binary salt mixture. The test conditions between 1205 and 1211 were approximately similar except for the melt composition. Yet the final hole size is not significantly changed. In fact, the slightly larger final hole in test 1211 is more likely due to a slightly larger volume and 10 additional degrees of melt temperature.

- From these tests it is found that the driving temperature difference governing the hole ablation process is that between the melt and its liquidus point (T_{melt}-T_{liq}) rather than the solidus point.

References

[1] Green, J.A., "Thermo-Physical Properties of Cerrobend Alloy and $NaNO_3$-KNO_3 Salt Mixtures," Research RIT/NPS Report (NPS-LAB-01-97), January, 1997.

[2] Incropera, F.P., and Dewitt, D.P., "Fundamentals of Heat and Mass Transfer", John Wiley and Sons, New York, 1990.

[3] Pilch, M.M. "Continued Enlargement of the Initial Failure Site in the Reactor Pressure Vessel", J. Nucl. Eng. Des., Vol. 164, pp.137-146 (1996).
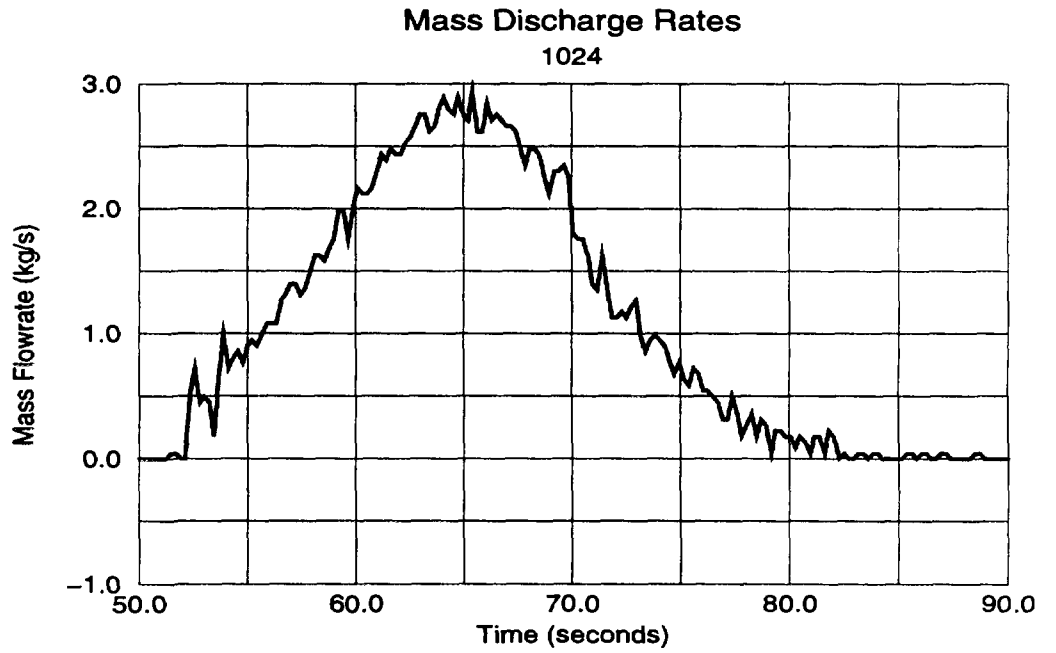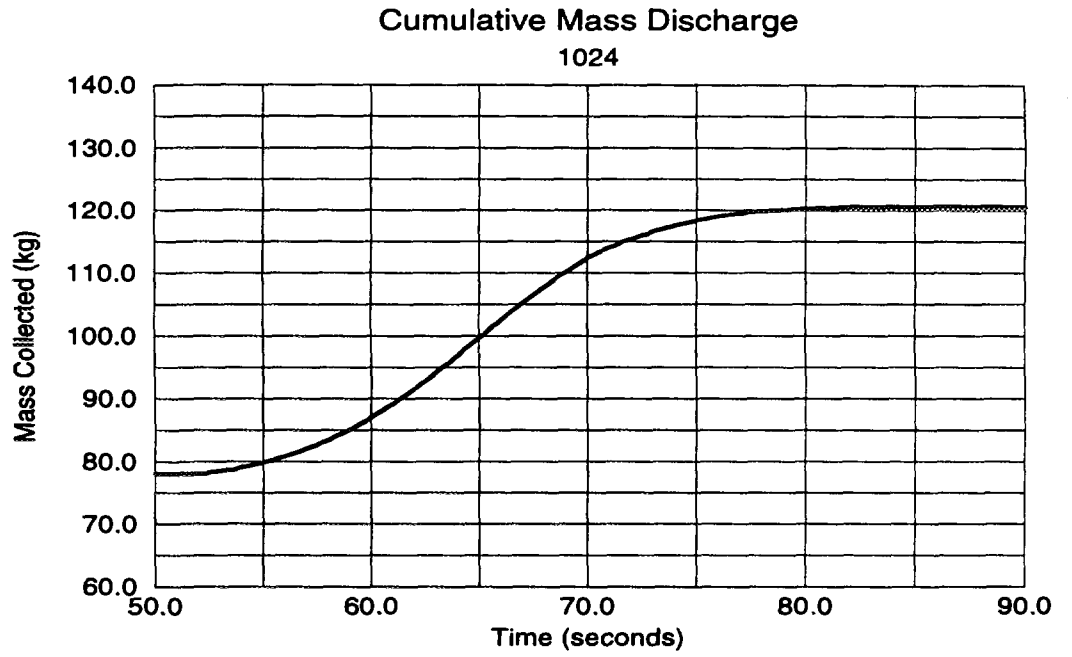
Figure A-7: Test 1205.

Cumulative Mass Discharge
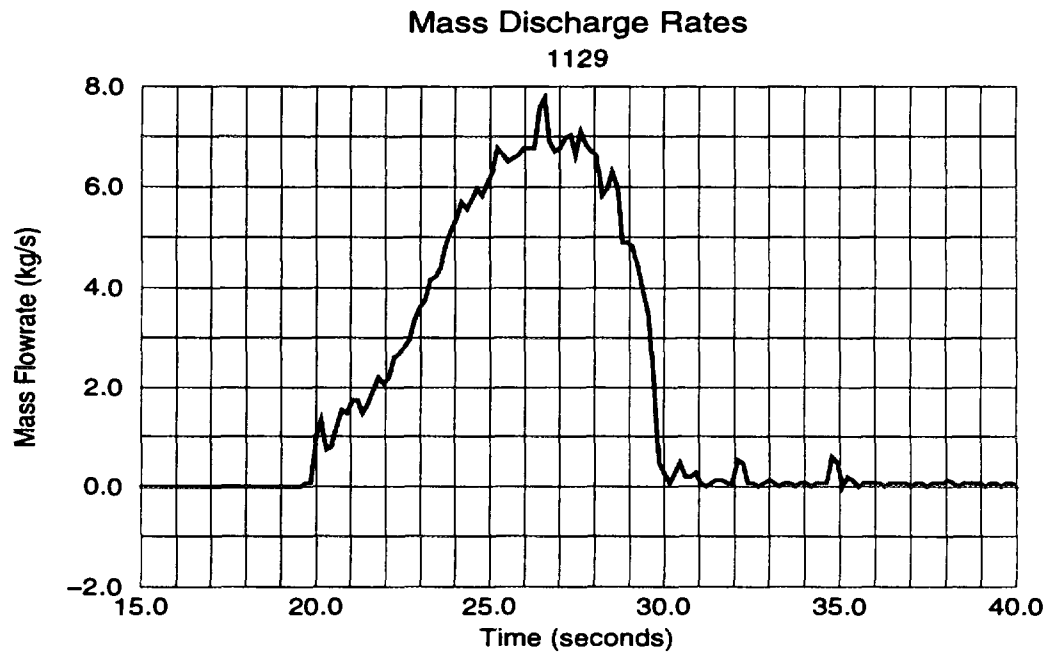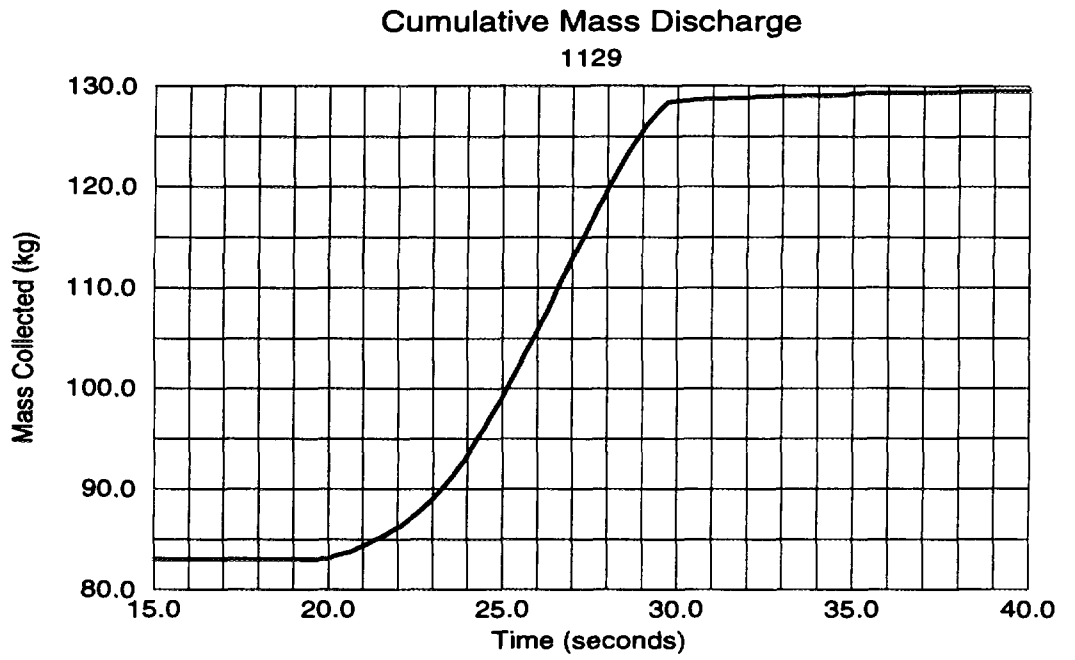### 1024

Mass Discharge Rates
1024

Figure A-8: Mass Discharge Data for Test 1024.

27

Figure A-9: Mass Discharge Data for Test 1129.

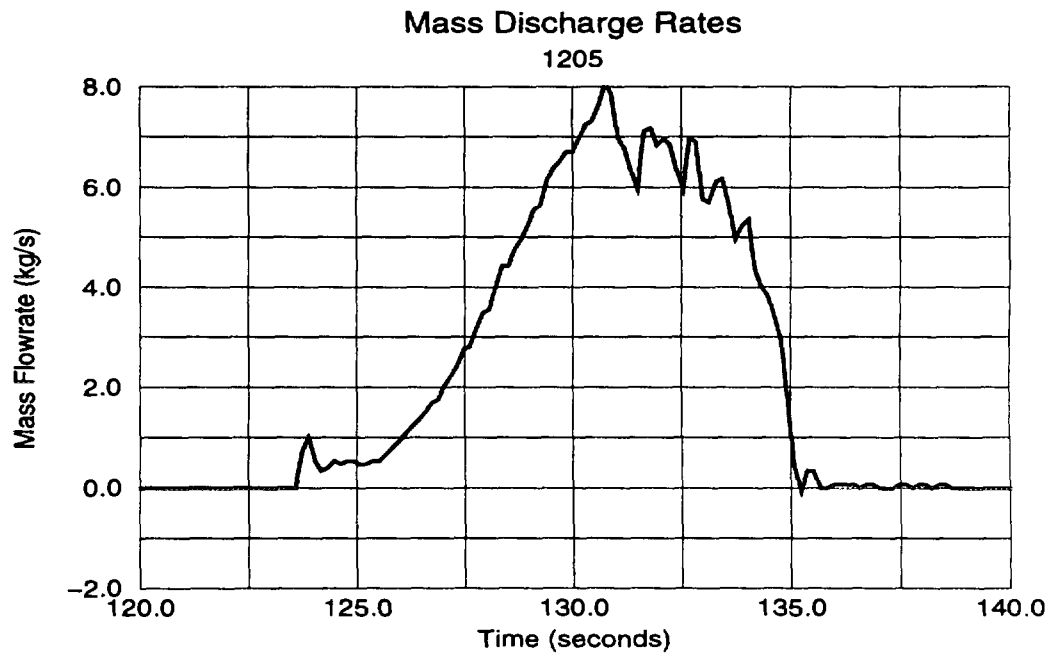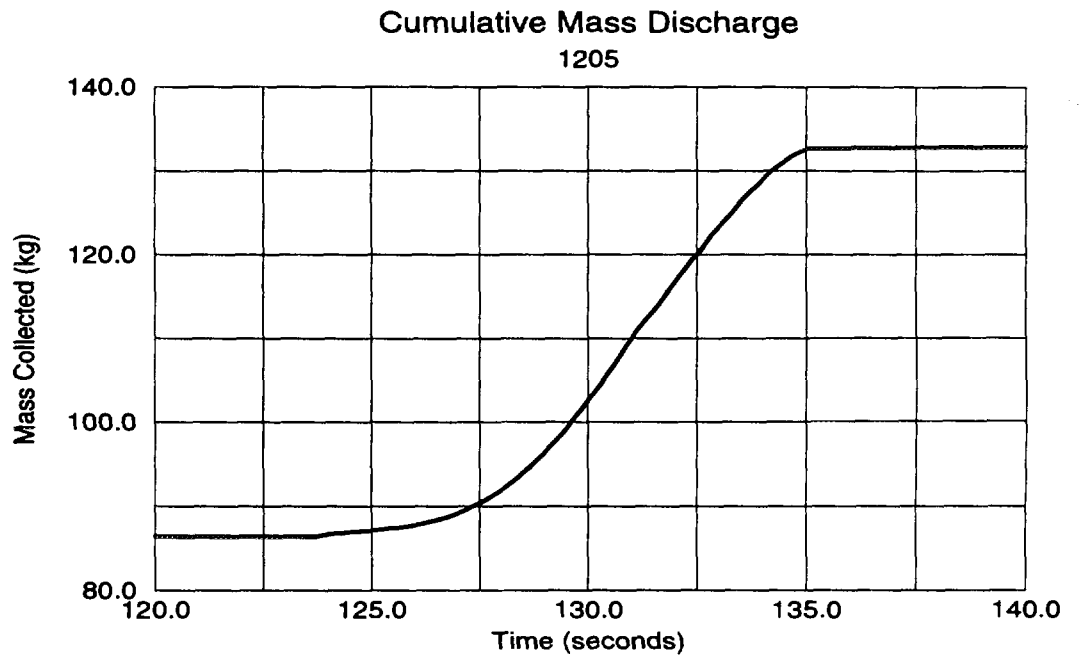## Cumulative Mass Discharge
1205

Mass Discharge Rates
1205

Figure A-10: Mass Discharge Data for Test 1205.

29

Cumulative Mass Discharge
1211

Mass Discharge Rates
1211
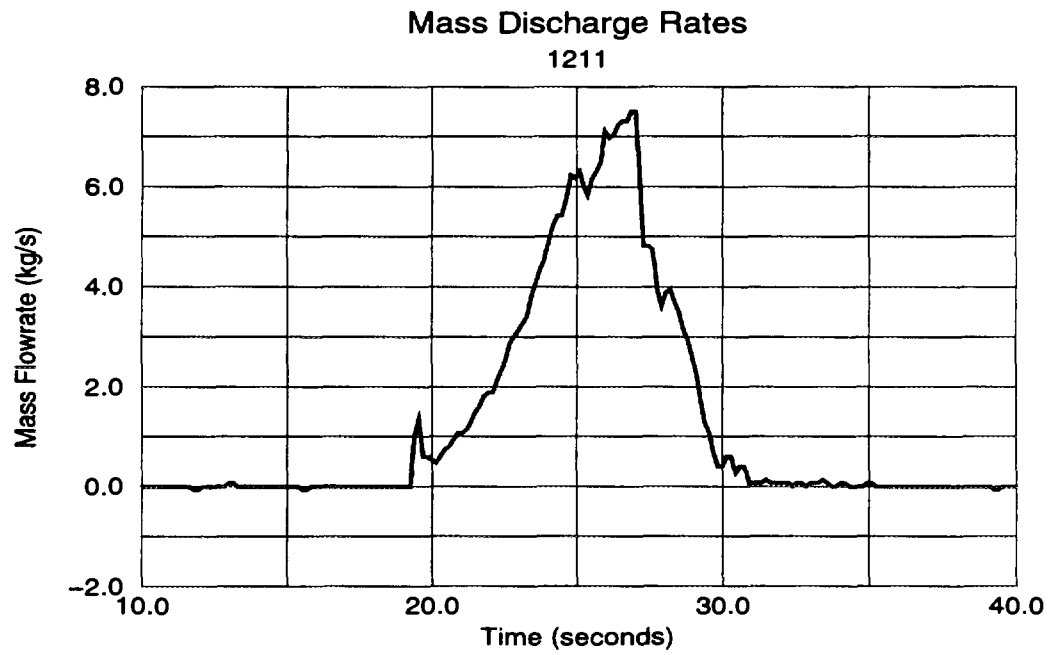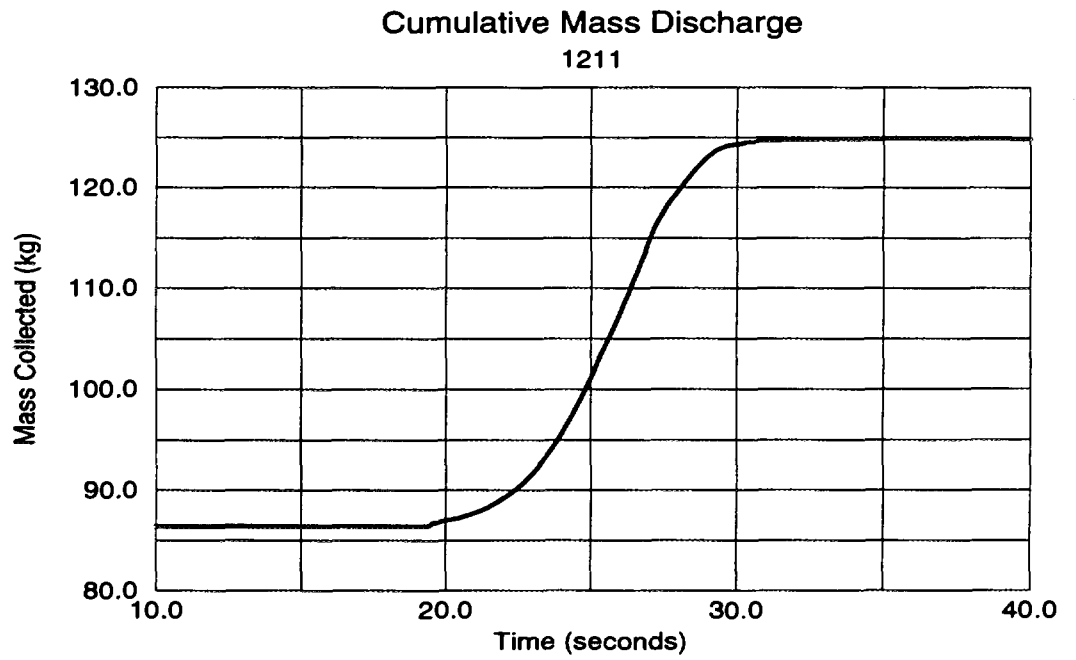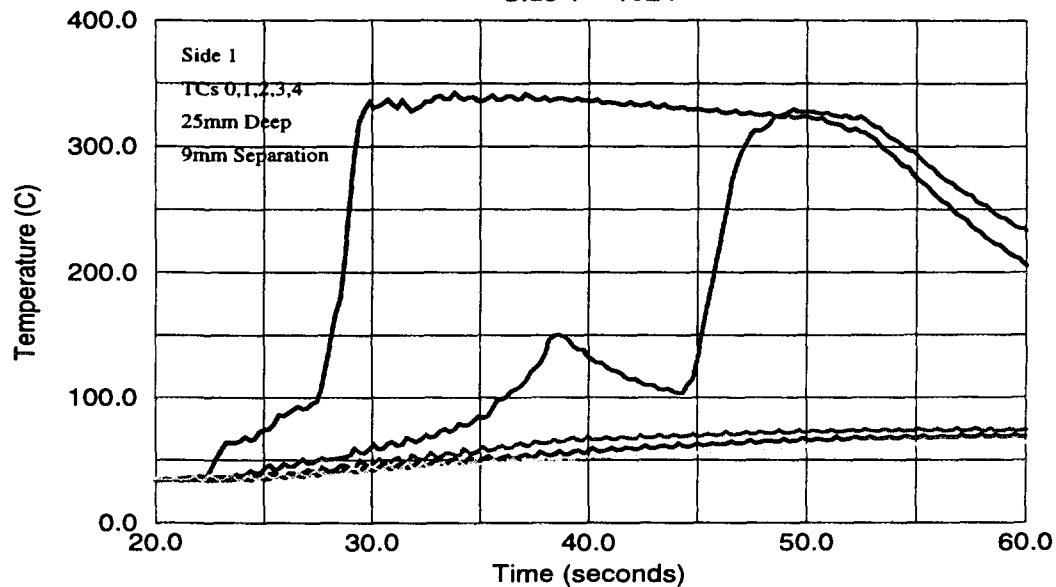
Figure A-11: Mass Discharge Data for Test 1211.

30

Embedded Thermocouple Response
Side 1 – 1024

Side 1
TCs 0,1,2,3,4
25mm Deep
9mm Separation

Temperature (C)

Time (seconds)

Embedded Thermocouple Response
Side 3 – 1024

Side 3
TCs 5,6,7
25mm Deep
9mm Separation

Temperature (C)

Time (seconds)
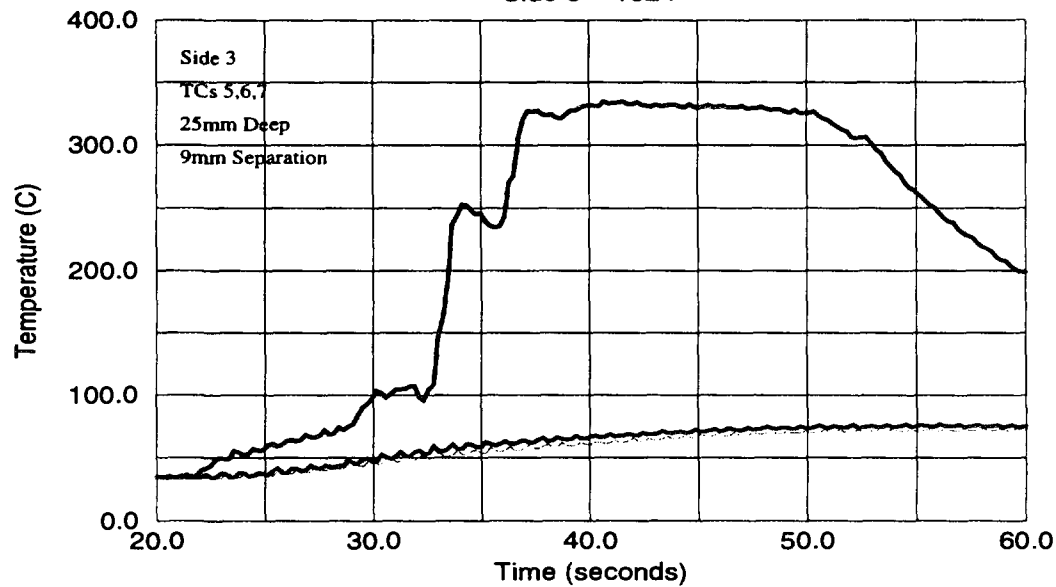
Figure A-12: Temperatures - Salt-Cerrobend Hole Ablation Test 1024.

31

Embedded Thermocouple Response
Side 4 – 1024

Side 4
TCs 8,9,10,11
38mm Deep
9mm Separation

Temperature (C)

400.0

300.0

200.0

100.0

0.0

20.0   25.0   30.0   35.0   40.0

Time (seconds)

Test Section Thermocouple Response
1024

Temperature (C)

400.0

300.0

200.0

100.0

0.0

TC 12 – in Test Section (Melt Tempreature)

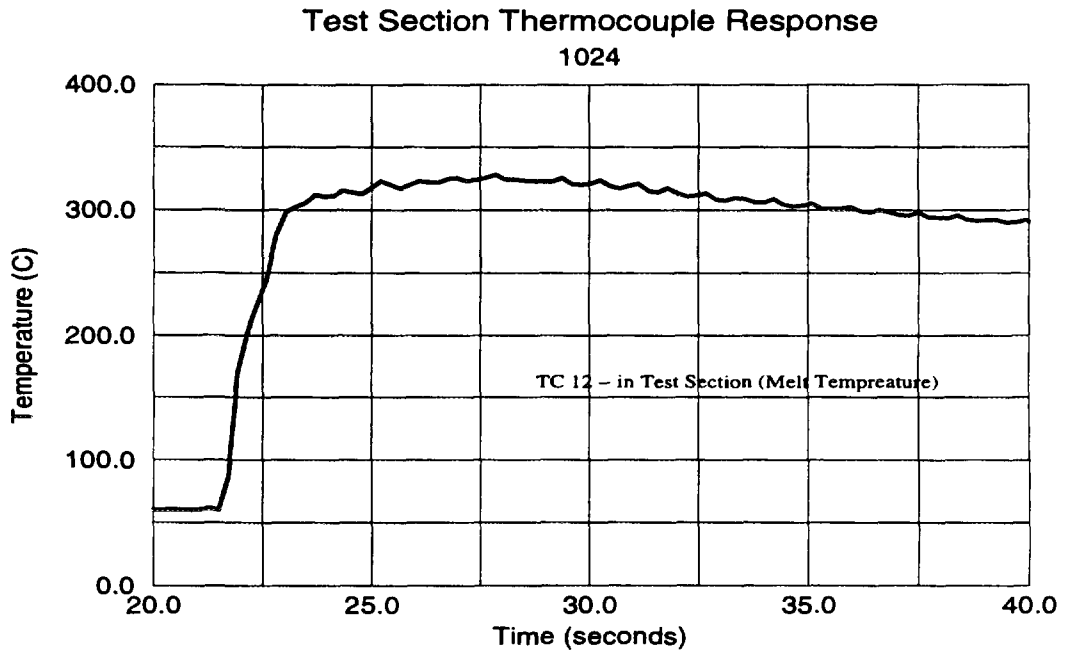20.0   25.0   30.0   35.0   40.0

Time (seconds)
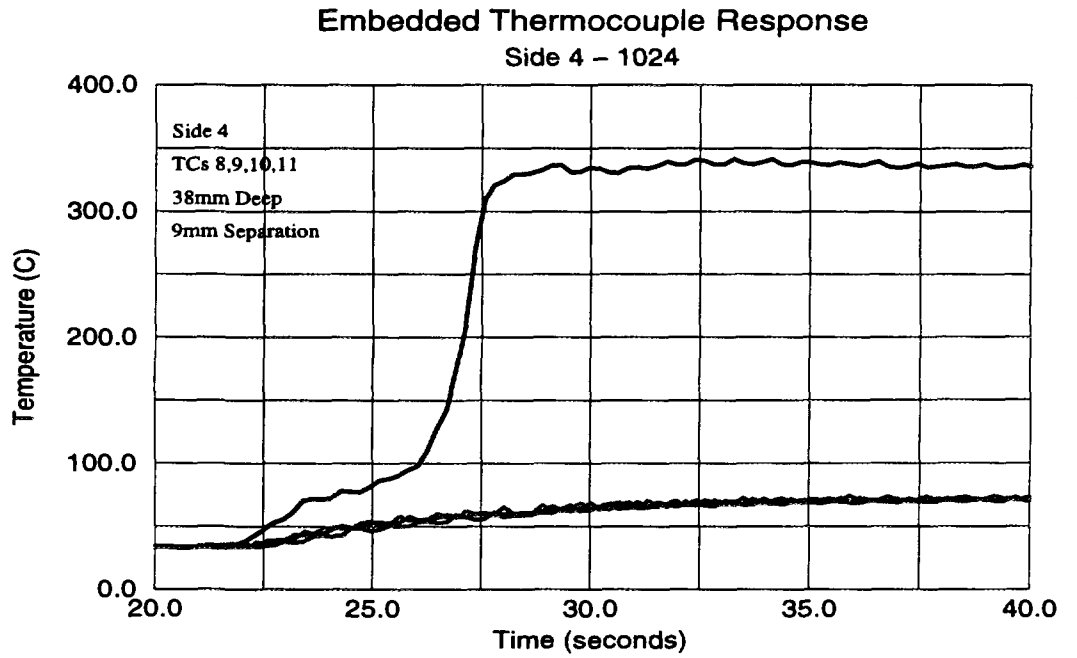
Figure A-13: Temperatures - Salt-Cerrobend Hole Ablation Test 1024.

32

Embedded Thermocouple Response
Side 1 – 1129

Side 1
TCs 0,1,2,3,4
25mm Deep
9mm Separation

(Temperature (C) vs Time (seconds))

Embedded Thermocouple Response
Side 3 – 1124

Side 3
TCs 5,6,7
25mm Deep
9mm Separation
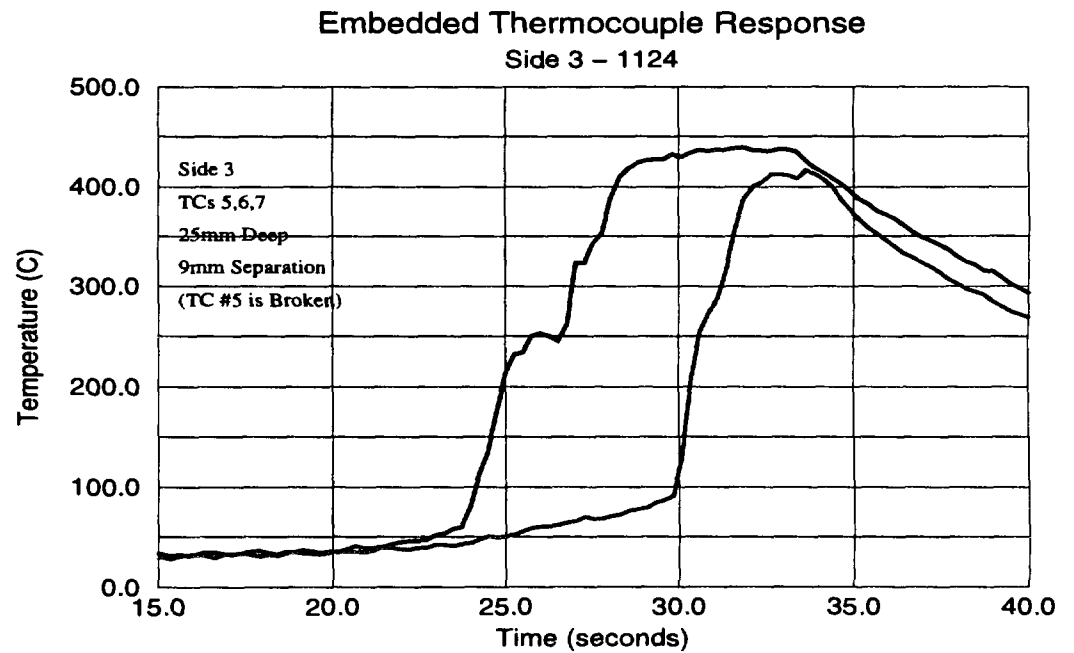(TC #5 is Broken)

(Temperature (C) vs Time (seconds))

Figure A-14: Temperatures - Salt-Cerrobend Hole Ablation Test 1129.

33

Embedded Thermocouple Response
Side 4 – 1129

Side 4
TCs 8,9,10,11
38mm Deep
9mm Separation

Temperature (C)

500.0
400.0
300.0
200.0
100.0
0.0

10.0   20.0   30.0   40.0

Time (seconds)

Test Section Temperature
1129

TC 16 – in Test Section
(melt temperature)

Temperature (C)

500.0
400.0
300.0
200.0
100.0
0.0

0.0   10.0   20.0   30.0   40.0

Time (seconds)

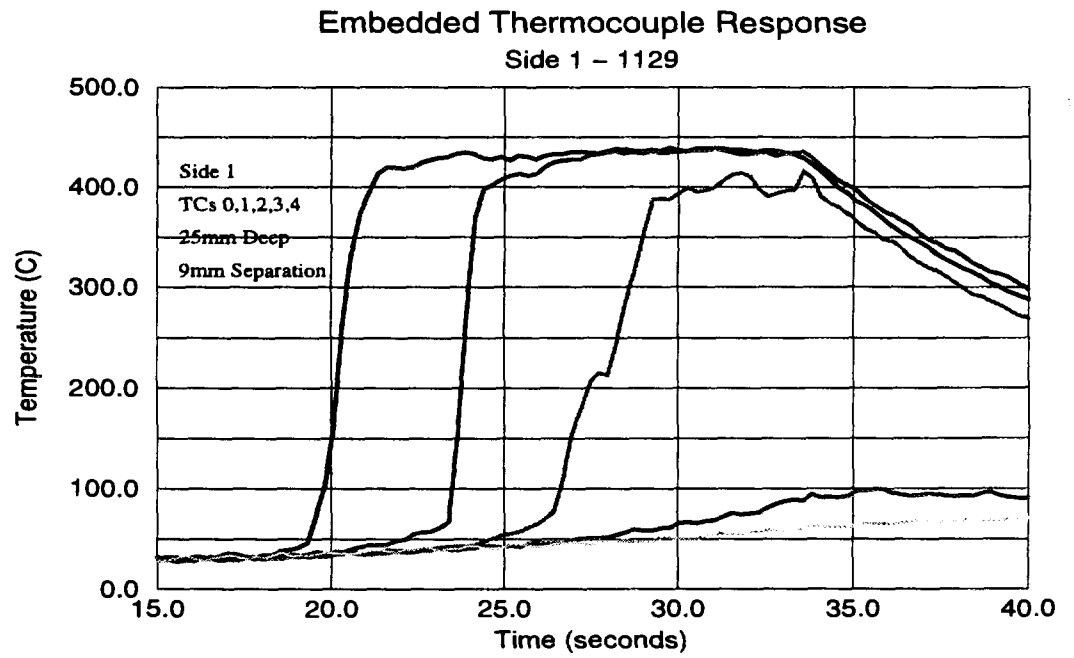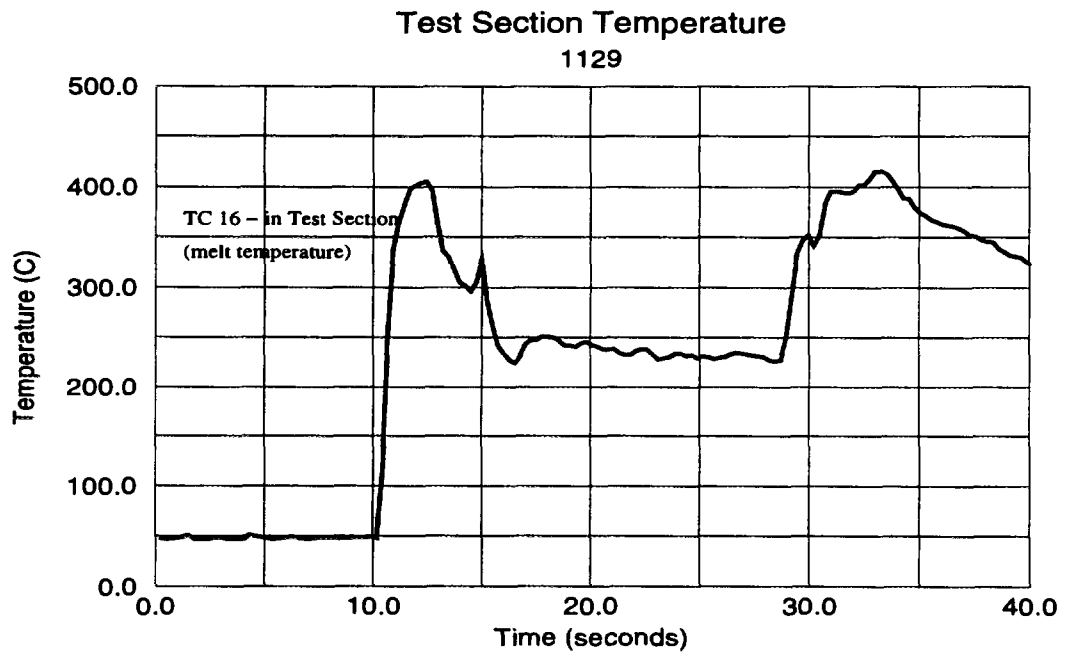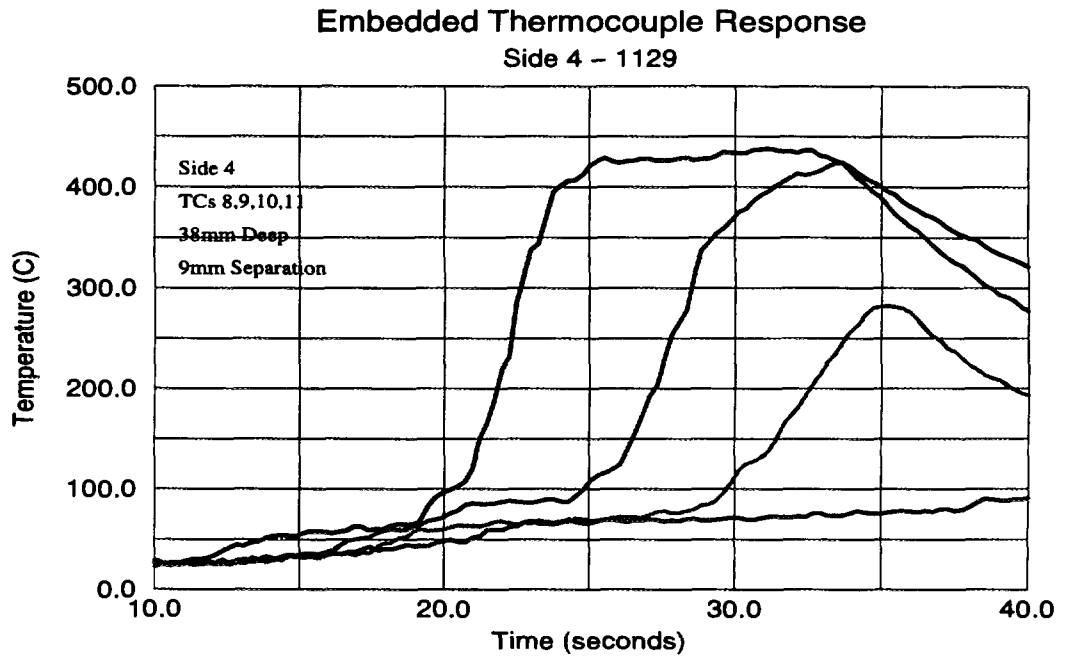Figure A-15: Temperatures - Salt-Cerrobend Hole Ablation Test 1129.

34

Embedded Thermocouple Response
Side 1 – 1211

Side 1
TCs 0,1,2,3,4
25mm Deep
9mm Separation

Temperature (C) vs Time (seconds)

Embedded Thermocouple Response
Side 3 – 1211

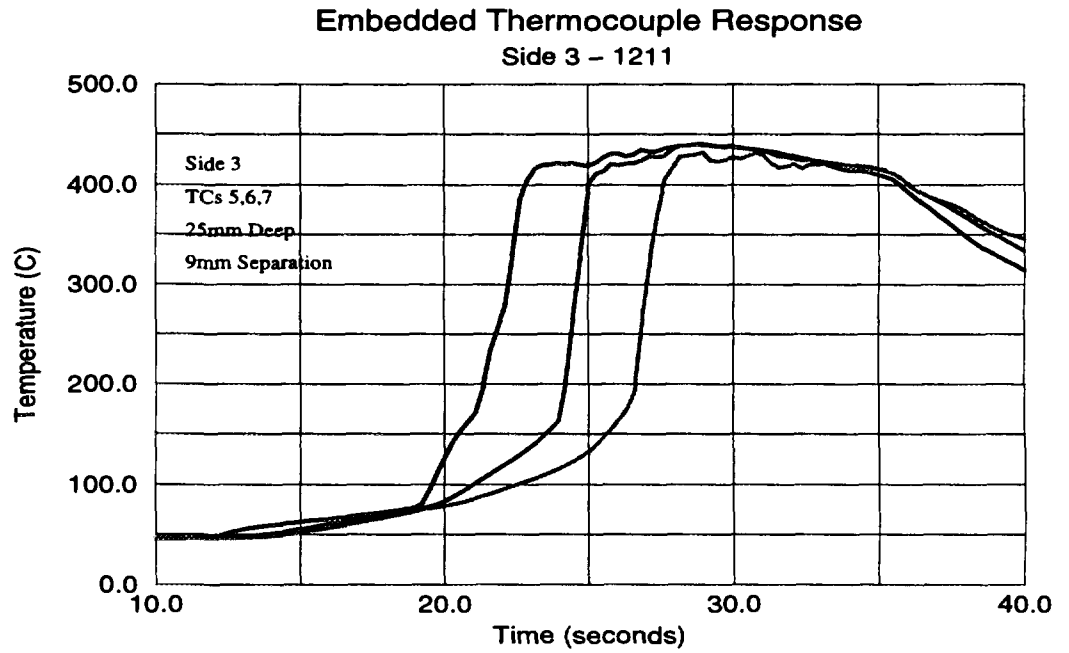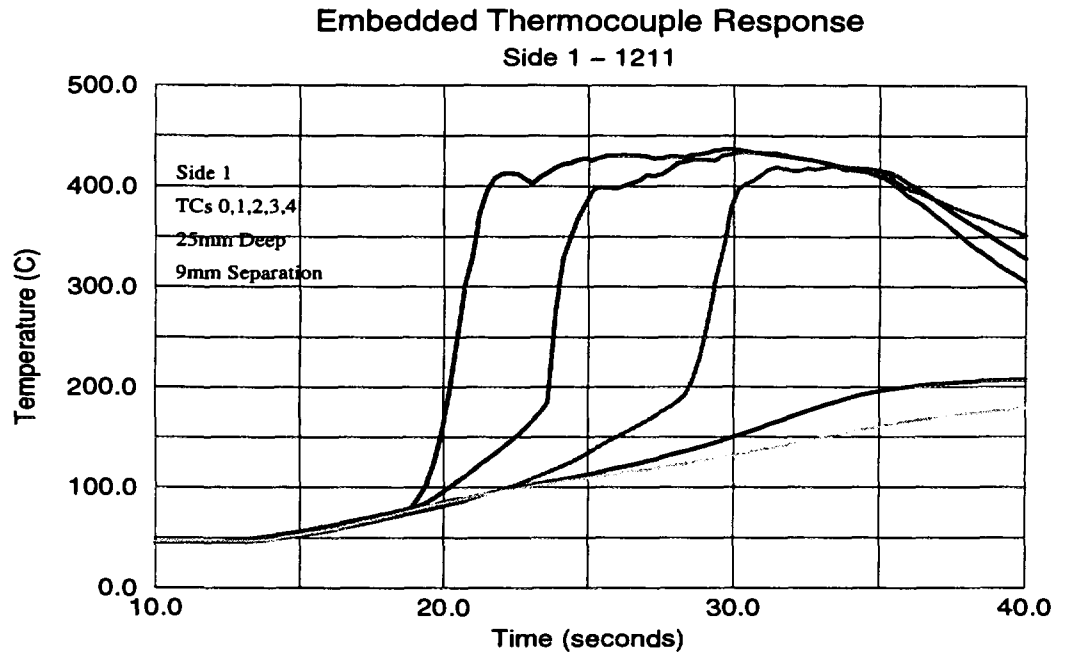Side 3
TCs 5,6,7
25mm Deep
9mm Separation

Temperature (C) vs Time (seconds)

Figure A-16: Temperatures - Salt-Tin Hole Ablation Test 1211.

Embedded Thermocouple Response
Side 4 - 1211

Side 4
TCs 8,9,10,11
38mm Deep
9mm Separation

Temperature (C)

Time (seconds)

Test Section Temperature
1211

TC 12 - in Test Section (melt temperature)

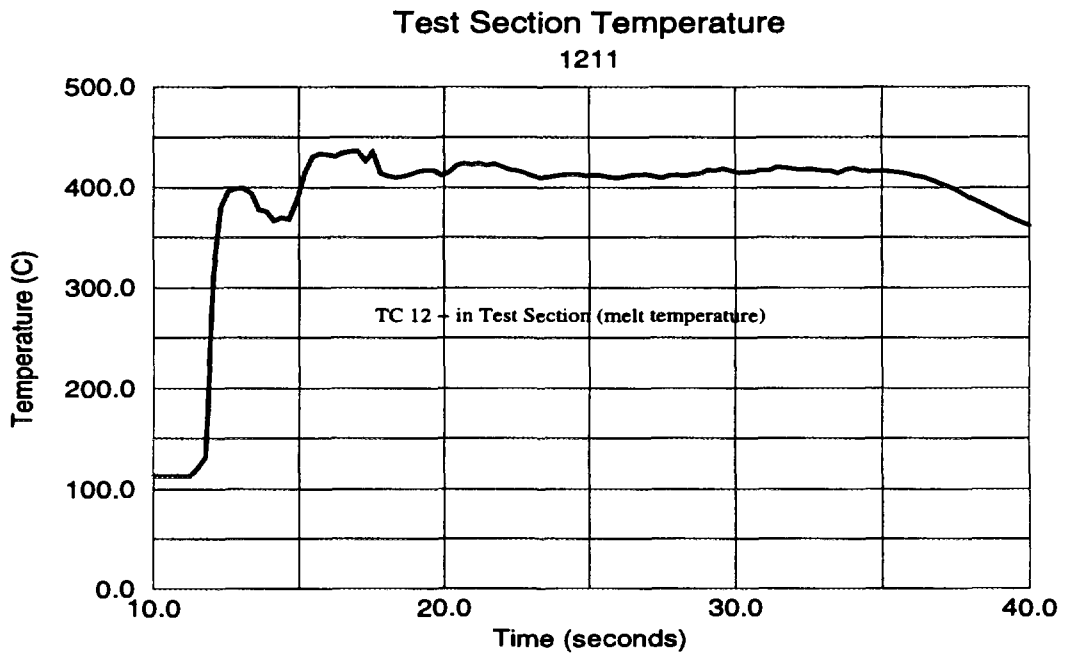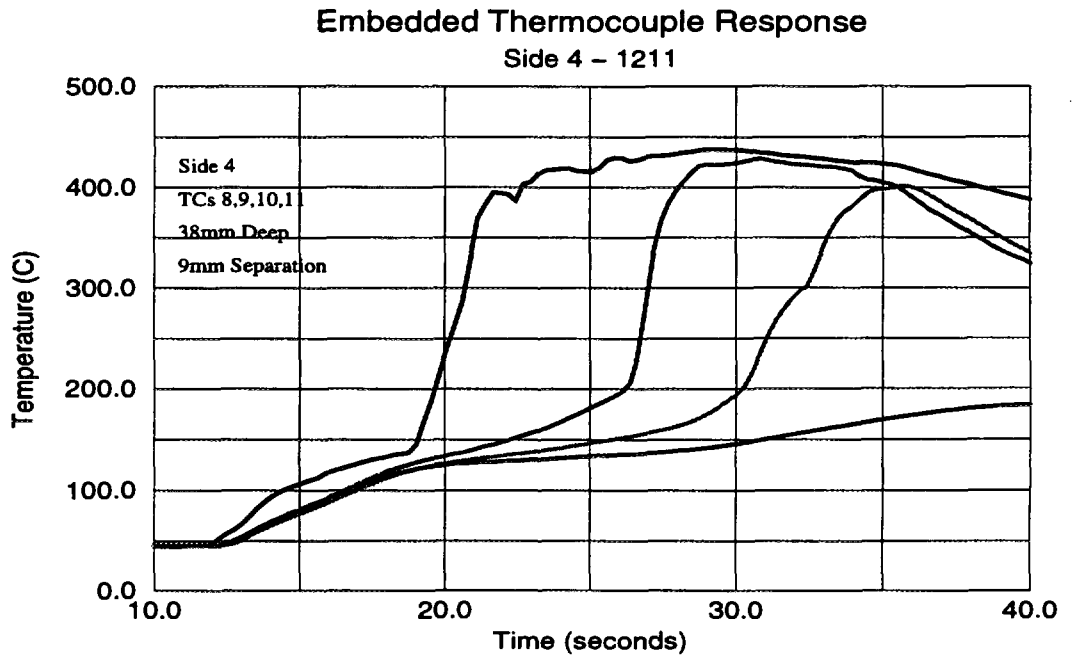Temperature (C)

Time (seconds)

. Figure A-17: Temperatures - Salt-Tin Hole Ablation Test 1211.

36

Appendix B: Description of a 20-liters Oxide Melt-Lead Plate Hole Ablation Experiment

Abstract

This section summarizes the results from a hole ablation experiment conducted on April 28, 1997 at the RIT/NPS laboratory. Approximately twenty (20) liters of 30-70 w/o CaO-B_2O_3 was inductively melted and poured into the pre-heated test section. The plate was 55mm thick Pb with 12 embedded thermocouples and an initial central hole of 15mm in diameter. This test showed a minimal ablation after pouring of the melt which was followed by a heatup of the Pb plate to its melting point which then resulted in an overall plate melting. Although there was not significant ablation evident, the results confirm the predictions of the pre-test HAMISA calculations.

B-1   Experimental Conditions and Melt Preparation

The following amounts of powders were mixed to make the melt:

20.7 kg CaO
74.3 kg H_3BO_3

If one assumes the typical loss of 35% of the boric acid mass due to the loss of water, then the resulting mass of B_2O_3 is 48.3 kg which yields a weight ratio of CaO to B_2O_3 30-70. The solidus and liquidus temperatures for this concentration are 980 and $1025°C$ respectively.

The test began at 9:30 am and the 18 liters was available after roughly 5 hrs at maximum power of the induction furnace. Note that 40kw was the maximum power possible for the coil configuration employed. However, that is acceptable since it corresponds to an outside crucible temperature of nearly $1250°C$. The crucible was made of Si-C and this particular crucible had been used twice before. It was noticed that some of the graphite from the crucible had entered into the melt and floated on the top of the melt as a slag. From post-test examination of the crucible, it does not appear to be significantly degraded and can be employed in another experiment. One of the major difficulties during the test is the exceptional amount of steam which is driven off and which typically overpowers the ventilation system. As in previous tests, the filters had to be removed in order to ensure enough suction. The ventilation system suffers from the difficulty that the fan decreases in speed now that the absolute filters have been removed. Satchwell is still working on this aspect.

There were 12 K-type thermocouples of 1mm OD embedded in the plate at varying depths and distances from the initial hole. The layout of the 12 TCs can be seen in Figure B-1.
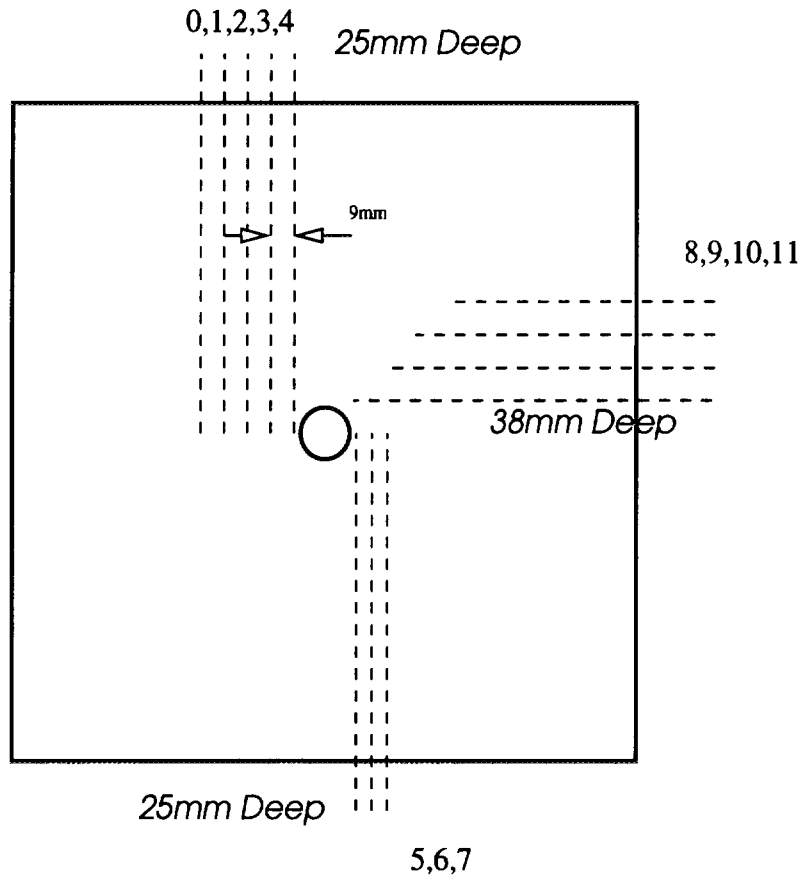

Figure B-1: Thermocouple Layout.

The melt was approximately 18 liters at 1350°C just before pouring from the furnace into the test section. The B-type thermocouple was used and for certain periods it worked properly. However, there is evidently a loose connection in this TC and measurements were highly dependent upon any slight movement of the thermocouple wire leads. The only use of this higher temperature thermocouple is for the measurement of temperatures in excess of 1200°C, since K-type TC's often fail at such temperatures.

The test section is 280mm ID and 500mm high. It was preheated to over 400°C by an arrangement of gas burners. Only a minimal crust layer was formed on the test section walls as realized by post-test examinations.

The melt of 18 liters would fill the test section to roughly 29 cm. An assumed C_d value of 1.0 would equate to a roughly 2.4 m/s discharge velocity without hole ablation.

B-2 Test Conduct

The melt was remotely tipped into the section and then the plate plug was pulled out. The tilting was accomplished quite quickly, estimated at less than 5 s, and the plug was removed immediately thereafter.
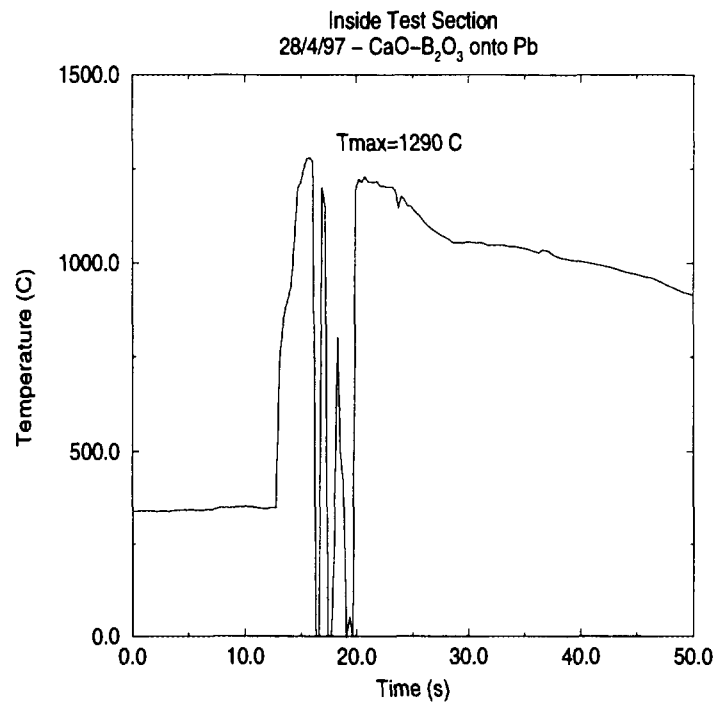

Figure B-2: Test Section Melt Temperature

The Hewlett-Packard Data Acquisition System (DAS) functions well. 400 scans of 15 channels were conducted with NPLC=0.01 and the time required was 109.2 seconds. (3.7 Hz). In addition, the mass discharged from the section was collected and recorded in time using the terminal application of the DAS PC (6.7 Hz).

The temperature of the thermocouple inside the test section wall is given in Figure B-2 while the readings from the embedded thermocouples are presented in Figures B-3 - B-5 and the mass collected from the discharge hole is shown in Figure B-6. The maximum temperature recorded in the section was $1290°C$ however the scanning was not done for a long enough period to capture the final rupture of the melt through the Pb plate. However, subsequent readings of these temperatures showed readings as high as $1300°C$ by some of the embedded thermocouples. At these temperatures the K-type TCs are not useful and typically give erratic readings (if not absolute failure). During the period of recording, the melt discharged as a relatively small jet and essentially little plate ablation was realized. By the time the DAS scanning had finished, the plate temperatures were

well above the melting point of 330°C and shortly thereafter the entire Pb plate simply discharged away and the remaining melt was discharged with it. This is seen at 125s of Figure B-6 where the mass collected increases rapidly.
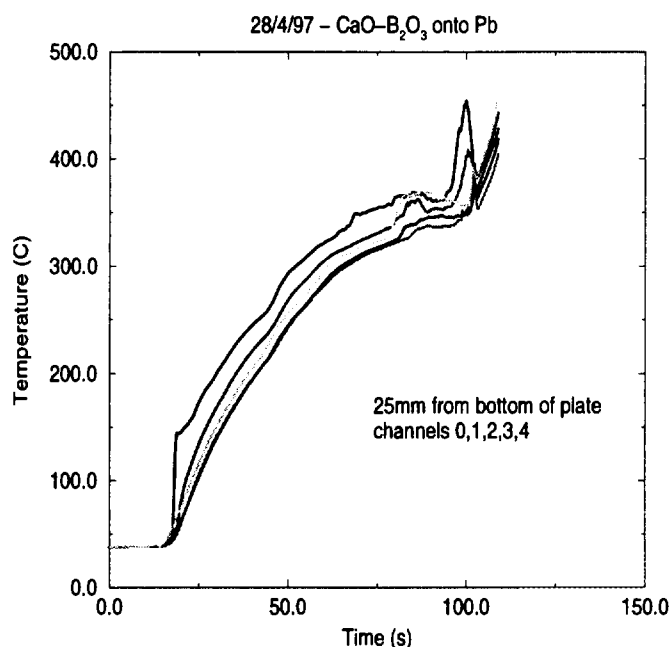

Figure B-3: Temperatures inside Pb Plate.

B-3   Analysis and Discussion

Since the final hole size is not available, the test results can only be analyzed in qualitative manner. The readings from the embedded thermocouples also do not reveal any useful information in term of hole enlargement dynamics, since the crust formation eventually plugged the melt discharge and thereafter the entire plate reached its melting point and discharged rapidly with the remainder of the melt in the test section.

However the test is useful for validation of the crust-formation model in the HAMISA code since the HAMISA pre-test calculation for these particular conditions showed that the crust would be developed to plug the initial hole. This is not the first time when the HAMISA crust formation model forecasts the choke-off the melt discharge flow in oxide-melt hole ablation experiments.

The reason for this plugging of the discharge flowpath is attributable directly to the kinematic viscosity of the melt simulant; $\mu = 0.1$ Pa-s and $\rho = 2400 kg/m^3$. This results
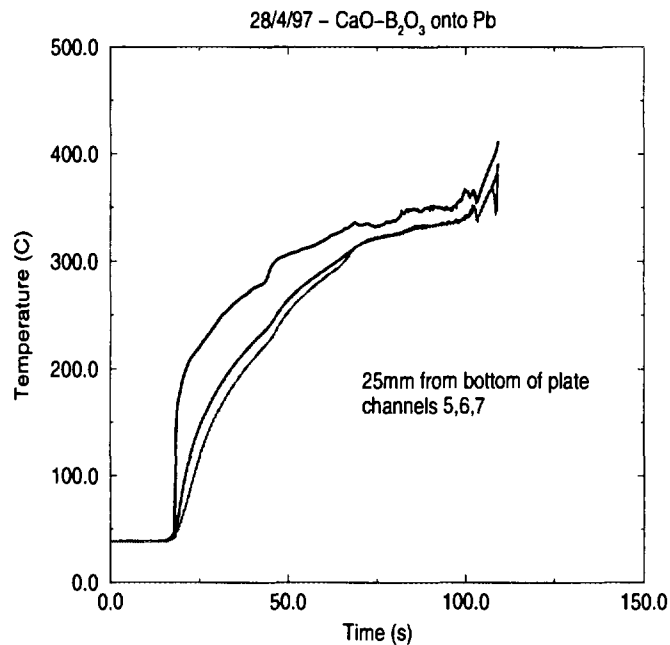
40

Figure B-4: Temperatures inside Pb Plate.

in laminar flow conditions and thus minimal heat transfer from the flowing melt to the ablating Pb plate. The crust which forms then grows and eventually prevents any further melt discharge. In this case however, the conductive heat transfer from the overlying pool of melt resulted in the majority of the Pb plate attaining temperatures greater than the melting point, which simply led to a massive failure of the plate. The current version of the HAMISA code does not predict the mechanical failure of the plate due to the attainment of liquid conditions.

Technically, the test demonstrated that:

(i) the B-type thermocouples can be used at the higher temperatures involved in these tests;

(ii) the Si-C crucibles are quite useful and result in only a slight contamination of the melt with C;

(iii) roughly 20 liters of the oxide melt can be generated repeatedly now in the MIRA facility at the RIT/NPS laboratory;

(iv) the HAMISA code properly predicted the choking-off of the melt discharge due to in-hole crust formation.
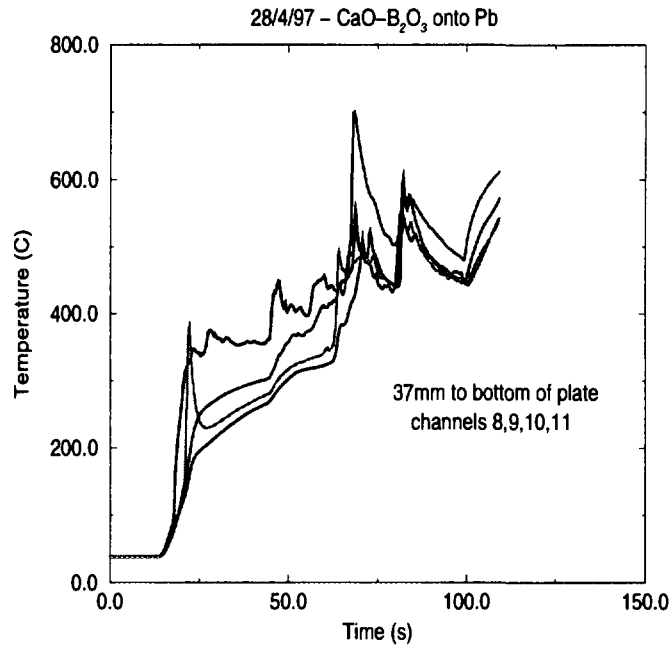
41

28/4/97 – CaO–B$_2$O$_3$ onto Pb

37mm to bottom of plate
channels 8,9,10,11

Figure B-5: Temperatures inside Pb Plate.
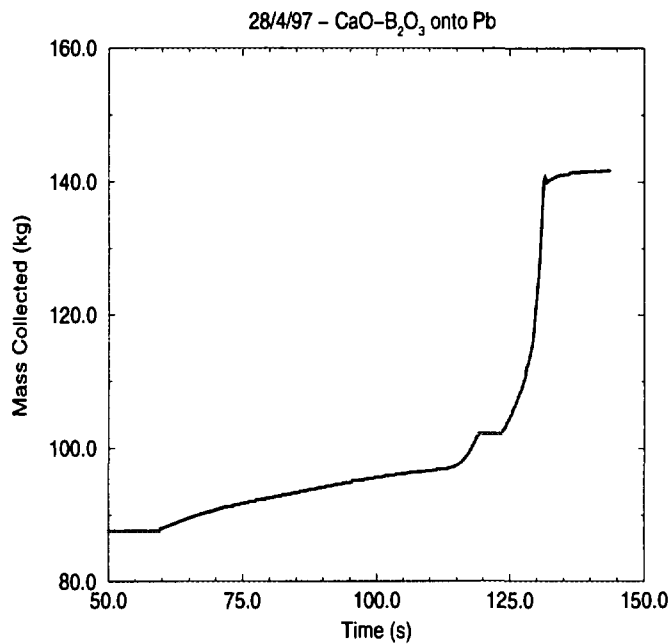

28/4/97 – CaO–B$_2$O$_3$ onto Pb

Figure B-6: Mass Discharged from Section.

42

B-4 Other Oxide-Melt Hole Ablation Experiments Performed at the Laboratory of RIT/NPS: Test Conditions and Major Observations

HOLE0124_96

- 35-65 w/o CaO-B_2O_3

- 4 liters melt made from unheated H_3BO_3

- Pb plate of 30 mm.

- 10mm diameter hole

- 1300°C melt just prior to pouring

- Manual pour

- Observation: Entire rupture of the plate due to prolonged pour-time.

HOLE0213_96

- 30-70 w/o CaO-B_2O_3

- 4 liters melt made from unheated H_3BO_3

- Pb plate of 30mm - 13 TC's

- 10mm diameter hole

- 1125°C melt prior to pouring

- 5mm thick (nonuniform) crust layer from 35-65 CaO-B_2O_3

- Approximately 10 seconds manual pour

- Observation: jet flow for less than 30 seconds, little (if any) melting of the Pb plate, majority of melt stayed in test section

HOLE0215_96

- Re-melt of the solid portions from HOLE0213_96

- 4 liters

- Pb plate of 30mm - 13 TC's

- 10mm diameter hole

- Over 1300°C melt temperature prior to pouring

- 5-7mm initial crust made from 35-65 $CaO\text{-}B_2O_3$ and placed above the Pb plate

- Manual pour in under 10 seconds

- Observation; crucible fire/shattering, cratering and pooling of Pb plate.

HOLE0404_96

- 30-70 w/o $CaO\text{-}B_2O_3$

- 40mm Pb plate 32 embedded TC's

- 10 mm diameter hole

- 4 liters melt volume

- Less than 10 seconds pour time

- 1150°C melt prior to pouring

- Observation: plug was not inserted far enough above plate and thus a crust layer prevented any flow to exit. Upper Pb melted but then re-solidified.

HOLE0409_96

- 30-70 w/o $CaO\text{-}B_2O_3$

- 40mm Pb plate 31 embedded TC's

- 10 mm diameter hole

- 4 liters melt volume made from pre-heated H_3BO_3

- 1160 °C melt prior to pouring

- 2 Hz data recording

- Approximately 10 seconds pour time

- Observations: successful test, *"good"* data although plug conductivity melted some Pb near hole at lower depths.

HOLE0415_96

- 30-70 w/o CaO-B$_2$O$_3$

- 4 liters melt made from preheated H$_3$BO$_3$

- 10 mm thick Al plate with 10 embedded TC's

- No preheating of plate - initial temperature is about 30 $^{\circ}$C

- Plug pulled in 5 seconds

- Melt temperature 1200 $^{\circ}$C prior to pouring

- Observations: No significant hole ablation. In-hole crust formation and plugging of the hole.

HOLE0416_96

- 30-70 w/o CaO-B$_2$O$_3$

- 10mm Aluminum plate - 11 embedded TC's

- 4 liters melt made from pre-heated H$_3$BO$_3$

- 10mm diameter hole

- 1200°C melt prior to pouring

- 5 seconds pour time

- Plate temperature prior to pour was 210°C

- Observation: no melting of Al plate at all, melt poured for over 2 minutes, final upper crust on Al was 13mm thick.

HOLE0418_96

- 30-70 w/o CaO-B$_2$O$_3$

- 40mm Pb Plate - 38 embedded TC's

- 4 liters melt made from solidified portions of HOLE0416_96 and 3kg of powder

- 10mm diameter hole

- 1160°C melt prior to pour

- Pb plate was 80° C prior to pouring

- 8 seconds pour time

- Observation: highly unsymmetric ablation/melt, very slight melt flow for over 20 seconds followed by a rapid melt-through. End-state is highly unsymmetric, no information for ablation dynamics.

HOLE0423_96

- 30-70 w/o $CaO-B_2O_3$

- 10mm Aluminum plate

- Variac was not turned off so TC readings were disturbed

- Observation: max plate temperature of 480°C, jet flow cut off after only a few seconds.

HOLE0426_96

- 30-70 w/o $CaO-B_2O_3$

- 20mm Aluminum plate - 16 embedded TC's

- 10mm diameter hole

- 4 liters melt volume

- Made from pre-heated H_3BO_3

- Al plate preheated to 370 ° C

- Observation: plug got stuck and could not be removed, no melt flow.

HOLE0522_96

- 30-70 w/o $CaO-B_2O_3$

- Pre-heated H_3BO_3

- 20mm Aluminum plate - 16 TC's

- Plate preheated to 580 °C

- 10mm diameter hole

- 4 liters melt

- 1200 °C melt prior to pouring

- 4 seconds pour time

- Observation: nice coherent jet for 45 seconds after which the crust prevented further melt flow, significant creep (bowing) of the Al plate, some very limited melting of the Al. Hole plugging was predicted in the HAMISA pre-test calculations.

Appendix C: Review of Low Temperature Hole Ablation Experiments

Abstract

A large number of hole ablation tests were conducted at RIT/NPS using water or paraffin oil as melt simulant and ice of salted water as vessel steel simulant. Employing large volumes (up to 80 liters) of low-viscosity and high-viscosity fluids, these tests provide good scaling to prototypical penetration failures. The test results were extensively used to validate the HAMISA model. This section presents original experimental results (temperature data) for some selected hole ablation tests.

C-1   Thermocouple Arrangement and Data Processing

Standard 1mm OD K-type thermocouples (TCs) are used with a typical accuracy of $\pm 0.7\%$. The data from the thermocouples is read using a high speed Hewlett Packard data acquisition system connected to a 486PC. Typical recording frequencies are 2 Hz or more for over 38 channels.

Thermocouples are arranged such that timing of the ablation front can be obtained (see Figure C-1).

The ablation front speed can be determined from the known distance of separation between individual thermocouples positioned on the same elevations.

$$V_{ablation} = \frac{R_{TC(i)} - R_{TC(i+1)}}{t_{TC(i)} - t_{TC(i+1}} \qquad (C-1)$$

The reference temperature difference is that between the melt jet and its corresponding melting point ($\Delta T_{ref} = T_j - T_{mp}$). Since the progression of the melt front is rapid, conduction in the plate material can be assumed to be small and the sensible heat of the plate is incorporated into the heat of fusion;

$$h_{fus}^* = h_{fus,p} + C_{p,p}(T_{mp,p} - T_\infty) \qquad (C-2)$$
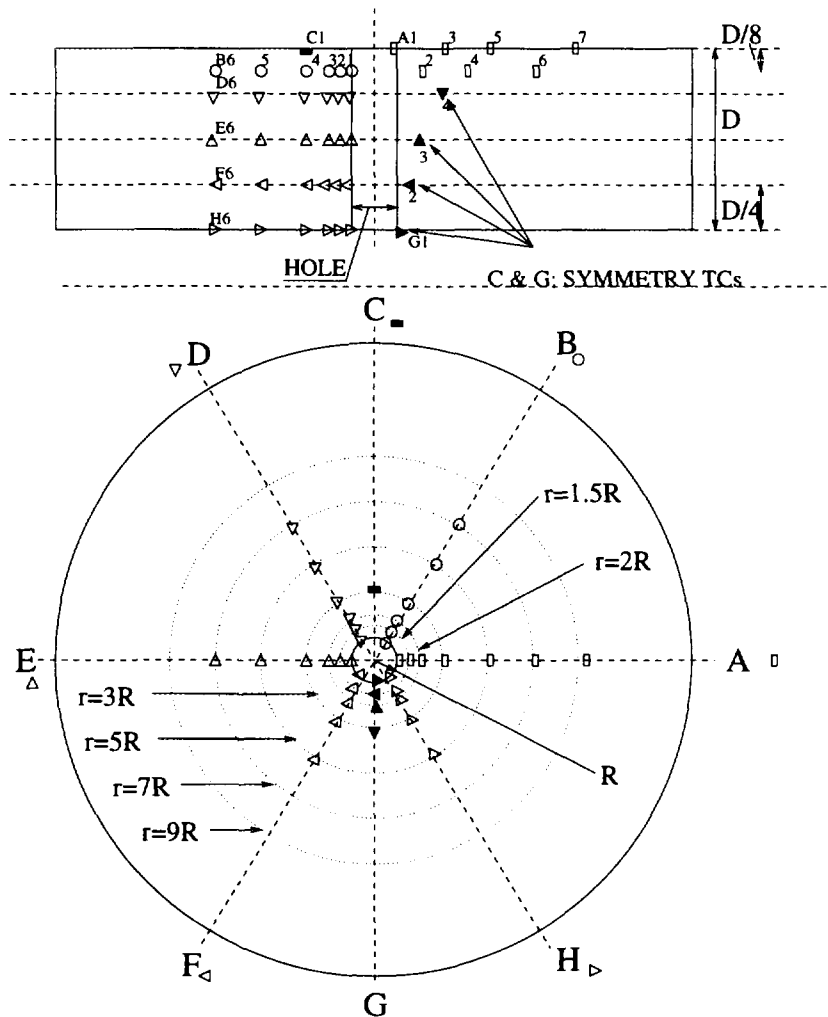
One can then determine the heat flux as;

48

Figure C-1: Thermocouple Arrangement for Hole Ablation Experiments

$$q_{abl} = V_{abl}\rho_p h^*_{fus,p} \qquad\qquad (C-3)$$

For these single-component tests, it was shown by Swedish [1], that the convective heat flux can be accounted for as;

$$q^*_{imp} = q_{abl}\frac{B}{ln(1+B)} \qquad\qquad (C-4)$$

where

$$B = \frac{C_{p,j}(T_m - T_{mp}))}{h^*_{fus,p}} \qquad (C-5)$$

Finally, the Nusselt number is determined as

$$Nu_o = \frac{q^*_{imp}}{\Delta T_{ref}} \frac{D_h}{\kappa_j} \qquad (C-6)$$

$$q_{cond} = \rho_p C_{p,p}(T_{mp,p} - T_{\infty,p})V_{abl} \qquad (C-7)$$

The data from the thermocouples is read using a high speed Hewlett Packard data acquisition system connected to a 486PC. Typical recording frequencies are 2...10 Hz for over 38 channels. Temperatures of the induction crucible, test section wall and test section melt are also recorded along with the time variation of the melt mass collected below the ablation hole.

C-2   Water-Ice Hole Ablation Tests

C-2.1   Test 0925

Figure C-2 shows temperature data of Test ICE0925. The test conditions are given in Section 2 of the present report.

C-2.2   Test 1015

Test was conducted October 15, 1996 on a 80mm plate of pure ice, with initial temperature of -24 °C. Initial hole diameter is 10mm. 78 liters of water at 44 °C was used as melt simulant.

10 temperature measurement channels were scanned, with 2 rows of 5 thermocouples at 2 depths: (i) #0-#4 TCs of first row at 45 mm from top surface, and (ii) #5-#9 TCs of second row at 60 mm from top surface (Figure C-3).

Final hole size was irregular, with 92-100mm at top surface and 93-96mm at bottom surface.

ICE0925 : Water onto SaltIce
Water=2 C : SaltIce=10w/o : Do=20mm
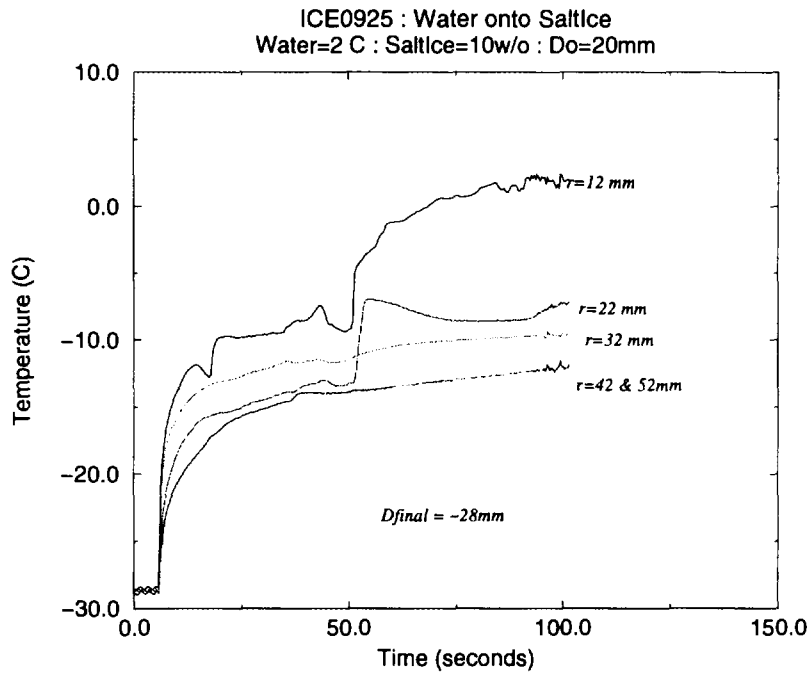
Figure C-2: Temperatures - Water-Salt-ice Hole Ablation Test 0925.

ICE1015 – Water onto Ice
Do=10mm, Tmelt=44 C, Plate=80mm

Figure C-3: Temperatures - Water-Ice Test 1015 (thermocouples #5-#9).
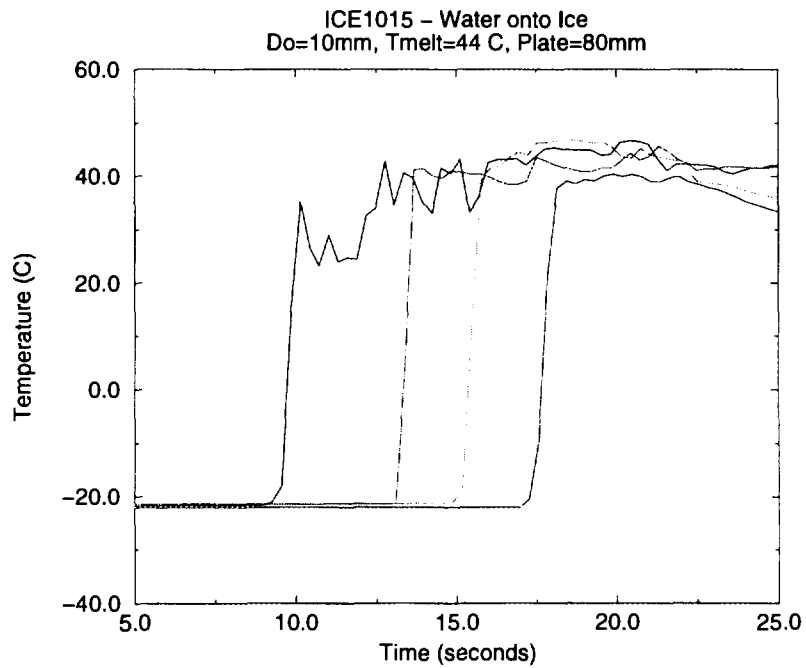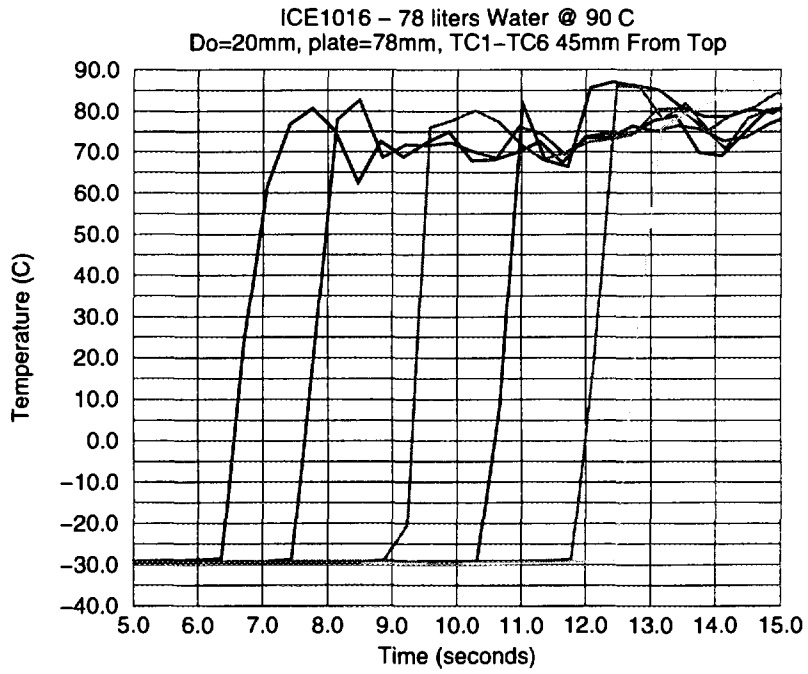
51

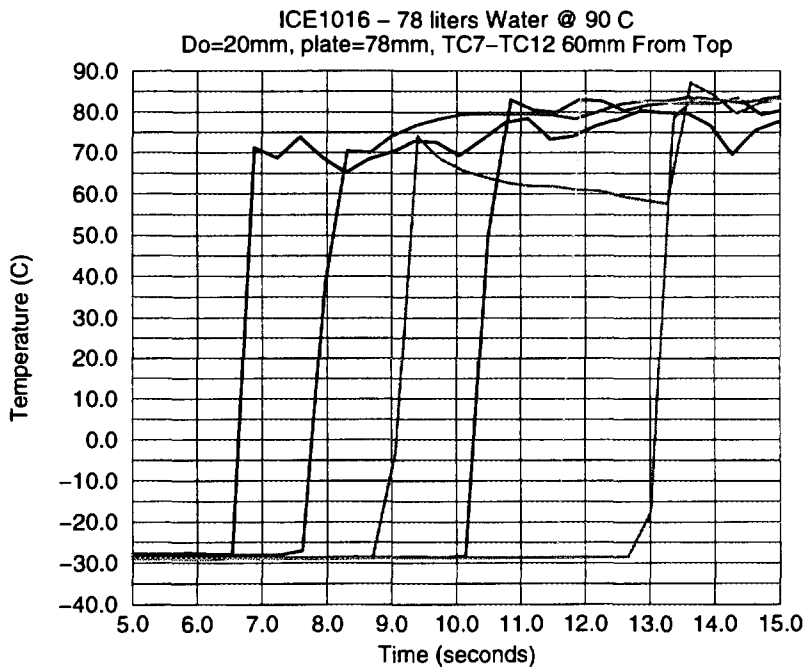Figure C-4: Temperatures - Water-Salt-ice Test 1016 (thermocouples #0-#5).

Figure C-5: Temperatures - Water-Salt-ice Test 1016 (thermocouples #6-#11).

C-2.3 Test 1016

Test was conducted October 16, 1996, using a 78mm thick plate of salt ice (10w/o NaCl). Initial diameter hole is 20mm and initial plate temperature is -30 °C. 78 liters of 90 °C water is used as melt simulant.

2 rows of embedded thermocouples. At 0° angle 6 thermocouples are installed 5mm apart at 45mm depth from the plate top surface (Figure C-4). At 180° angle other 6 thermocouples are installed 5mm apart at 60mm depth from the plate top surface (Figure C-5).

A scale build underneath of the test section is used to measure water discharge rate (Figure C-6).

Final hole sizes are 105/102 mm at top surface and 104/107 mm at bottom surface.

ICE1016 78 liters Water at 90.5 C
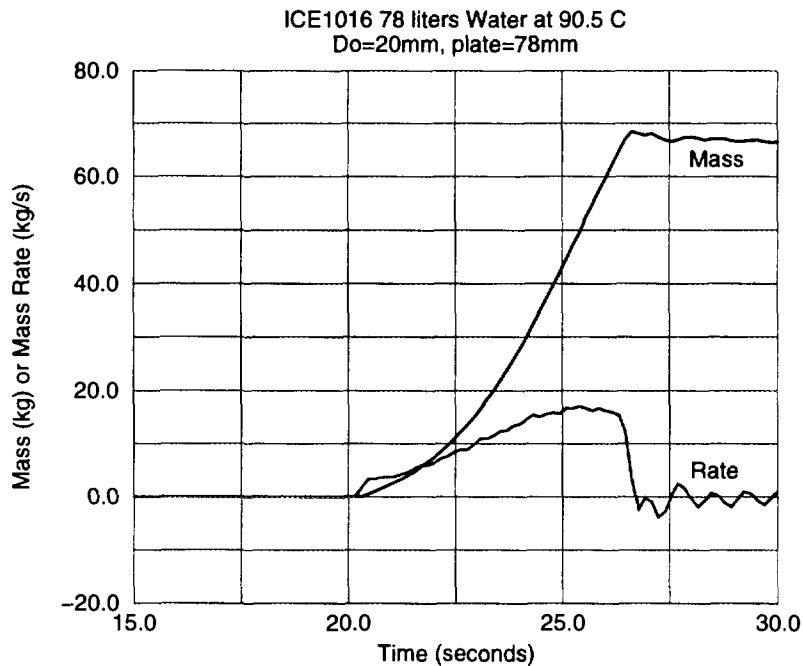Do=20mm, plate=78mm

Figure C-6: Mass Discharge Rate - Water-Salt-ice Hole Ablation Test 1016.

C-3   Paraffin-oil-Salt-ice Hole Ablation Tests

The test conditions of these tests (Test 1023 and Test 1024) were shown in the Section 2 of the present report. It was observed that, in both tests, little melting of the hole occurs.

In Test 1023, the hole ablation was not detected by the embedded thermocouples. Temperature data (Figure C-7), however, can be used to determine the heat fluxes, utilizing, e.g. an inverse heat conduction problem. In Test 1024, the final size was 30mm at top and 22 mm at bottom. In this case, thermocouples closest to hole indicated ice melting (Figure C-8).

In both tests, the top surface was found curved in but the hole is perfectly cylindrical through most the length. The observation agrees with calculations by the HAMISA code, when utilizing two-dimensional model of heat conduction in the ice plate and taking into account the in-hole friction due to high viscosity of the paraffin oil.
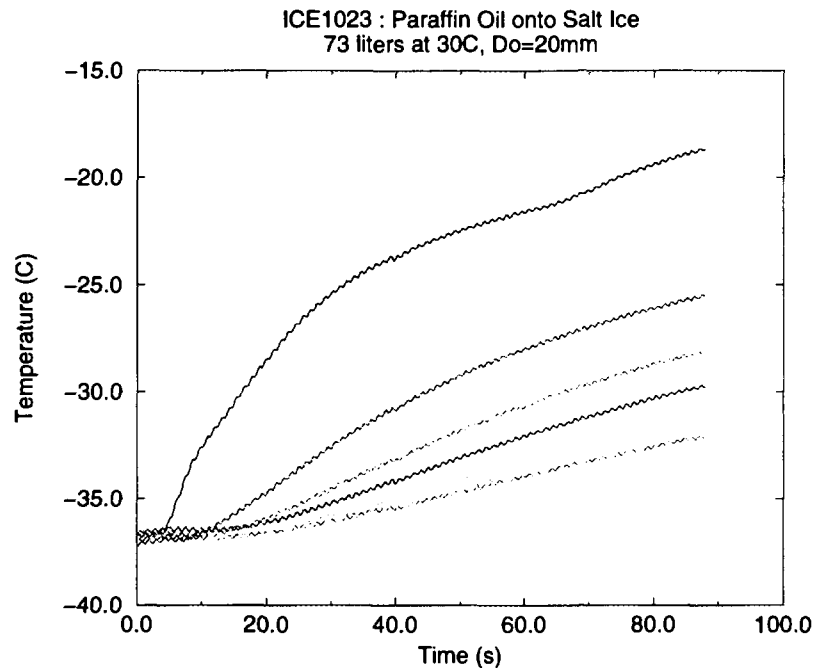
Figure C-7: Temperatures - Paraffin-oil-Salt-ice Hole Ablation Test 1023.

Nomenclature

Arabic

C_p	Heat capacity coefficient, J/(kg.K)
D_h	Diameter (of hole), m
h	Heat transfer coefficient, W/(m.K)
h_{fus}	Heat of fusion, J/kg
Nu	Nusselt number, $Nu = hD_j/\kappa$
q	Heat flux, W/m^2

54

ICE1024 : Paraffin Oil onto Salt Ice
45 C Melt, 72 liters, dX=60mm, Do=20mm
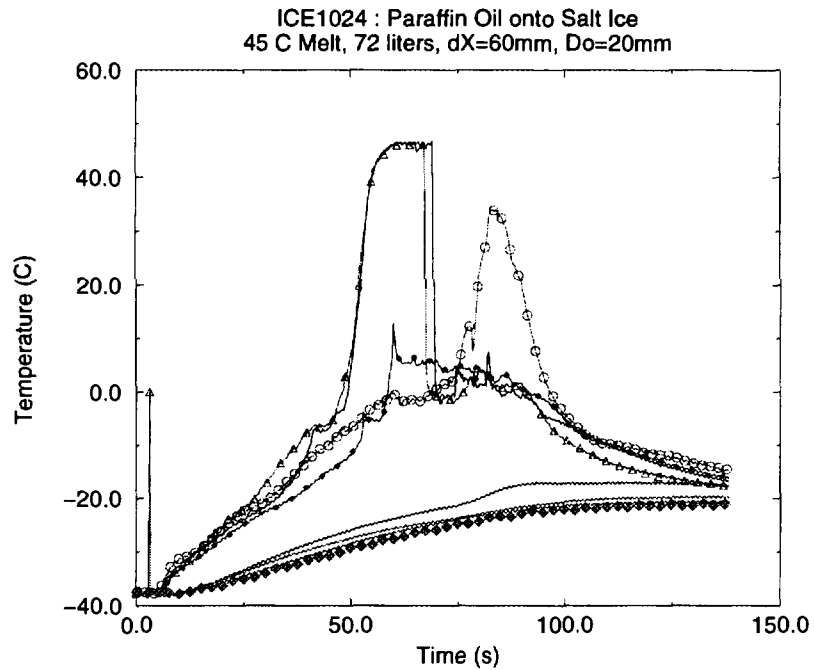
Figure C-8: Temperatures - Paraffin-oil-Salt-ice Hole Ablation Test 1024.

T	Temperature, K
V_{abl}	Ablation Velocity, m/s

Greek

κ	Heat conductivity, W/m·K
ρ	Density, kg/m^3
ΔT	Temperature difference, K

Subscripts

m	Melt (flow)
mp	Melting point
p	Plate
l	liquid
s	solid

References

[1] Swedish, M.J., et al., "Surface Ablation in the Impingement Region of a Liquid Jet, AIChE Journal, Vol.25 (4), (1979), pp. 630.

Appendix D: A Separate Effects Study of Discharge Coefficients for Use in Hole Ablation Experimentation and Modeling

Abstract

Experiments were conducted in the Division of Nuclear Power Safety (NPS) of the Royal Institute of Technology (RIT) to determine the discharge coefficients for flow exiting a geometry similar to that employed for vessel hole ablation experiments. The discharge coefficients obtained in these experiments cover a range of nozzle diameters and lengths. It was found that the commonly employed discharge coefficient of 0.6 is improper for typical reactor and experimental situations. The entrance, in-hole, and exit pressure losses for flow exiting the nozzle strongly influence the flow velocity which in turn plays an important role in the heat transfer and thus ablation of the plate structure when phase change is considered. Dependence of these coefficients upon fluid (melt) properties and geometry are discussed. A model is proposed for prediction of the overall nozzle discharge coefficient.

D-1 Introduction

Discharge coefficients, C_d, are used extensively in a variety of industrial engineering applications usually for the express purpose of determining the pressure loss-velocity relationship for fluid flow past an area change of known dimension. Values of C_d are empirically measured for particular geometries and flow conditions. These conditions are typically the ratio of upstream to orifice area, β, and the flow Reynolds number, respectively. For the case when fluid flows past an infinitely short orifice (sharp edged), the discharge coefficient has been shown to be 0.6 at high Reynolds numbers for most area ratios. The situation changes for the laminar and transition flow regimes in pipe flow, where the resulting C_d values for sharp orifii show considerable variation with Re [1]. However, for situations with longer lengths of the reduced area (L), such as nozzles, the discharge coefficient is seen to be dependent upon both the length-to-diameter ratio (L/D) as well as the Reynolds number of the discharging flow. Lichtarowicz [2] and Kiljanski [3] show pipeline discharge coefficients for a variety of L/D ratios and Re. Additionally, the work by Lichtarowicz provides a comprehensive overview of the experimental data obtained from a variety of other investigators.

Knowledge of C_d values is also necessary when examining the mass discharge from a vessel, under both atmospheric and pressurized conditions. In this respect, a sharp-edged orifice is unlikely to be employed and instead a finite L/D ratio (with L being typically

the vessel wall thickness) will be a characteristic of the discharging flow.

A very specific example, related to severe accidents in nuclear power plants, is the discharge of an in-vessel melt pool through a failure location in the lower reactor pressure vessel (RPV). For a given driving pressure difference between the in-vessel and ex-vessel atmosphere, a higher value of C_d will yield greater velocities, and thereby greater mass discharge rates.

$$U_{disc} = C_d \sqrt{2(P_{in-vessel} - P_{atmosphere})/\rho} \qquad (D-1)$$

In the case of gravity driven flow (for example the experimental case where $P_{in-vessel} \approx P_{atmosphere}$) then the melt velocity is driven simply by the height of fluid, h, over the overlying melt pool and discharge hole and the discharge coefficient, C_d, accounts for losses at the discharge point.

The rate of mass discharge from the pressure vessel to the containment atmosphere is a crucial parameter in determining the subsequent loadings placed on the containment during a severe accident. Unlike the case of orifii or nozzles in pipe flow, this involves the discharge of fluid into a different density medium, such as air or perhaps water. In the case of a nuclear reactor however, the situation is substantially complicated by the fact that the discharging flow is at a temperature higher than the melting point of the vessel melting point, and thus the discharge hole is increasing in diameter (ablating) in time. More detailed discussions of the hole ablation process can be found in the references by Dinh [4],[5] and Pilch [6].

The objective of the present study is to obtain experimental data for the discharge coefficient when fluid is ejected from the vessel through a nozzle of finite length into an air atmosphere. Application of these results to the situation of corium melt discharge from a RPV is then discussed.

D-2   Calculation Methods for C_d

Lichtarowicz et al. [2] examination of the substantial body of experimental work in the area of discharge coefficients including their dependence upon the geometry (L/D) and flow (Re) resulted in the following empirically-fitted correlation;

$$\frac{1}{C_d} = \frac{1}{C_{du}} + \frac{20}{Re}(1 + 2.25\frac{L}{D}) - \frac{0.005\frac{L}{D}}{1 + 7.5(log(0.00015 \cdot Re)^2)} \qquad (D-2)$$

where the *ultimate* discharge coefficient, C_{du} is that at fully turbulent flow conditions as determined by;

$$C_{du} = 0.827 - 0.0085\frac{L}{D} \qquad (D-3)$$

Although this empirical approach provides good indication of C_d values for a range of L/D and Re, it is nonetheless based upon conditions of pipe flow where both the upstream and downstream fluids are the same.

A model with more physical underpinnings is proposed by the present authors here for the case of short nozzles with discharge into air. The velocity of the discharged flow can be determined from

$$U_d = C_d\sqrt{\frac{\Delta P}{\rho}} = \frac{1}{\sqrt{\sum F\rho}}(\sqrt{2(P_{vessel} - P_{atmosphere} + \rho g H)}) \qquad (D-4)$$

where F represents the sum of the entrance, in-hole and exit form losses as the fluid passes the nozzle/orifice. Expansion of the form losses in these terms provides;

$$C_d = \frac{1}{\sqrt{F_c + F_{in-hole} + F_{ex}}} \qquad (D-5)$$

The value of $F_{in-hole}$ is obtained from the frictional losses for common pipe flow and a variety of correlations exist for the laminar, transition and turbulent flow regimes. The term can of course be included or excluded with ease depending upon the situation at hand and indeed, for consideration of melt flow and discharge through over a rather long length, as envisioned for bottom penetrations of the RPV, inclusion of this term is necessary. Likewise, at low Re values the in-hole frictional term increases which in turn decreases the value of C_d.

The contraction form loss coefficient for a sharp contraction falls between 0.44 and 0.5 [7] whereas the expansion form loss coefficient varies depending upon the length of the orifice/nozzle. For extremely short nozzles, a value of F_{ex} of 2.25 allows for agreement with the classical orifice discharge coefficient of 0.6 for fully turbulent flows regardless of the mediums. Agreement with the data of Lichtarowicz implies a value of F_{ex} of 1.0.

D-3 Experimental Study

In order to better quantify the values of C_d for short nozzles with expansion into a lower density fluid, a simple tank apparatus was arranged. This involved a rectangular glass tank of dimension 0.3 x 0.3 m with a 1.0 m height, thus providing for a maximum discharge volume of 90 liters. At the bottom of the tank, plastic plates of various thicknesses with centrally located holes of known diameter formed the container boundary. The ratio of hole-to-tank diameter is kept small to prevent any non-uniformity in the approach to the hole. Straight bore holes were made in the plastic with high precision.
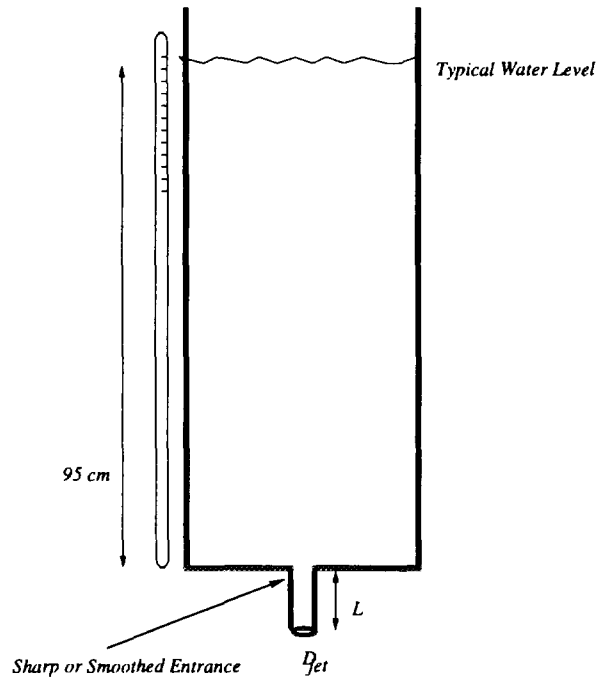
Figure D-1: Experimental Arrangement

Water over a range of temperatures ($3 < Pr < 12$) was employed in the majority of testing but in some cases higher viscosity (μ=35cSt) paraffin oil was used. The level of the tank was measured in time along with the mass discharge in time via an electronic scale. In this manner the experimentally determined discharge coefficient could be obtained as;

$$C_d = \frac{U_{meas}}{\sqrt{2 \cdot g \cdot H}} \qquad (D-6)$$

where H is the tank level and U_{meas} is determined from the derivative of the collected mass in time. The only pressure driving force is that due to the gravity head since the test section is open to the atmosphere. It must be emphasized that the discharge coefficients determined in this fashion are transient in nature since the driving force decreases in time.

Under these circumstances however, the deceleration of the fluid is negligibly small [8]. Also, data obtained when the tank was nearly drained was excluded since it is substantially influenced by the swirling gas vortex which is formed [9].

Table D-1 lists all the hydraulic water tests and their corresponding geometry and flow conditions.

Table D-1: Hydraulic Tests - Water

Tests #	D_{jet} (mm)	L (mm)	Avg. T °C	Range T °C	L/D_{jet} (-)	Pr (m²/s)	Re (-)	C_d (-)
4	15	400	19.9	16.5-22.8	26.7	7.03	38,000-57,800	0.76-0.81
4	15	62	16	~16	4.13	7.85	25,600-51,500	0.88-1.06
3	15	43	16.4	16-17	2.87	7.85	25,300-53,500	0.91-1.10
3	15	32.5	15.5	15-16	2.17	7.85	24,200-51,200	0.89-1.12
2	15	32.5	51.9	51-52	2.17	3.43	51,100-99,400	0.94-1.13
1	15	32.5	3	3	2.17	12.0	16,900-33,300	0.89-1.13
1	15	32.5	11.7	11.7	2.17	8.94	22,400-48,300	0.93-1.14
2	15	32.5	65.3	63-67	2.17	2.74	61,000-133,900	0.92-1.17
3	15	16	20.8	18-23	1.07	7.0	25,700-71,900	0.93-1.13
1	15	16	48.5	48.5	1.07	3.66	45,500-109,600	0.94-1.14
5	25	50	42.6	38-45	2.0	4.10	72,200-162,100	0.91-1.07
4	25	50	16.8	15-18	2.0	7.85	41,100-87,900	0.88-1.04
2	25	50	68.6	67-70	2.0	2.61	107,700-254,900	0.91-1.06
4	25	30	16.6	15-18	1.2	7.85	39,400-84,500	0.89-1.07
5	25	16	15.3	14-15	0.64	7.85	29,600-63,800	0.67-0.87
3	25	8	21.1	18-23	0.32	7.0	38,600-68,700	0.69-0.72
3	25	4	20.0	19-21	0.16	7.0	33,800-70,400	0.69-0.72
2	25	2	16.2	16-20	0.08	7.85	34,000-70,800	0.69-0.72

The experimental velocity, U_{exp}, was determined simply from the volumetric discharge rate divided by the tube area. The actual head of water for use in determining the discharge coefficients is that of the water in the measured section plus the length of the tube.

Typical results for the experimental velocity as a function of the water head are shown in Figure D-2 for different tube lengths and diameters ambient temperatures. One can see from Figure D-2 that both the 15 and 25 mm diameter tubes at ≈30mm length yield similar velocity discharge curves. However, when the same 25mm diameter tube is reduced by roughly 1/2 in length (16mm) that the discharge velocity as a function of water level is significantly reduced. For comparison, a very long tube (400mm), was examined since this

provides a situation where the in-hole friction pressure loss is substantial in comparison to the entrance/exit effects.

Hydraulic Tests
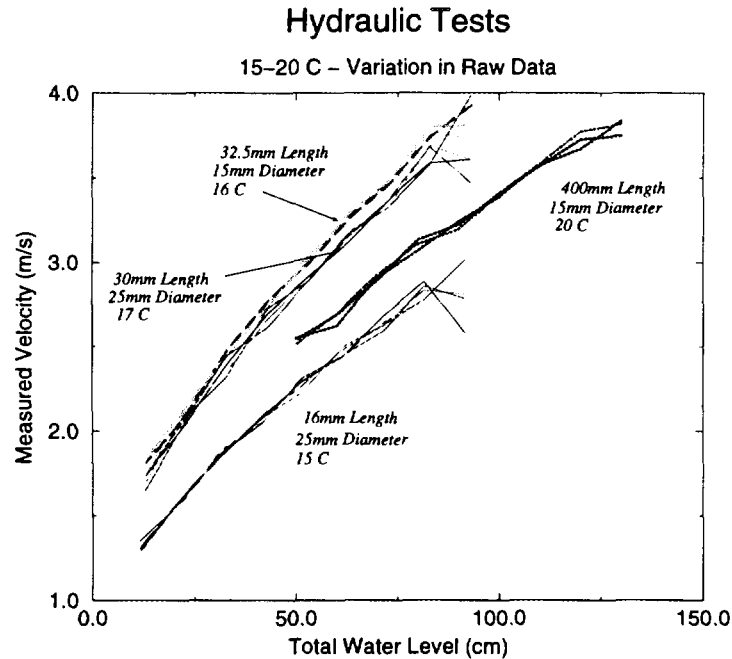
15–20 C – Variation in Raw Data

Figure D-2: Discharge Velocity as a Function of Gravity Head

From known thermo-physical parameters at the water temperature the Reynolds number can be determined. An indication of the uncertainty in the data is given in Figure D-3 which shows the results of 4 individual tests for a given flow diameter of 15mm and tube length of 32.5mm. Water temperature is kept nearly constant for the four runs shown. The greatest variance is found to always occur at the highest water levels due to the rapid rate of fluid discharge at that point in time. Figure D-4 shows data for the same geometry tube but over a range of temperatures. The figure shows that variation in temperature, from 3 to 67 °C, and thereby a substantial change in viscosity and thus Pr (2 to 10), plays little role in the discharge velocity from the tube. The implication being that viscous shear forces are *not* a dominant feature of this process.

The experimentally determined discharge coefficients have been plotted against water height and measured velocity for all of the data (except the first test which employed a 400mm long tube) in Figures D-5 and D-6, respectively. The data for L/D greater than 1 covers diameters of 15 and 25mm and a range of tube lengths and fluid temperatures. Yet, all the data is seen to be closely clustered. The data for L/D below ≈ 1 is for a 25mm diameter tube at ambient fluid temperatures. All of the data plotted in these figures are *averaged* values for similar conditions. Each test set shows a characteristic rise in discharge coefficient at low water height (which is equivalent to low discharge velocity). This agrees with data found in Perry [1] which shows C_d as a function of Re and the ratio

61

of upstream to constriction area, β.

Hydraulic Tests – D_jet=25mm, L=50mm

Uncertainty in Data
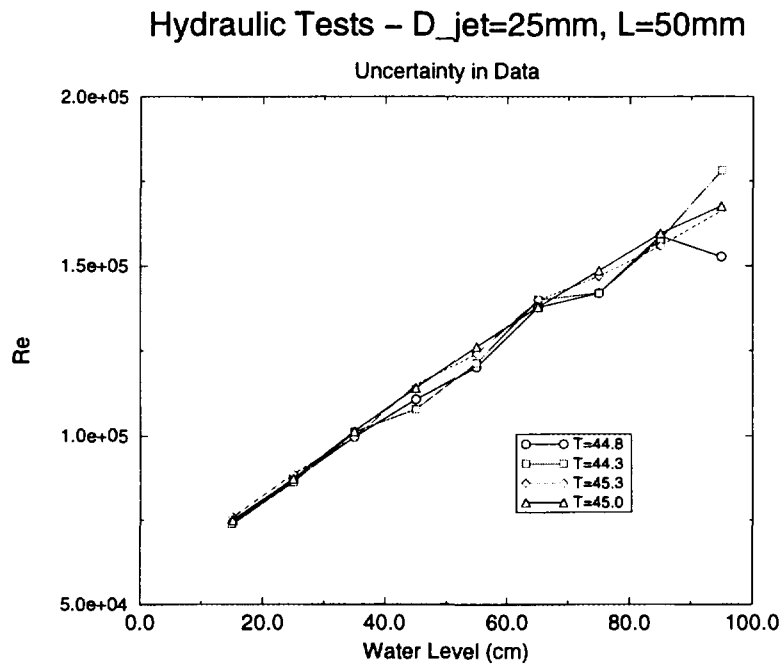
Figure D-3: Variability in Test Data

Hydraulic Tests

D_jet=15mm, L_tube=32.5mm
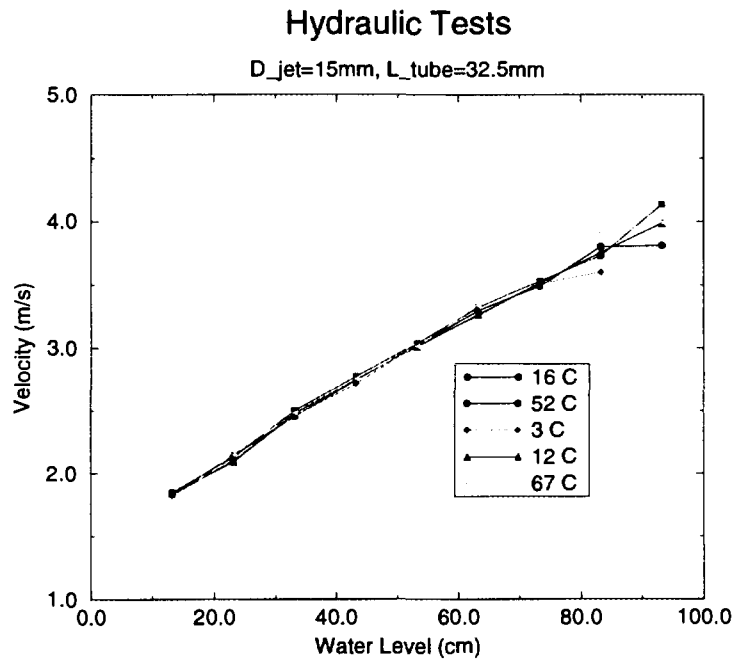
Figure D-4: Impact of Temperature Variation upon Discharge Velocity

Hydraulic Tests

All "Averaged" Data
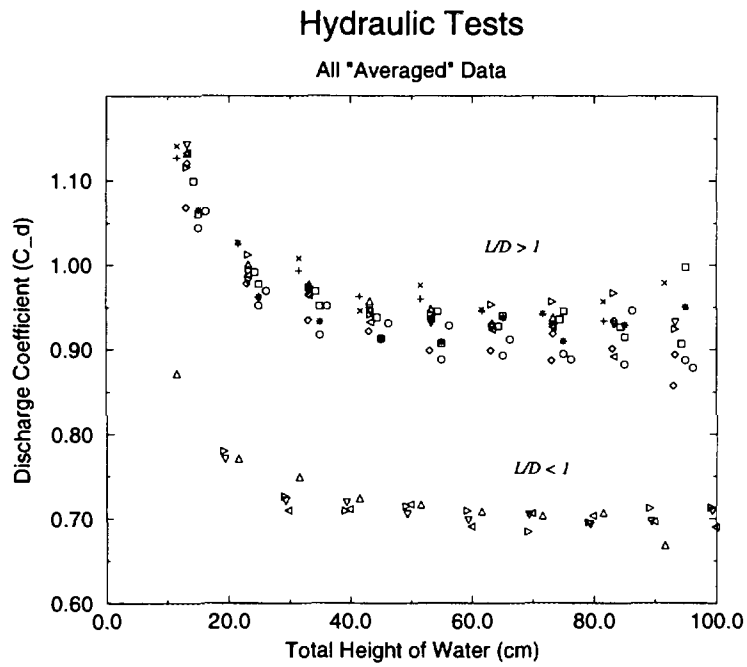
Figure D-5: Discharge Coefficient as a Function of Gravity Head and Geometry

Hydraulic Tests

All "Averaged" Data
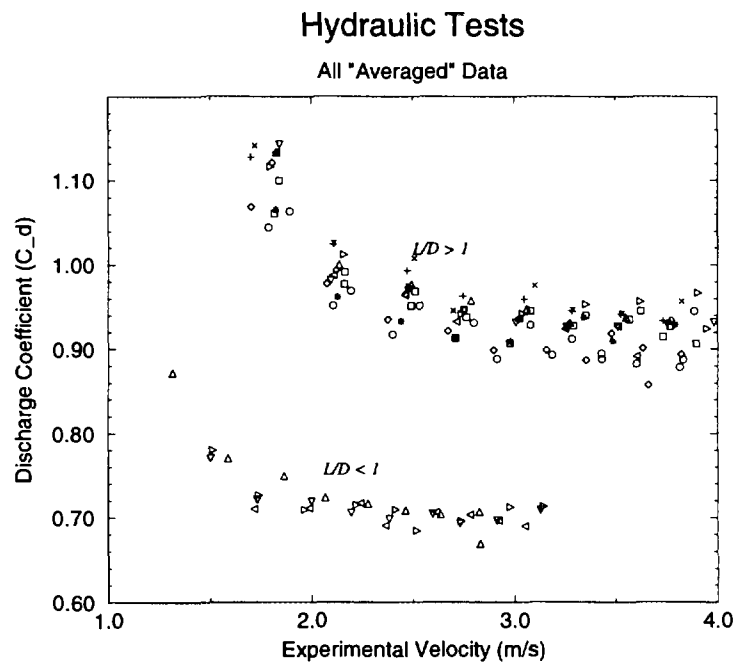
Figure D-6: Discharge Coefficient as a Function of Velocity and Geometry

Hydraulic Tests

Effect of Temperature
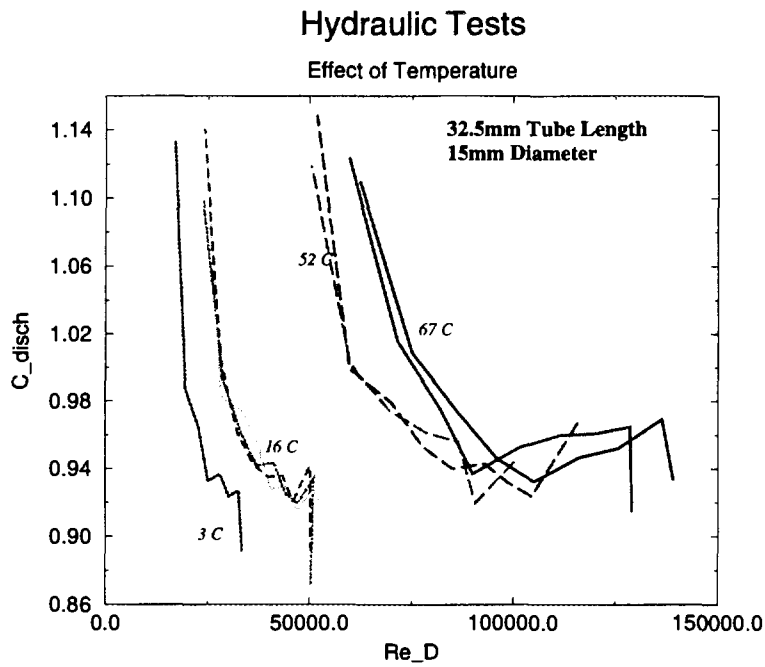
Figure D-7: Discharge Coefficient as a Function of Re

Hydraulic Tests

Effect of Temperature

Figure D-8: Discharge Coefficient as a Function of Re

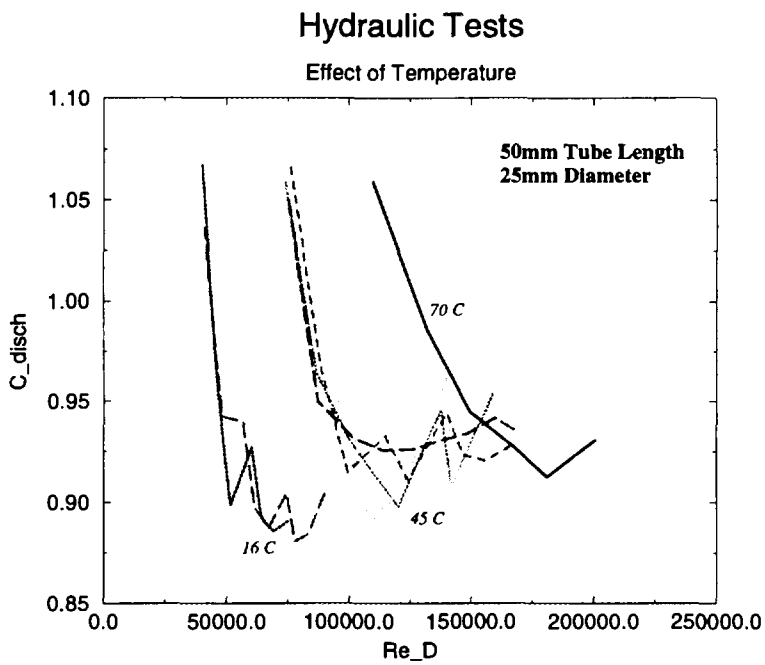For Re number above $\sim$30,000 the values of C_d are essentially constant between 0.595 and 0.620 regardless of β. At lower Re number, the value of C_d is found to increase with increasing Re. However, care must be taken in employing data obtained from orifii in pipe flow to the case of interest here [1].
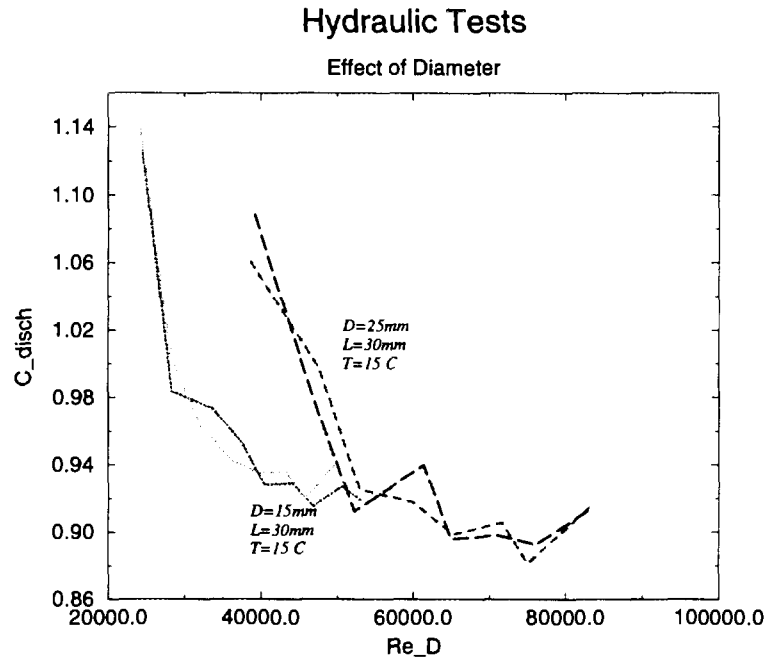
Hydraulic Tests

Effect of Diameter

Figure D-9: Effect of Diameter Change upon C_d

Temperature effects are manifested in the calculated Re number primarily as a result of viscosity changes. This is clearly seen in Figures D-7 and D-8 for L/D ratios of approximately 2 for the 15 and 25mm diameter tubes. Recall, there is little if any discernable difference in measured velocity as a function of the water temperature (Figure D-4). Thus in Figures D-7 and D-8, the shift in the curves is simply a result of the variation in the kinematic viscosity as a function of temperature. The experimental C_d is seen to increase with decreasing Re which of course is the result of the decrease in velocity as the tank empties. In addition, one should note the y-axis, and realize that the change is not significantly large.

The effect of diameter change is given in Figure D-9 where the fluid temperature and tube length have been maintained the same.

---

[1]There are two fundamental differences:
(i) The fluid (water in this case but corium in the reactor case) is being discharge into a different (much lower density) fluid. Orifice related C_d are for pipe flow with the system 'full' of the same type fluid.
(ii) Flow orifii are very thin (along the flow path) and thus there is little to no length in which the flow can develop. For application to hole ablation, the length for flow is much longer (even 150mm in reactor cases.

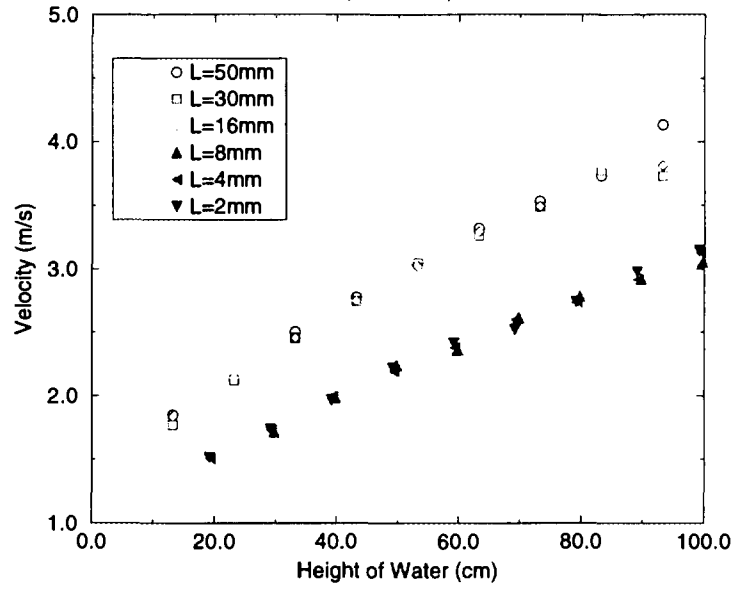## Hydraulic Tests – 25mm D_jet

(~16–20 C)

Figure D-10: Effect of L/D Ratio on Discharge Velocity

Hydraulic Tests – D_jet=15mm
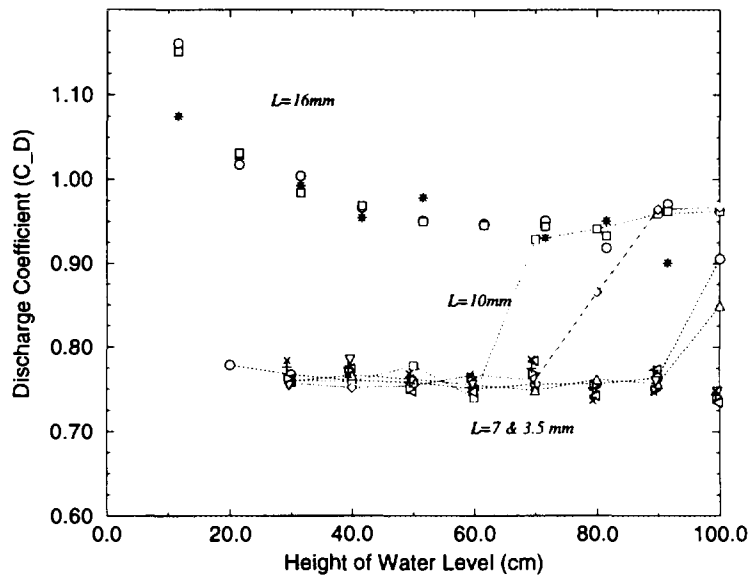
T_water ~ 20 C

Figure D-11: Transition Point

As was seen previously, the shorter L/D ratios (below $\sim$ 1) result in substantially lower velocity discharge rates and thus experimentally determined discharge coefficients (see Figures D-4 & D-5). Such results are more clearly seen in Figure D-10 where the velocity-water level data are plotted for a given diameter tube of varying lengths at roughly the same temperature. Such data reflects a *step* behavior relationship upon the L/D ratio rather than a functional relationship. That is to say, after reaching a *critical* value of L/D, somewhere less than 1.0, that the measured discharge coefficient becomes significantly reduced.

Clearly there exists a *transition point* which depends strongly upon the geometric L/D ratio. However, the transition does not appear to be solely due to the geometry but rather a combination of the geometry and gravity head (driving force). This is evident from tests conducted with a 15mm flow diameter at varying lengths the results of which are shown in Figure D-11. At a length of 16mm ($L/D = 1.07$) the discharge coefficients fell into the 0.9 to 1.1 range. Shortening of the tube length to 10mm revealed a transition from the higher values of discharge coefficient (in reality discharge velocity) *during* the discharge process. That is to say, the rate of fluid discharge from the nozzle dropped (or transitioned) as the gravity head fell. The complication with this particular L/D value was the fact that this transition was not reproduceable (even though water temperature was held very nearly constant). Thus in some instances the transition to lower discharge velocities occurred quite early, in others the tank level was seen to decrease by over 40cm before the transition was observed. Furthermore, the transition was not only realized from the data calculation, but rather it could be clearly noted from visual and audio observation during the tests. When the nozzle length was reduced to 7 and subsequently 3.5 mm (L/D of 0.47 and 0.23 respectively) the lower discharge velocities (C_d) were always realized.

In general, it was found that the method proposed in section D-2, Eq.(D-5), can adequately describe the experimental results obtained (e.g. Figures D-12-D-13).
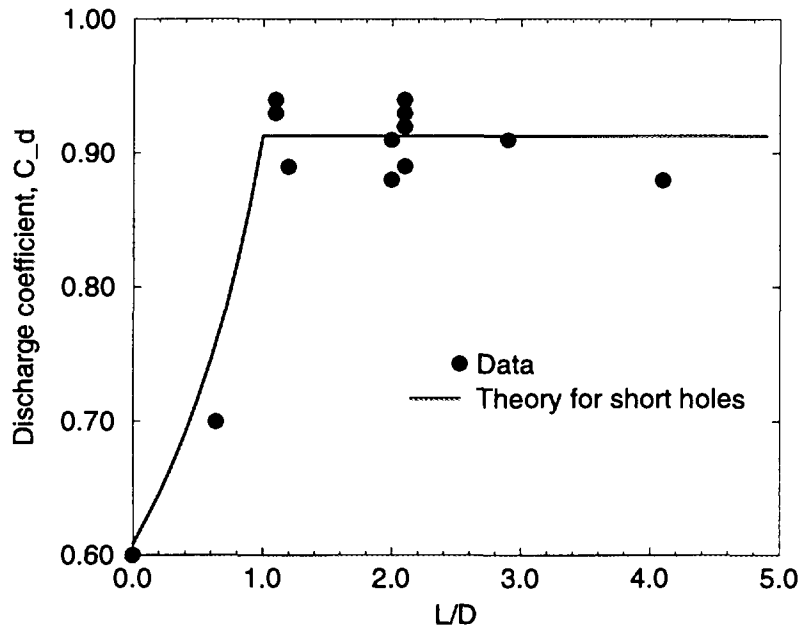
Figure D-12: Comparison and prediction for different hole lengths and Re numbers.
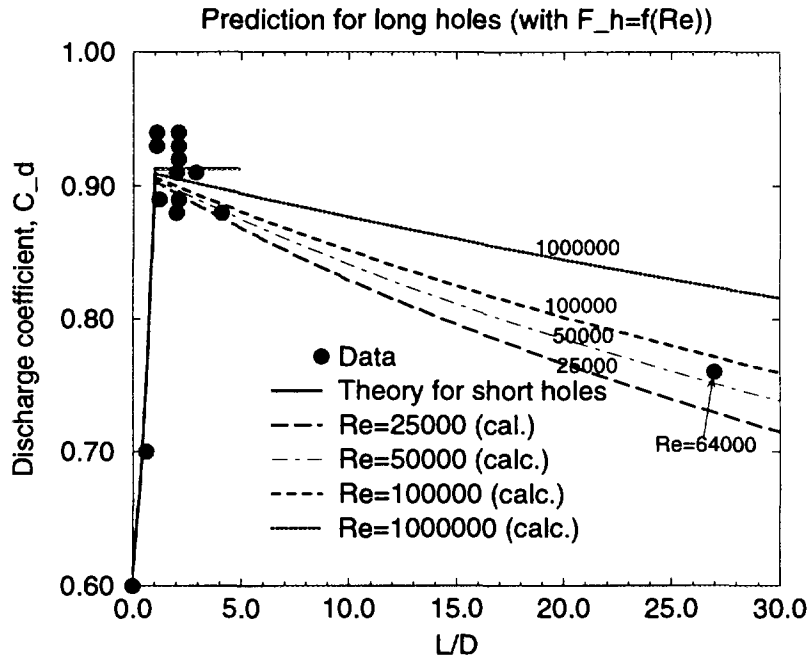
Figure D-13: Comparison and prediction for different hole lengths and Re numbers.

D-4 Smoothed Entrance Effect
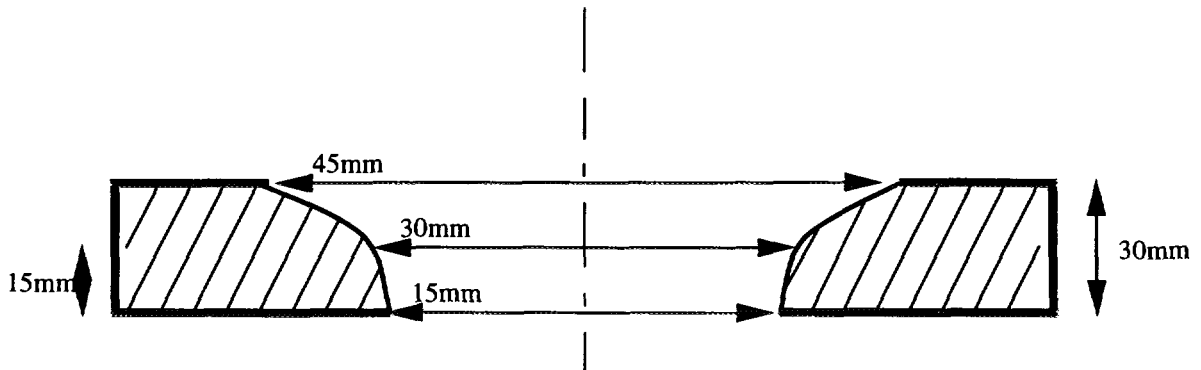
Figure D-14: Smoothed Entrance Geometry
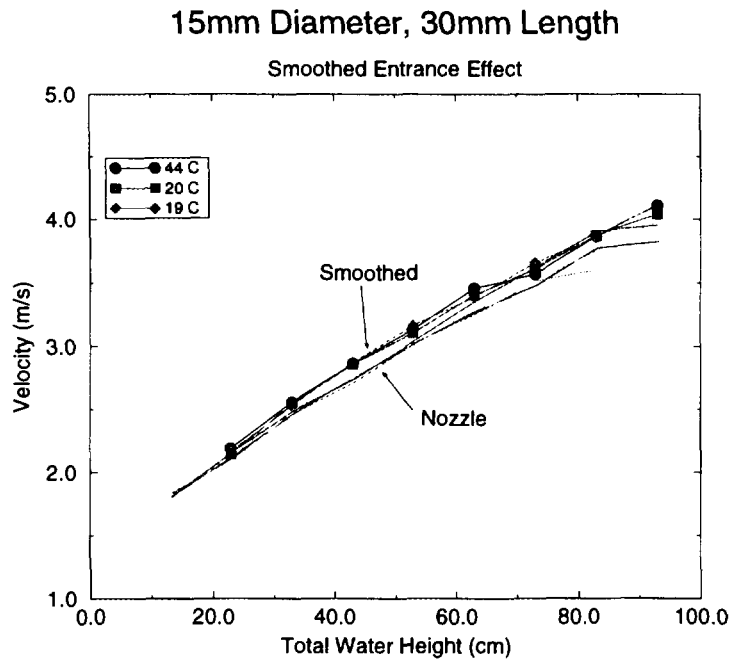
Figure D-15: Comparison of Smoothed and Sharp Entrance Geometry

From past experiments using $PbO\text{-}B_2O_3$ and $CaO\text{-}B_2O_3$ melts onto Pb plates [11], [12], the geometry of the hole ablation location has been shown to be multi-dimensional with a typically "funnel-like" shape. Fundamental fluid flow experiments have shown that a smoothed entrance exhibits a higher equivalent discharge factor as shown in Table D-1. Measurements similar to that of the nozzle were completed with a plate of dimensions shown in Figure D-14. A comparison with the sharp-edged nozzle of similar L/D is provided in Figure D-15. The difference is small yet noticeable. The smoothed entrance

69

provides for higher discharge velocities at equivalent gravity driving forces. This is as would be expected due to the lesser entrance pressure loss.

D-5 Viscosity Effect

Experiments were also conducted using paraffin oil as working fluid. It was found that the fluid viscosity affects, primarily, the in-hole friction. Once the pressure loss in the hole is properly accounted for, the discharge coefficient can be predicted by Eq.(D-5).

D-6 Discussion

In the above, values of the discharge coefficient, C_d, for water and paraffin oil draining from an open tank through a lower flat plate with a centrally located opening are obtained and analyzed. Of particular interest is the fact that the discharge considered here is for a more dense fluid into air, whereas most previous studies have dealt with orifii/nozzles in pipe flow where upstream and downstream fluids are identical.

It was found that for cases with $L/D \geq 1$, the discharge coefficient approaches 1, while for cases with $L/D < 1$ a transition to $C_d \simeq 0.7$ was observed. Thus, when the discharge nozzle has a certain finite length the fluid is ejected from the pressure vessel easier than when the nozzle is very short or being an orifice. The expansion pressure loss is found to be responsible for such a behavior. Dependence of the discharge coefficient on fluid viscosity and surface tension was also experimentally examined for selected fluids. It is suggested that for fluids with high surface tension coefficient the discharge flow is generally coherent and the discharge coefficient is in the range 0.9-1.1.

The measured discharge coefficient values are well predicted by a combination of entrance, in-hole and exit form loss pressure drops; Eq.(D-5).

Application of these results is made for the situation of melt discharge from a nuclear plant pressure vessel during a postulated severe accident in which a melt pool has formed in the reactor pressure vessel lower head. Longer discharge path-lengths are also considered here since the possibility exists for the melt to discharge via a longer nozzle or through a combined length of melt pool crust layer and vessel metal.

For conditions of interest to melt discharge during a severe reactor accident due to a penetration failure, the sensitivity to the hole ablation process may not be significant. This is the result of competing mechanisms. As shown above, increased values of C_d are associated with increased fluid discharge velocities which then decreases the time

required to discharge a given volume under equivalent pressure driving conditions. Yet, the increased flow velocity will also produce increased convective heat transfer to the ablating structure (vessel wall) and thus a faster rate of hole growth. Combined, the overall sensitivity of this process to the value of C_d may not appear large but since the the source terms for melt discharge to the containment may be significantly altered, a more mechanistic manner of determining discharge coefficients is desirable.

When applying the above model to determine the discharge coefficient C_d, the flow discharge periods measured in hole ablation experiments were well predicted by the HAMISA code. This result confirms that the discharge coefficient, being a form parameter, is insensitive to transient (hole enlargement) process and to surface roughness, induced by phase change process within the discharge hole (crust formation and/or wall melting). The later is associated with a minor role of the in-hole friction in comparison to the expansion and contraction pressure losses.

D-7   Summary

A series of experiments were performed in the RIT/NPS Laboratory to investigate the discharge coefficient for flow exiting an overlying pool through a known geometry nozzle. The data was collected in order to reduce the uncertainty associated with melt pool flow through the bottom of a RPV lower head during a severe reactor accident. Several past scaling analysis which were directed at vessel hole ablation had employed an empirical discharge coefficient that is not directly applicable for a reactor situation. This is due to the fact that the common L/D ratio in the reactor case is not small enough to warrant a discharge coefficient typically employed for orifii.

The conclusions from this experimental study can be summarized as follows:

- Discharge coefficients were measured for 15 and 25 mm diameter holes with L/D ratios ranging from 0.08 to 4;

- A range of water temperatures were employed in order to significantly vary the Pr ($3 < Pr < 12$) and Re ($15,000 < Re < 300,000$) of the fluid;

- Results were consistently reproducible;

- Measured discharge coefficients vary by a factor of 2x to that of the value of 0.6 used in previous scaling work;

- At lower nozzle lengths a *step* transfer into lower C_d values was observed;

- A method of employing contraction, in-hole and expansion loss coefficients to determine the discharge coefficient is proposed and shown to adequately represent the test data.

Nomenclature

Arabic

C_d	Discharge Coefficient
D	Diameter (of hole), m
F	Pressure Loss Factor
g	Gravitational Acceleration Coefficient, m/s^2
H	Height, m
P	Pressure, Pa
Pr	Prandtl number, $Pr = \nu/\alpha$
Re	Reynolds number, $Re = UD/\nu$
U	Discharge velocity, m/s

Greek

α	Thermal diffusivity, m^2/s
β	Ratio of flow areas, $\beta = \frac{A_{downstream}}{A_{upstream}}$
ν	Kinematic viscosity, m^2/s
ρ	Density, kg/m^3

References

[1] R.H. Perry and C.H. Chilton, Chemical Engineer's Handbook, McGraw-Hill Book Company, New York, 1973.

[2] A. Lichtarowicz, R.K. Duggins and E. Markland, "Discharge Coefficients for Incompressible Non-Cavitating Flow Through Long Orifices," Journal of Mechanical Engineering Science, Vol. 7, No. 2, 1965, pp. 210-219.

[3] Kiljanski, T., "Discharge Coefficient for Free Jets from Orifices at Low Reynolds Number," Journal of Fluids Engineering, Vol. 115, pp. 778-781, 1993.

[4] T.N. Dinh, V.A. Bui, R.R. Nourgaliev, T. Okkonen, and B.R. Sehgal, "Modeling of Heat and Mass Transfer Processes During Core Melt Discharge From A Reactor Pressure Vessel", J. Nuclear Engineering and Design, Vol. 163, pp.191-206 (1996).

[5] T.N. Dinh, J.A. Green and B.R. Sehgal, "On Mechanisms That Govern the Vessel Melt Source for Ex-Vessel FCIs," Proceedings of ICONE-5, May, 1996.

[6] M.M. Pilch, "Continued Enlargement of the Initial Failure Site in the Reactor Pressure Vessel," J. Nuclear Engineering and Design, Vol. 164, pp. 137-146, (1996).

[7] B.R. Bird, W.E. Stewart and E.N. Lightfoot, "Transport Phenomena," Wiley International, New York, 1960.

[8] L.V. Boronina, N.V. Tarasova and V.P. Kovrizhnykh, "Experimental Study of the Effect of Transiency of Water Flow on Orifice Measurements of Flowrate," Fluid Mechanics-Soviet Research, Vol. 18, No. 1, January-February, 1989, pp. 95-99.

[9] A.S. Dudko, "Conditions for Entry of the Air Core of a Vortex Funnel into an Orifice on the Bottom," Fluid Mechanics-Soviet Research, Vol. 18, No. 1, January-February, 1989, pp. 35-41.

[10] Morton, D., "Process Fluid Mechanics", Prentice Hill, Englewood Cliffs, N.J., 1980.

[11] Sehgal, B. R., et al., "Experiments on Vessel Hole Ablation During Severe Accidents", Proceedings of the International Seminar on Heat and Mass Transfer in Severe Reactor Accidents, Izmir, Turkey, 1995.

[12] Green, J., et al., "Experiments on Melt Jet Impingement and Vessel Hole Ablation Phenomena," International Topical Meeting on Probabilistic Safety Analysis, Park City Utah, (October 1996).

Appendix E: On Mechanism that Govern the Vessel Melt Source for Ex-Vessel FCIs: Hole Ablation Phenomenology and Prediction Method

Abstract

This section summarizes the findings from research conducted at the Royal Institute of Technology - Division of Nuclear Power Safety (RIT/NPS) concerning reactor pressure vessel hole ablation during a hypothetical light water reactor (LWR) severe accident. The major physical mechanisms which govern the vessel hole enlargement during core melt discharge from the reactor vessel lower plenum were identified and analyzed. Substantial insight into these processes has been gained. The understanding achieved has been incorporated into the mechanistic HAMISA model with excellent comparisons to experimental data. The remaining uncertainties in prototypical reactor assessments are primarily attributable to the melt conditions and geometrical aspects at the time of vessel failure.

E-1   Introduction

The newer ABB boiling water reactor (BWR) plants located in Sweden and Finland employ a severe accident management procedure in which a deep water pool is established under the vessel, as soon as it becomes clear that the water level in the core may fall below the top of the fuel. The motivation for this strategy is that the core melt jet will fragment during its passage through the water and that the coarse particles which are formed will be cooled permanently within the water pool. The success of this procedure is predicated upon the judgement, that a large steam explosion, which could threaten the containment integrity during the melt-water interaction, will not occur.

The configuration of the in-vessel melt debris/pool at the time of lower head failure will be highly dependent upon the accident progression scenario variables up to the point in time of vessel failure. The extent of core-melt relocation, and the possibility of melt quenching due to the presence of coolant in the lower plenum regions, are two examples of such variables. The melt ejection out of the vessel would be governed by the driving forces (vessel over-pressure, hydraulic head of the melt pool) as well as the melt flow and heat transfer-induced ablation of the lower head wall around the initial failure site. The lower head failure location may affect the discharge flow, although eventually, most heat-generating material could be ejected. The melt discharge rate and other characteristics (composition, superheat) are important for determining the consequences of the ex-vessel fuel-coolant interactions (FCIs). Thus, an improved understanding of lower head ablation

during melt discharge through a local failure site, is a necessary step towards defining the progression of the ex-vessel FCI process [1].

This paper considers the vessel ablation process, which increases the size of a hole, or a local failure, in the wall of the reactor pressure vessel (RPV) lower head, as the core melt is discharged into the containment (see Fig.E-1). Depressurization of the reactor coolant system is assumed to occur prior to vessel failure. This is a wholly justifiable assumption for the Nordic BWRs since primary system depressurization is a required accident management procedure under the circumstances considered. Global vessel failure (i.e. a nearly complete breach of the reactor pressure vessel) is not considered here, since failure of penetration tubes (control rod or instrumentation tubes), or local vessel creep failure, are much more likely failure mechanisms [2].
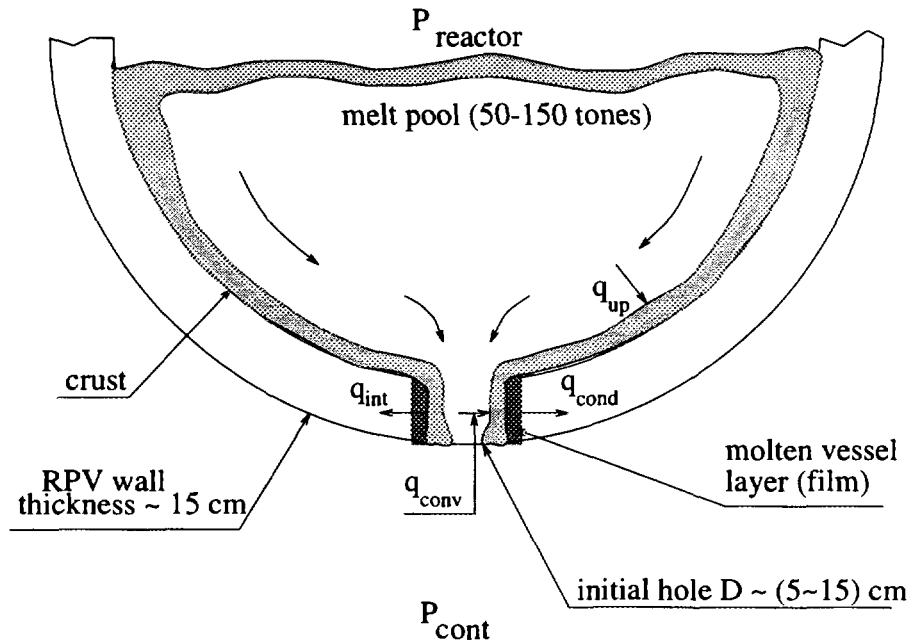
Figure E-1: Physical picture of hole ablation phenomenology.

E-1.1 Previous work & experimental background

A review of experiments conducted in the past, mainly at Sandia National Laboratory (SNL), can be found in the paper by Pilch [3]. Pilch also proposed a scaling methodology, which indicated that the SNL experiments did not fall in the prototypic-condition parameter range for penetration failures. A review of concepts employed in relevant reactor safety assessments can be found in [4] and will not be repeated here.

Model development and experiments have been pursued at RIT/NPS in order to gain an improved understanding of the complicated melt-vessel interaction processes which

occur during vessel failure and melt discharge. Several aspects which govern the hole ablation process such as vessel heat conduction and phase change, melt thermal-hydraulics in the lower plenum, prior to, and during, the discharge process, melt discharge flow characteristics and gas blowthrough, and crust formation and its stability, were addressed in [4] [5]. The continued enlargement of the initial failure site in the RPV lower head is determined by these processes. It was found that not only integral scaling parameters (timing and final hole opening) matter, but also the scaling groups for separate component processes may be able to change the physical picture under consideration. Furthermore, it was found that experiments are needed to resolve phenomenological uncertainties associated with in-hole convective heat transfer, crust formation and stability, and discharge flow rates.

In earlier RIT/NPS experiments, molten binary oxidic materials ($PbO - B_2O_3$ and $CaO - B_2O_3$) were employed as working fluids. Recent experiments have employed more prototypic ranges of the integral scaling parameters by using several pairs of simulant materials for melt and plate, namely [molten binary salt mixtures-Cerrobend], [water - salt-water ice], [paraffin oil - salt-water ice] [6]. Also, large variations in fluid Prandtl number and discharge flow Reynolds number were covered. These experiments provide a necessary database for advancing the level of knowledge concerning the governing mass and energy transfer mechanisms and for validating the predictive capability of the various empirical correlations which must be employed for such a problem.

E-1.2 Objectives

Analyses are performed for cases in which a core melt pool was formed inside the RPV lower head, prior to the melt discharge. The primary objectives of this paper are to identify and to analyze physical mechanisms which may limit the dynamics of the vessel hole enlargement, and hence to provide bounding assessments of melt discharge flow rates used in quantification of the consequences of ex-vessel fuel-coolant interactions [1].

E-1.3 Method and work performed

First, limiting mechanisms of vessel hole enlargement will be identified, with particular emphasis on scenario- and reactor design-dependent aspects. Second, the experimental observations and data are employed to assess the major phenomenological uncertainties. Next, the HAMISA model [4] and computer code, which has been developed at RIT/NPS, is used to perform simulations. The new information and experimental data obtained was used to validate the performance of the HAMISA model under high-Reynolds-number conditions. In particular, the influence of phase change on convective heat transfer, and the effect of a finite vessel wall thickness on the discharge coefficient were introduced into

the HAMISA model.

Reactor predictions of the vessel hole ablation and core melt discharge processes, and discussion of their implications, while accounting for limiting mechanisms, are presented in the following sections.

E-2   Phenomenology of Hole Ablation and Limiting Mechanisms

The phenomenology of hole ablation and related processes can be decomposed based as follows:

- (i) convective heat transfer in the discharge hole and in the lower head melt pool during the discharge process;

- (ii) vessel heat conduction and phase change;

- (iii) discharge flow characteristics.

In the paper by Dinh et al. [4], several important phenomena were examined, namely crust existence, entrance and property effects on laminar and turbulent convective heat transfer in the discharge hole, gas blowthrough and multi-dimensional heat conduction and phase change in the vessel wall.

However, there remained phenomenological uncertainties related to (a) crust behavior under high-Reynolds number flow conditions, (b) convective heat transfer with phase change (freezing/melting) boundary conditions, and (c) discharge flow rate (or discharge coefficient) through a hole of finite length. Resolution of these phenomenological uncertainties is discussed in the next section, while in this section we focus on uncertainties associated with scenarios of accident progression and specific design features applicable to the reactor lower plenum.

E-2.1   In-hole crust growth and stability

Initial calculations which employed an earlier version of the HAMISA model (version HAMISA.0) indicate that the hole ablation rate depends strongly on whether a crust layer exists as a thermal boundary resistance to the in-hole melt flow. In reactor cases, discharge of some $9m^3$ of core melt may lead to final hole sizes up to 0.6m for the case without crust and 0.3-0.4m when a crust layer is present. More importantly, hole enlargement dynamics

77
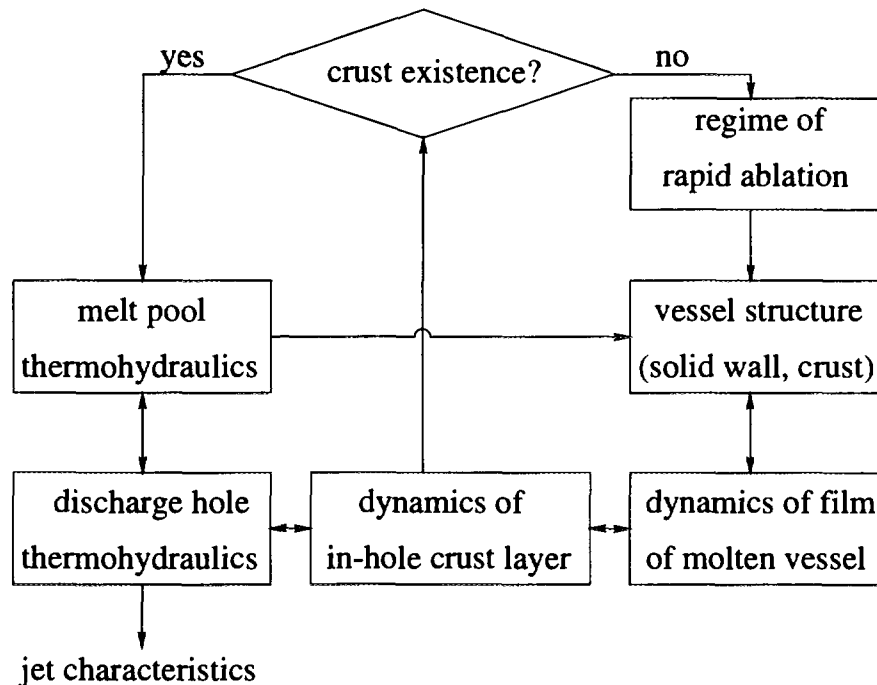
Figure E-2: Hole ablation phenomenological scheme.

are completely different for the two cases, such that the characteristic time of the melt discharge process for the case without crust is on the order of 1 second or less, while that in the case with crust can extend to several tens of seconds. Therefore, the limiting mechanisms of hole ablation are based on phenomena which ensure crust growth and stability.

E-2.2 Initial debris crust layer in the lower plenum

In previous reactor safety assessments (including the modeling effort of ref. [4]) the presence of an initial debris crust layer (IDCL) in the reactor pressure vessel lower plenum was ignored. Simulations of debris heating and melt pool formation in the RPV lower head, performed using the MVITA code of RIT/NPS [7], revealed that a thick crust layer exists at the lowermost region of the reactor lower plenum. This crust layer may be as much as 0.2m thick at the moment of melt pool formation and persists at a thickness of 0.05m, until circumferential vessel rupture is predicted. It should be mentioned that neither the failure of the lower head penetrations (instrument nozzles or control rod drive mechanisms) nor any external heat sink was simulated using the MVITA code.

Hole ablation dynamics are affected by the IDCL through a number of heat and mass transfer mechanisms, as described below.

- The IDCL is a heat capacitor and as an oxidic material it will exhibit a relatively large heat of fusion. Opening of the intial hole (in both the IDCL and the vessel wall) requires melting of both the wall and the debris crust which lies above the vessel.

- For the section of the hole which is in the IDCL, the question of "crust existence" plays no role. Subsequently, the melt-to-hole heat fluxes, and thereby the ablation rates, in this portion of the hole will be limited primarily by the melt superheat.

- Ablation of the hole section in the IDCL supplies a mass of remelted crust into the melt flow boundary layer before it enters the hole section in the vessel wall. In addition, heat transfer from the melt flow to its crust lowers the melt flow boundary layer temperature. According to estimates of conduction-controlled phase change behavior at the contact between melt and steel vessel ([4]) the lower melt flow boundary layer temperature will significantly reduce the characteristic time necessary for crust formation. Under such conditions, it was found that crust growth dominates crust remelting even at the entry region of the vessel-hole section.

- Entrance effects on the melt flow heat transfer, for the case of a phase change boundary, will be substantially reduced or eliminated when an IDCL is present.

- Given all of the above mechanisms, particularly the addition of the "cool" melt to the boundary layer and the reduced entrance effect, it is evident that vessel wall heat fluxes will decrease with increasing IDCL thicknesses.

- Also, the low velocity of melt flow in the lower head pool and the relatively low superheat of melt located next to the IDCL will result in little if any re-melting and erosion of the IDCL by the pool flow. Furthermore, the IDCL is a thermal resistance to energy transfer from melt pool to the vessel wall, particularly during the discharge period. Consequently, it limits multi-dimensional pre-heating of the vessel prior to ablation.

The arguments made above clearly demonstrate the important role of an initial debris crust layer in limiting the dynamics of the vessel hole enlargement during the melt discharge process.

E-3 HAMISA Model Development and Validation

gas blowthrough

convective heat transfer with phase change b.c.

discharge coefficient

entrance effect

| mass (0D) | moment (0D) | energy (0D - 1D) |

mass & moment (0D - 1D)

energy (0D - 1D)

MELT POOL

DISCHARGE HOLE

pool-crust heat tr.

INITIAL DEBRIS CRUST LAYER
(1D - 2D)

crust dynamics

VESSEL ABLATION
(1D - 2D)

layer of molten vessel
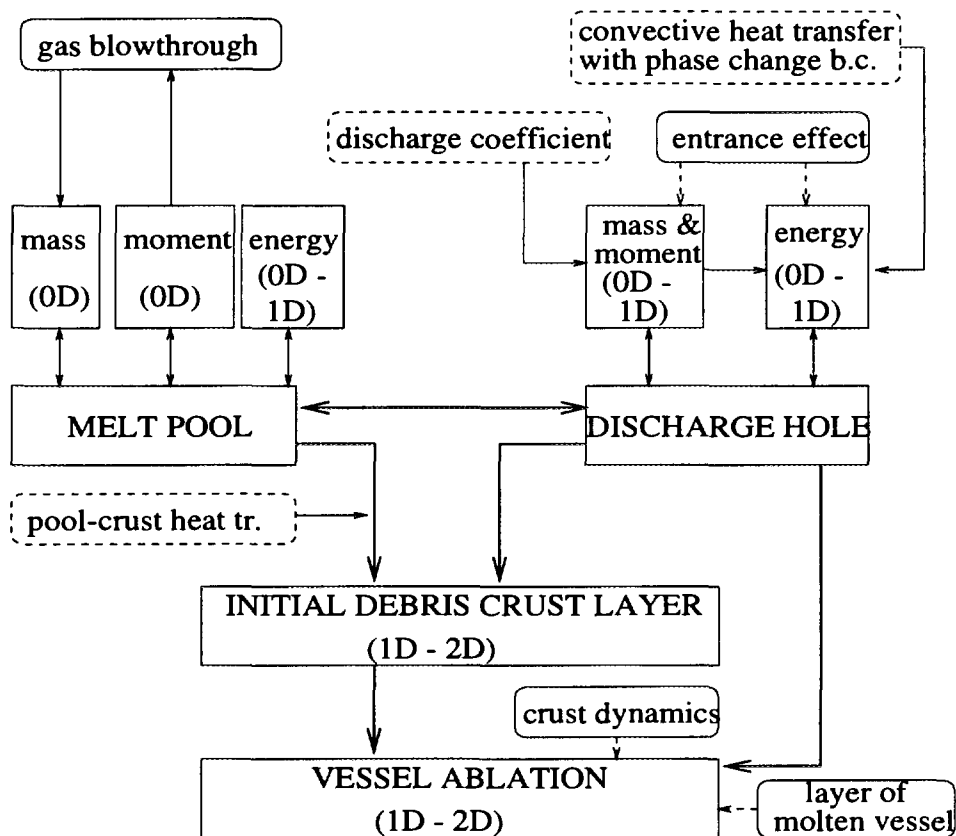
Figure E-3: Component models of the HAMISA model.

The HAMISA model is validated against low and intermediate-temperature experiments. The HAMISA model includes zero- and one-dimensional models of transient heat transfer in the experimental melt pool prior to and during melt discharge. Options included in the HAMISA model account for specific effects of experimentation, such as melt pouring into the vessel and growth of the melt crust prior to melt discharge, heat removal from the melt pool to upper and side structure of the vessel, for example. One-dimensional modeling of convective heat transfer in the discharge hole and a two-dimensional model of heat conduction and phase change in the initial debris crust layer and vessel wall are implemented in the present version [4]. Three component models, namely (i) discharge coefficient, (ii) convective heat transfer with phase change boundary condition in the discharge hole and (iii) pool-crust interface heat transfer, were significantly improved, based on insight obtained from relevant experiments (see Fig.E-3).

E-3.1   Discharge flow rate calculations

Standard hydraulic pressure losses will necessarily be associated with the discharge of the melt volume through the vessel failure hole. Earlier considerations, such as that found by Pilch in [3], accounted for the in-hole melt flow pressure loss by the use of common discharge coefficients, C_d. In [3] a value of 0.6 is recommended for the discharge coefficient based upon flow through a sharp-edged orifice coupled with the fact that it provided good agreement to vessel rupture failure tests. However, for penetration-type failures the melt must flow through a hole of at least a thickness equivalent to the RPV and in the case of an IDCL, over a longer distance. This is not characteristic of flow through an orifice and the longer in-hole flow distance will present both entrance and exit losses along with the frictional pressure losses for the in-hole section of flow.

A series of separate effects tests were conducted in order to better examine the role of frictional pressure losses for conditions applicable to hole ablation dynamics. A 90 liter tank was assembled with a bottom plate thickness of δ_w in which a central hole of diameter, D, was drilled. Both the thickness and hole diameter of the plate were varied during these tests to cover a range of δ_w/D from 0.08 to 4 using 15 and 25mm diameter holes. Such an aspect ratio for melt flow is representative of the ranges envisioned in reactor scale penetration failures. The working fluid was water which ranged in temperature from 3 to 70°C. Fluid discharge through the plate hole was initiated by removal of a plug mechanism and the drop in water level was measured to determine the discharge velocity in time (in some tests the mass discharged was collected and measured in time with a scale connected to a PC data acquisition system). Since there was no tank overpressure, the experimental discharge coefficient could be calculated in time as;

$$C_d = \frac{U_{exp}}{\sqrt{2 \cdot g \cdot H}} \qquad (E-1)$$

Variation in the tank water temperature allowed for a Pr number variation from 2 to 12 and the measured discharge velocities yielded a Re number range from 16,000 to 250,000. Excellent repeatability was observed throughout the test series thereby providing confident statistical measures.

Results from over 50 experimental runs are summarized in Fig.E-4 where the discharge coefficient is plotted against the measured discharge velocity. Each point represents an average of all tests conducted with identical water temperature and δ_w/D. It is evident from these results that the use of 0.6 for the discharge coefficient will underpredict the melt ejection velocity. Only for the conditions of very thin plate thicknesses, thus approaching similarity to an orifice, were values of 0.6-0.7 realized. Considering the dimensions of RPV penetrations and wall thickness (see for example Fig.E-1) the discharge coefficient can be as much as 70% (and more) greater in comparison to that predicted for an orifice.
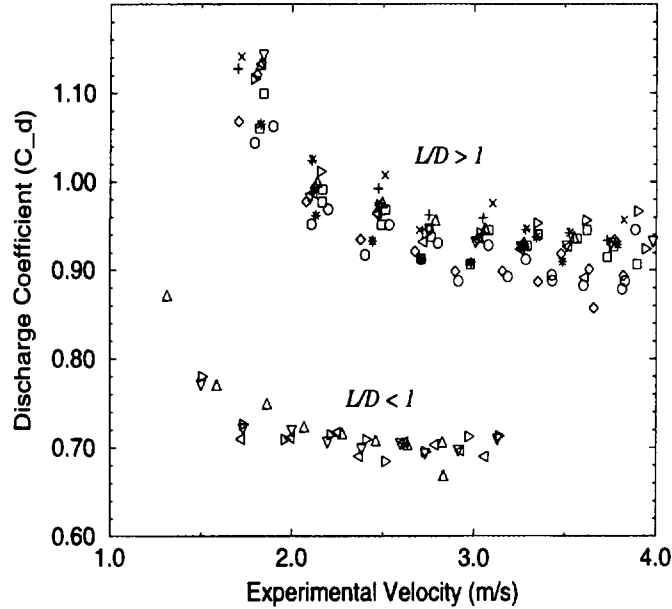
Figure E-4: Experimental discharge coefficient as a function of discharge velocity in RIT tests.

In light of these experimental observations an improved model for the in-hole pressure drops was incorporated into the HAMISA program. The discharge flow rate is determined from the following equation for flow through a hole of finite length.

$$U = C_d\sqrt{\frac{\Delta P}{\rho}} = \frac{1}{F\rho}[\sqrt{2(P_{RPV} - P_{cont} + \rho g H)}] \qquad (E-2)$$

where F is the overall form loss coefficient and the driving pressure difference is that between the primary system and containment. The total form loss is a summation of the contraction ($F_{cont} \sim 0.45$), in-hole ($F_{in-hole} = f(Re)$) and expansion losses ($F_{exit} \sim 1.0$) with values taken from classical fluid dynamics. Friction for the in-hole flow is considered flow-regime dependent and several correlations have been provided for depending upon the value of the flow Re number.

The discharge experiments reported here certainly do not cover all aspects which may be applicable to reactor vessel failures. Other factors such as the melt viscosity and surface tension as well as the possibility for a rounded (smoothed) entrance geometry may reveal further insight which can then be incorporated into predictive tools such as the HAMISA model.

82

It may be argued that the sensitivity of the hole ablation process to the failure location melt flow pressure drop is not large. That is to say, that accounting for the hole entrance, in-hole and exit losses does not significantly influence the final vessel hole size. This arises as a result of two competing ablation mechanisms. In the first, an increased value of the discharge coefficient will produce increased melt ejection velocities for equivalent hydraulic driving forces. This in turn reduces the *time* of melt flow ablation for a given melt volume. In the second mechanism, the increased melt velocity will result in enhanced convective heat transfer from the flow to the ablating wall (increased Re) thereby increasing the *rate* of vessel ablation. Combined, these two mechanisms may indeed only slightly influence the final predicted hole size but the vessel melt source rates for ex-vessel FCIs may be significantly affected. Therefore, a more mechanistic model which captures both effects, such as the one proposed and incorporated in the HAMISA code, is preferable, especially when consideration of an IDCL is made.

E-3.2   Convective heat transfer in the discharge hole

As a result of recent RIT experiments involving both hole ablation and jet impingement with phase change [6], [8] a new model for heat transfer from the flowing melt to the solid interface has been proposed. Dinh and co-workers [9] have shown that the surface roughness associated with the phase change process enhances energy transfer from the melt to the ablating structure. In a series of water-ice and water-salt ice jet impingement experiments it was recognized that the surface roughness, resulting from the phase change of the melting plate material was a controlling factor in the transition from laminar to turbulent heat transfer regimes in the jet stagnation zone. Experimental observations from the jet impingement research may then be extended to the vessel ablation conditions, considered here, due to the underlying similarities in the heat transfer mechanisms between the two processes.

The change of phase of an ablating wall material will produce a roughened surface, regardless of whether or not the conditions for crust layer existence are met. This, in turn, influences the hydrodynamic and thermal boundary layers which must develop and flow past the surface. When the surface roughness becomes thicker than the hydrodynamic sublayer the convective heat transfer will be enhanced, and more importantly, the dependence upon length scales may be reduced or eliminated altogether. Determination of the convective heat transfer from the melt flow to the crust interface will, from classical considerations, depend upon the in-hole skin factor (C_f'), and the Re and Pr numbers for the flow. Under the rough surface conditions associated with phase change, the viscous sublayer is believed to be thin and the skin factor of the surface will become independent of Reynolds number as is the case for common pipe flow. It is clear that the impact of the surface roughness will be significantly influenced by values of the melt fluid Pr number since this number reflects the relationship between the inertial and thermal boundary layers.

For turbulent flow conditions, which is the case in the prototypical situation, the energy transfer can be determined using the Reynolds analogy [10]

$$h = \frac{1}{2}U_\infty \cdot \rho \cdot C_p \cdot C_f' \qquad (E-3)$$

For rough surfaces the value of C_f' may range from 0.005 to 0.007. Eq.E-3 can be easily rearranged as

$$Nu = \frac{1}{2} \cdot Re \cdot Pr \cdot C_f' = \frac{1}{2}C_f' \cdot Pe \qquad (E-4)$$

Notice that the combination of the Re and Pr numbers removes any influence of the fluid viscosity, and the governing dimensionless group then becomes the Peclet number.

Consideration of the aforementioned surface roughness effects for the case of RPV ablation dynamics, reveals for the turbulent, high Re number, conditions anticipated that the convective energy transfer from the flowing melt to the stable crust layer will be enhanced depending upon the magnitude of the surface roughness, that it will become independent of the Re number and finally that entrance effects for the flow will be minimized. Concerning this latter item, the implication is that the growth of the failure site will be approximately cylindrical as the result of a much more uniform heat flux along the flowpath for melt.

The above models for melt-flow pressure drop and convective heat transfer in the discharge hole were incorporated into the HAMISA code. Validation of the models was obtained by comparison to hole ablation experiments using corium simulant materials conducted at the RIT/NPS laboratory.

E-3.3   Comparison to experimental ablation rates

Descriptions of the hole ablation experiments conducted at RIT can be found in the references by Green et al. [8] and Sehgal et al. [6] and thus will not be repeated in detail here. Briefly, certain volumes of melts from simulant materials were generated and placed in contact with a plate in which thermocouples were embedded and in which an initial hole of known diameter had been placed. Rates of plate ablation, and thus heat transfer, were derived from the embedded thermocouple response, along with the more important integral parameters i.e., the final hole size, timing of melt discharge and the shape of the ablated region. The relevant melt-plate simulant combinations involved water-salt ice, $NaNO_3+KNO_3$- cerrobend alloy, $NaNO_3+KNO_3$-Sn, and paraffin oil-salt ice. Table E-1

provides a listing of the relevant parameters for several of the RIT/NPS hole ablation experiments.

Table E-1: RIT Hole Ablation Experiments

Test	Melt Fluid	Plate Material	D_o (mm)	δ_w (mm)	T_{melt} (°C)	$T_{o,plate}$ (°C)	V_{melt} (m³)
0917A	Water	Salt-Ice	20	50	23	-30	78
0917B	Water	Salt-Ice	20	50	41	-28	78
0918	Water	Salt-Ice	10	60	48	-20	78
0919	Water	Salt-Ice	10	60	46	-33	78
0923	Water	Salt-Ice	10	60	80	-40	76
0925	Water	Salt-Ice	20	60	3	-30	76
1002	Water	Salt-Ice	10	38	11	-41	78
1015	Water	Salt-Ice	10	80	44	-24	78
1016	Water	Salt-Ice	20	79	91	-31	78
1023	Paraffin Oil	Salt-Ice	20	60	29	-37	74
1024	Paraffin Oil	Salt-Ice	20	63	45	-38	69
1129	20-80 $(Na,K)NO_3$	Cerrobend	10	50	450	25	25
1205	20-80 $(Na,K)NO_3$	Tin	10	50	420	25	25
1211	50-50 $(Na,K)NO_3$	Tin	10	50	440	50	23

In these experiments it was clear that the crust layer played a controlling role in the ablation process. The reduction of the melt liquid temperature (see e.g. 0925 in Table E-1) yielded extended discharge times due to the only slight ablation. Crust layers of varying thickness were found on the in-hole and upper surface of the plates. Visual observation of the final ablated hole conditions revealed that the final surface was indeed substantially roughened and, that for all but the paraffin-oil tests, the final hole geometry was reasonably cylindrical, indicating a uniform ablation heat transfer.

The relevant experimental conditions and thermodynamic properties were then supplied as input for the HAMISA model. In these simulations the aforementioned entrance and exit form loss coefficients were supplied along with an average skin factor of 0.0055. The experimental plate was nodalized in two dimensions. Results are presented in Table E-2 from which it is clear that the agreement between HAMISA and the experiments is very good and that both the final hole diameters as well as the melt discharge times are properly predicted.

The data obtained from the RIT/NPS hole ablation tests also provides important information regarding the relevant scaling parameters for prototypic penetration-type failures. This is seen in Fig.E-5 where the RIT data is presented according to the scaling parameters of Pilch [3] which are shown in the last columns of Table E-2. The boxed region

Table E-2: HAMISA Validation on RIT/NPS Hole-Ablation Experiments

Test	Experiment D_f^T	D_f^B	HAMISA D_f (mm)	Experiment t_d (s)	HAMISA t_d (s)	$\Delta D/D_o$ (-)	τ_m/τ_D (-)
0917A	72	72	70	16	18	2.5	13
0917B	72	65	76	12	15	2.8	23
0918	94	87	87	14	13	7.7	233
0919	90	86	85	15	13	7.5	219
0923	90	96	96	12	11	8.6	309
0925	28	25	24	77	78	0.2	0.5
1002	64	60	59	27	32	4.9	45
1015	100	94	88	14	12	7.8	228
1016	103	105	107	10	8	4.4	56
1205	54	56	50	11	12	4.3	56
1211	68	60	50	11	12	4.9	59

represents postulated severe accident conditions for a corium melt pool of volumes 1.3 to 19 m^3, at system pressures of 2 to 10 bar, and for different initial failure sizes as presented in the paper by Sehgal and co-workers [5]. As can be seen in the figure, the recent simulant hole ablation tests extend the available experimental database. In addition, the Reynolds number of the in-hole flow was sufficiently high ($3 \cdot 10^5$). More importantly, in all the experiments, the crust was found to be effective and, hence, limited the hole enlargement.

E-4   Related Aspects

E-4.1   Scenario- and design-dependent aspects

Two major parameters can be used to categorize boundary and initial conditions for the hole ablation process: location of (initial) failure site and configuration of the in-vessel debris at the moment of vessel failure. Both of these parameters depend on the accident scenario progression and specific design features of the reactor lower plenum.

It is obvious that if only a small amount of molten material is present in the lower plenum at the time of vessel failure then no significant vessel-hole ablation will occur. More importantly, in such a case, the melt jet which is ejected will remain close to the original small diameter. Such a jet may even fragment in air, and if not, most probably as it passes through the coolant (liquid) pool. Subsequently the flow rate of core melt discharged from the RPV will be determined by the heat-up and remelting of the debris,
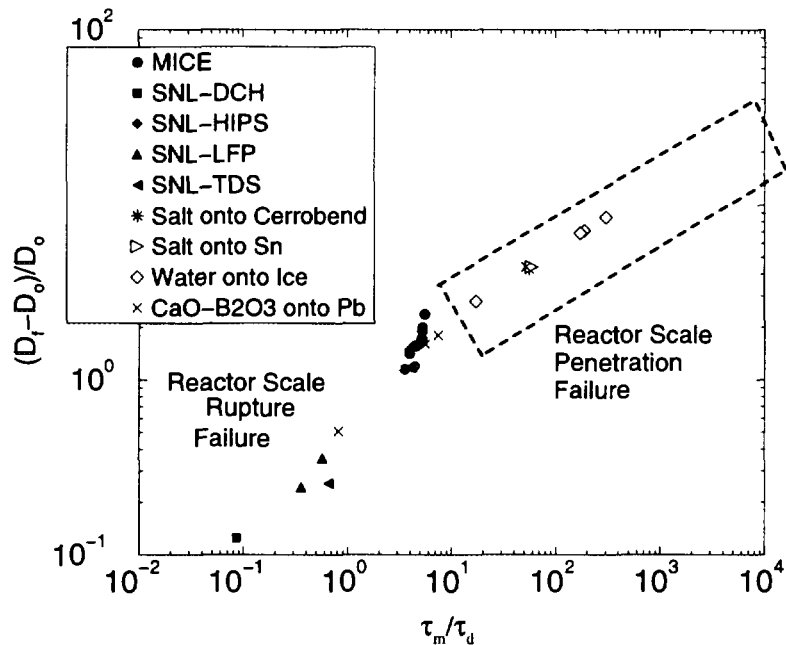
Figure E-5: Hole ablation scaling.

which will take substantial time. Thus, in this scenario the containment failure by steam explosion, or through base-mat melt through may not be credible.

E-4.2 Corium melt-phase properties

Oxidic melt pools, such as corium, present unique challanges to phase change related processes in light of their *mushy* zone behavior. The melt pool thermodynamics will be further complicated by the fact that unoxidized metals such as Zr, as well as other melted core structural materials, will also be present in the pool. There remain significant uncertainties not only in determining accurate corium physical properties but also for the melt phase diagram itself. From this arises the question: what temperature gradient is appropriate for use in determining fluid-to-structure energy transfer rates: $(T_{melt}-T_{sol})$ or $(T_{melt}-T_{liq})$? The answer, obtained from the analysis of the RIT binary-salt experiments, is $(T_{melt}-T_{liq})$. Nevertheless, this question must be further investigated as better information on the core melt phase diagram and properties and observations from reactor-material experiments are made available.

As can be seen from Table E-2, in most experimental runs, the final hole is quite cylindrical, so that it can be concluded that two-dimensional heat conduction in the experimen-

tal plates as well as entrance effects on convective heat transfer are negligibly small. For experiments, employing paraffin oil as working fluid, the hole is two-dimensional, reflecting both 2D heat transfer during the long period of melt (oil) discharge and possible entrance effects for the highly viscous oil. Similarly, in a prototypic situation, two-dimensional ablation of the reactor vessel and overlying fuel crust (IDCL) can occur in case of small melt superheat, i.e. dominance of mushy-phase highly-viscous melt.

E-4.3 Example of reactor assessment

Results of reactor predictions, performed by using the HAMISA model, indicate that most of the melt volume is discharged from the RPV as a coherent jet. The melt volume available in the lower plenum after the gas blowthrough onset is generally less than 10% (for overpressurization of 0.7MPa). The vessel hole enlargement dynamics for the proto-typic vessel, with about 70 tonnes of molten core materials in the vessel lower plenum is predicted to be in the range 6-10mm/s, i.e. the time period to have the initial hole of 10cm diameter to grow up to 25-30cm would take 20-25s. Thus, for the ex-vessel FCIs the interaction between coolant pool and quasi-steady melt jet should be analyzed.

Sensitivity analysis of remaining phenomenological uncertainties indicates that they do not appear to significantly affect the physical picture established from the results of RIT/NPS experiments and analyses. The HAMISA model, validated against experimental data, provides a tool with which the hole ablation process can be described and, therefore, the ex-vessel melt source can be determined for problems involving FCIs. Thus, overriding uncertainties in predictions of vessel melt source for ex-vessel FCIs, in prototypic accident scenarios, are the related intangibles of accident scenarios. For instance, knowledge of the configuration of melt pool and frozen crust as well as the failure location are essential for determining the discharge parameters, since the hole ablation dynamics are affected by the presence of the in-vessel (initial) crust layer.

E-5   Concluding Remarks

Phenomena and factors of potential importance to dynamics of vessel hole enlargement during core melt discharge from the reactor pressure vessel were identified and analyzed in the present study. Phenomenologically, the major findings are as follows;

- It appears that the in-hole crust is stable (or at least exists as a boundary condition) even under high Reynolds number and high heat flux conditions. Corium, as a binary oxidic melt, may even help to hasten the crust formation. Some other factors

(addition of cooler mass from melting crust into the melt boundary layer, long hole, reduced entrance effect) tend to stabilize the crust.

- The presence of a corium crust layer above the vessel wall reduces the heat up of the vessel wall during the core melt discharge process. This crust layer significantly limits the vessel ablation due to the heat capacity (sensible heat and heat of phase change) of the oxidic material. It also increases the length of the discharge hole and hence affects the in-hole frictional losses, the hole entrance and exit loss coefficients, and the heat flux distribution.

- Accounting for the non-orifice form of the discharge hole leads to a shorter discharge period for a given melt volume.

- For low Prandtl number fluids (such as corium), phase change may significantly affect the convective heat transfer, since phase-change-induced surface roughness may be thicker than the viscous sublayer for high Reynolds number flows. This phenomenon may provide augmentation of the heat transfer coefficient and lead to nearly uniform hole growth.

Nomenclature

Arabic

C_d	Discharge coefficient
C_d'	Skin Factor
C_p	Specific Heat, J/kgK
D	Hole diameter, m
f	Friction factor
F	Form loss coefficient
g	Gravitational Acceleration Coefficient, m/s^2
h	Heat transfer coefficient, W/m^{2}K
H	Melt volume height, m
Nu	Nusselt number
P	Pressure, Pa
Pe	Peclet number
Pr	Prandtl number
Re	Reynolds number
U	Velocity, m/s

Greek

δ_w	Wall, plate thickness, m
ρ	Density, kg/m^3
τ_m	Characteristic melt discharge time, s

τ_d Characteristic hole growth time, s

Subscripts

exp	Experiment
f	Final condition
o	Initial condition
w	Wall
∞	Bulk flow conditions

Abbreviations

IDCL	Initial Debris Crust Layer
RPV	Reactor Pressure Vessel
LWR	Light Water Reactor
BWR	Boiling Water Reactor

References

[1] T.J. Okkonen, T.N. Dinh, V.A. Bui, and B.R. Sehgal, "Quantification of the Ex-Vessel Severe Accident Risks for the Swedish Boiling Water Reactors". A scoping study performed for the APRI project. July 1995. *SKI Report No.95:76.* Swedish Nuclear Power Inspectorate (SKI), 195p (1996).

[2] J.L. Rempe et al. "Light Water Reactor Lower Head Failure Analysis". NUREG/CR-5642. EGG-2618 (October 1993).

[3] M.M. Pilch, "Continued Enlargement of the Initial Failure Site in the Reactor Pressure Vessel", Intern. J. Nuclear Engineering and Design, Vol. 164, pp.137-146 (1996).

[4] T.N. Dinh, V.A. Bui, R.R. Nourgaliev, T. Okkonen, and B.R. Sehgal, "Modeling of Heat and Mass Transfer Processes During Core Melt Discharge From A Reactor Pressure Vessel", Intern. J. Nuclear Engineering and Design, Vol. 163, pp.191-206 (1996).

[5] B.R. Sehgal, J. Andersson, V.A. Bui, T.N. Dinh, and T. Okkonen, "Experiments on Vessel Hole Ablation During Severe Accidents", Proceeding of the International Seminar on "Heat and Mass Transfer in Severe Reactor Accidents", Izmir, Turkey, 1995; Begel House Publ. Inc., 1996.

[6] B.R. Sehgal, J.A. Green and T.N. Dinh, "Experimental and Analytical Investigations of Vessel-Hole Ablation during Severe Accidents", Proceedings of the Fifth International Topical Meeting on Nuclear Thermal Hydraulics, Operations, and Safety (NuTHOS-5), Beijing, China, April 1997.

[7] V.A. Bui, T.N. Dinh, and B.R. Sehgal, "In-Vessel Core Melt Pool Formation during Severe Accidents", Proceedings of the 1996 National Heat Transfer Conference, in the session "Fundamental Phenomena in Severe Accidents", Houston, Texas, August 3-6, 1996, HTC-Vol.9, pp.86-94.

[8] Green, J.A., T. Dinh, W. Dong, and B.R. Sehgal, "Experiments on Melt Jet Impingement and Vessel Hole Ablation Phenomena," Proceedings of the International Topical Meeting on Probabilistic Safety Assessment 1996, Vol. III, pp. 1359, Park City, Utah, October, 1996.

[9] Dinh, T.N., W.G. Dong, J.A. Green, R.R. Nourgaliev, and B.R. Sehgal, "Melt Jet Attack of the Reactor Vessel Wall: Phenomena and Prediction Method," Proceedings of NURETH-8, Tokai-mura, Japan, October, 1997.

[10] Schlichting, H., Boundary Layer Theory, 6th Edition, McGraw-Hill Book Company, New York, 1968.

SKi

STATENS KÄRNKRAFTINSPEKTION
Swedish Nuclear Power Inspectorate